UNIVERSITY OF OKLAHOMA

GRADUATE COLLEGE

INFERRING BULK MICROPHYSICAL CHARACTERISTICS OF MESOSCALE CONVECTIVE SYSTEMS USING POLARIMETRIC RADAR OBSERVATIONS

A THESIS

SUBMITTED TO THE GRADUATE FACULTY

in partial fulfillment of the requirements for the

Degree of

MASTER OF SCIENCE IN METEOROLOGY

By

SHAWN LLOYD HANDLER
Norman, Oklahoma
2017

INFERRING BULK MICROPHYSICAL CHARACTERISTICS OF MESOSCALE CONVECTIVE SYSTEMS USING POLARIMETRIC RADAR OBSERVATIONS

A THESIS APPROVED FOR THE
SCHOOL OF METEOROLOGY

BY

Dr. Cameron Homeyer, Chair

Dr. Guifu Zhang

Dr. David Parsons

Acknowledgements

I would like to thank everyone within the Convection, Climate, and Chemistry (CCC) Research Group here at OU. Every time the CCC group convened, whether we were at our monthly social group meetings or our research meetings, we always seemed to be having fun while learning from each other.

One of my biggest thank yous goes to Dr. Cameron Homeyer for serving as the greatest advisor I could have ever asked for. Dr. Homeyer would always have his door for open for me, and he would listen to me if I had a problem, whether it be research related or if I was frustrated with courses. He helped me through times when I thought I wouldn't be able to make it, or when I had serious doubts as to why I was even here in the first place. At times, he believed in me more than I believed in myself! I definitely wouldn't have been able to complete this thesis if it weren't for him being as active and supportive as he was during my time as a student here.

Lastly, I wouldn't be where I am today if it were not for my loving and supportive family and friends back home in Chicago and Maine, and here in Oklahoma. My once girlfriend, now fiance Meredith, allowed me to make the executive decision to move down to Oklahoma to pursue a graduate degree in hopes of kick-starting our careers. Although there have been ups and downs along the way, she has been fortunate enough to find success and joy in teaching here in Oklahoma. We are both excited for what the future holds for us both here in Oklahoma and thereafter.

Table of Contents

List of Figures

Abstract

In 2013, the network of NEXRAD WSR-88Ds were upgraded to dual-polarization. Dual-polarization allows for the identification of particle shape, size, orientation, and concentration within a radar sample volume due to the addition of new and derived radar variables which include differential reflectivity (Z_{DR}), specific differential phase (K_{DP}), and the co-polar correlation coefficient (ρ_{HV}).

In this study, polarimetric radar observations were utilized to create high-resolution three dimensional composites to better understand bulk hydrometeor distributions and their associated microphysical characteristics within mesoscale convective systems (MCSs). A hydrometeor classification algorithm (HCA), a novel radar echo identification algorithm, and a reanalysis dataset were used to examine hydrometeor distribution changes in relation to storm lifecycle, storm structure, storm environment, geographic location, and time of year. An idealized model was also used to compare observed hydrometeor distributions to those simulated from a model by using a polarimetric radar data simulator (PRDS). This study also demonstrate how microphysical variables from a model and simulated polarimetric radar variables can improve hydrometeor classification.

Results from both the modeling and observational component indicate that graupel particles are typically the most dominant hydrometeor type within the convective region upwards of 5 km above the environmental freezing level during the developing and mature stages of MCSs. Below the freezing level, rainwater dominants, although sometimes small hail and graupel are present in the earlier stages of the MCS. Stratiform precipitation consists of small graupel concentrations within 2 km of the freezing level ($\sim$10%), whereas dry-snow aggregates are the dominant hydrometeor type closer to the freezing level, thereafter ice crystals of various orientations are more dominant near echo top. Issues regarding the melting process in microphysical parameterization are also discussed.

Chapter 1: Introduction and Background

1.1 The NEXRAD WSR-88D Polarimetric Radar Network

In the 1990s, the United States Next Generation Weather Radar (NEXRAD) program installed 140 Weather Surveilance Radar-1988 Doppler (WSR-88D) radars throughout the country (Crum and Alberty, 1993). The NEXRAD WSR-88D network provides near complete radar coverage within the CONUS, with the exception of portions of the western United States due to topography. The WSR-88Ds are S-Band 10.7 cm wavelength radars that operate by transmitting rapid pulses of electromagnetic (EM) radiation. The WSR-88D radars operate to ranges of 300 km for radar reflectivity at horizontal polarization (Z_H), radial velocity (V_R), and spectrum width (σ_V) measurements. The above three measurements are known as the base moments. The network of WSR-88Ds operate 24 hours a day in various scan strategies depending on the weather situation (e.g. clear air or severe storms). The radar performs full 360° azimuthal sweeps at multiple elevation angles. A completed 360° sweep for every elevation angle is called a volume scan. For more information, the reader is referred to Crum and Alberty (1993).

The WSR-88Ds were initially developed as single polarization radars in which horizontally polarized EM waves were transmitted. More recently in 2013, all of NEXRAD WSR-88D weather radars were upgraded to dual-polarization. WSR-88D radars now transmit EM radiation in both the horizontal and vertical dimensions simultaneously as opposed to only the horizontal dimension for single polarization radars (Kumjian, 2013a). This enables scientists and operational meteorologists to identify the shape, size, and orientation of various hydrometeors within a given radar sampling volume. This upgrade will enable more in-depth research into microphysical processes of precipitating storms, real-time diagnosis of potential severe weather hazards, and improved quantitative precipitation estimation.

Accompanying the upgrade to dual-polarization is a suite of new radar variables:

horizontal and vertical reflectivity ($Z_{H,V}$), differential reflectivity (Z_{DR}), differential propagation phase shift (ϕ_{DP}), and the co-polar correlation coefficient (ρ_{HV}). The reflectivity factors provide information on the size of hydrometeors (i.e. $Z \sim D^6$) in a sampling volume as can be seen in the following equation:

$$Z_{H,V} = \frac{4\lambda^4}{\pi^4 |K_m^2|} < |NS_{HH,VV}|^2 > \tag{1.1}$$

Where λ represents the radar wavelength, K_m is the complex refractive index, $S_{HH,VV}$ are the complex scattering amplitudes for backscattered (first index) and incident (second index) EM waves, and N is the number of particles in a cubic meter. The angular brackets $< ... >$ denote the ensemble average (Zhang, 2016).

Z_{DR} reveals information about the shape of the largest hydrometeor in a sampling volume (Seliga and Bringi, 1976, 1978).

$$Z_{DR} = 10 \log_{10} \left(\frac{< |S_{HH}|^2 >}{< |S_{VV}|^2 >} \right) \tag{1.2}$$

Since Z_{DR} is defined as the logarithmic ratio of the reflectivity factors at horizontal and vertical polarizations, positive values of Z_{DR} indicate the presence of hydrometeors whose horizontal axis is greater than its vertical axis (e.g. an oblate raindrop or pristine ice crystal). Precipitation particles typically fall with their longest axis oriented in the horizontal. When particles viewed by the radar beam have a larger vertical scale compared to the horizontal scale (e.g. conical graupel), Z_{DR} values are negative (e.g. Weinheimer and Few, 1987). In the prescence of a strong electric field, pristine ice can also be reoriented into the vertical (e.g. needles) yielding negative Z_{DR} values. The density of hydrometeors in the radar sampling volume also affects Z_{DR}. Since liquid water has a higher refractive index than ice, Z_{DR} values for liquid hydrometeors will be larger than those for ice particles.

ϕ_{DP} measures the amount of phase shift between the horizontal and vertical polarization as the waves propagate through precipitation. Oblate hydrometeors will appear to "slow down" the horizontal beam relative to the vertical beam, giving rise to positive ϕ_{DP}. Typically, for a more visual and informative field, the range derivative of ϕ_{DP} is taken, which is called the specific differential phase (K_{DP}; Jameson 1985) and shown in the following equation:

$$K_{DP} = \frac{1}{2}\frac{d\phi_{DP}}{dr} \tag{1.3}$$

Here, ϕ_{DP} represents the sum of the differential scattering phase and the differential propagation phase. K_{DP} provides information on the size and shape of the most concentrated anisotropic hydrometeor in a sampling volume. K_{DP} is most sensitive to liquid water. Therefore K_{DP} can be considered homogeneous or noisy in regions of dry snow, but can be greater than 0.5 deg km^{-1} in regions of more concentrated pristine ice crystals (Kumjian, 2013a).

Lastly, ρ_{HV} is a measure of the diversity of hydrometeors within a sampling volume, including large variations in orientation, phase, or shape. ρ_{HV} measures the correlation between the vertical and horizontal co-polar received signals based on the following equation:

$$\rho_{HV} = \frac{< S_{HH}^{*} S_{VV} >}{(< |S_{HH}|^2 >< |S_{VV}|^2 >)^{\frac{1}{2}}} \tag{1.4}$$

Where S_{HH}^{*} represents the complex conjugate. ρ_{HV} values vary from 0 to 1 with more uniform scattering targets producing ρ_{HV} values close to 1 and non-meteorological scatters much less than 1. ρ_{HV} may also be reduced in mixed phase regions (i.e., those containing both water and ice in radar sampling volume).

Several unique signatures of dynamical and microphysical processes within storms have been documented using the polarimetric variables (Kumjian and Ryzhkov, 2008). Two very common signatures seen in convective storms are Z_{DR} columns (e.g. Hall et al., 1984; Caylor and Illingworth, 1987; Brandes et al., 1995; Kumjian and Ryzhkov, 2008) and K_{DP} columns (e.g. Hubbert et al., 1998; Loney et al., 2002; Kumjian and Ryzhkov, 2008). Both signatures are characterized by a column of highly positive values extending above the environmental freezing altitude and represent the lofting of supercooled water by convective updrafts. The K_{DP} column has also been attributed to hail stones shedding liquid water as they melt (Rasmussen and Heymsfield, 1987; Hubbert et al., 1998). Z_{DR} columns often contain wet graupel and hail and large raindrop hydrometeors (e.g. Brandes et al., 1995; Loney et al., 2002). ρ_{HV}, apart from being arguably the best indicator between meteorological and non-meteorological scatterers, is most widely known for identifying the "bright band" seen in stratiform precipitation (Fabry and Zawadzki, 1995; Heymsfield et al., 2015). The radar bright band can be easily identified as a reduction of ρ_{HV}, or an enhancement in Z_H and Z_{DR}, due to the presence of mixed-phase hydrometeors, commonly melting snow aggregates. For a more in-depth review of the dual-polarization variables, their applications, and their caveats, the reader is referred to the review presented by Kumjian (2013a,b,c) or textbooks (e.g. Bringi and Chandraseker, 2001; Zhang, 2016).

1.2 Mesoscale Convective Systems

1.2.1 Kinematic and dynamical characteristics

The structure and dynamical characteristics of mesoscale convective systems (MCSs) have been studied extensively in the tropics and midlatitudes (e.g. Zipser, 1969; Houze, 1989; Houze et al., 1989; Biggerstaff and Houze, 1991; Houze, 2004). MCSs have been broadly defined as a cumulonimbus cloud system that produces a contiguous precipitation area approximately 100 km or more in at least one direction (Houze, 2004). MCSs form when individual cumulonimbus clouds conglamorate and organize upscale into a single cloud system with a very large cloud structure and subsequent precipitation structure. When viewed from radar, MCSs typically contain precipitation generated from both convective and stratiform processess (Houze et al., 1990; Houze, 2004). MCSs garner broader interest and relevance because of their impact on society during the warm-season via severe and/or hazardous weather they produce. MCSs are among the largest storms containing convection, last for several hours, and can account for a substantial amount of precipitation. In fact, approximately 60% of the warm-season precipitation in the U.S. Central Plains has been attributed to MCSs (Fritsch et al., 1986).

Parker and Johnson (2000) found that the most common MCS type in the U.S. is the leading line trailing stratiform (LLTS) MCS (Fig. 1). There are other archetypes of MCSs, including the mesoscale convective complex (MCC; Maddox 1980) which is similar to the LLTS MCS in terms of physical characteristics. However, when viewed from visible and infrared satelitte imagery, MCCs exhibit expansive, circular cold cloud top temperatures and convection that is typically not organized into lines. A MCS known for its damaging straight-line winds is the bow echo. The convective line of the system bows outwards owing to strong storm-relative rear-inflow associated with strong cooling in the midlevels (Weisman, 1993, 2001).

Two ideal schematics showing the common structure and airflow trajectory patterns within LLTS MCSs are shown in Figure 1. First, a front-to-rear ascending flow originates at the leading edge of the gust front which then travels through the convective region into the upper-levels of the stratiform region. Strong upward motion is exhibited within the convective region with a broad mesoscale updraft above the freezing level in the stratiform region associated with latent heat release. Secondly, a rear-to-front descending flow originates at the base of the stratiform cloud terminating near the leading convection (Smull and Houze, 1985, 1987). The rear-to-front flow (commonly referred to as a ”rear inflow jet” or RIJ) arises as a dynamical response to the mean heating within the convective line (Schmidt and Cotton, 1990; Pandya and Durran, 1996; Fovell, 2002). Transfer of horizontal mid-level momentum also may enhance the RIJ, especially in cool-season MCSs (Johns, 1993). Microphysical processes (i.e. evaporation/melting) alone do not initiate the RIJ, but they can increase the intensity of the RIJ and force it to descend. The RIJ and precipitation induced cold pool have been been shown in theoretical modeling studies to be vital components in MCS longevity (Rotunno et al., 1988; Weisman et al., 1988).

There have been studies examining the mode of MCS development (Bluestein and Jain, 1985; Bluestein et al., 1987) along with the common modes of MCSs after development (Parker and Johnson, 2000). Parker and Johnson (2000) developed a classification of the three common linear MCSs based upon their distribution of stratiform precipitation and discussed the thermodynamic environment in which each form in along with the corresponding mesoscale flow patterns. Those three common archetypes are the classic LLTS, leading stratiform (LS), and parallel stratiform (PS). They concluded that the LLTS mode is the most frequently observed MCS archetype (60% of all MCSs in their study), is characterized by the strongest instability, and has the lowest LCL heights. The authors also determined most MCSs eventually evolve into the LLTS type before dissipating. The LLTS type can be considered symmetric or asymmetric depending on the relative position of the convective line to the stratiform precipitation. Many asymmetric LLTS systems, those with stratiform precipitation located preferentially towards one terminus of the convective line, develop a broad circulation in the middle levels at the base of the stratiform cloud known as a mesoscale convective vortex (MCV). The MCV forms to due strong differential heating (Zhang and Fritsch, 1987; Bartels and Maddox, 1991) and can sometimes support development of new MCSs within the long-lived vortex in the hours following the demise of the parent MCS (Fritsch et al., 1994).

1.2.2 Microphysical characteristics

Associated with the common airflow patterns within MCSs are microphysical patterns. Much of the knowledge related to microphysical processes within MCSa can be attributed to numerous field campaigns such as the Bow Echo and Mesoscale Convective Vortex Experiment (BAMEX; Davis et al. 2004), Preliminary Regional Experiment for Storm-scale Operational and Research Meteorology program (PRE-STORM; Cunning 1986), and lastly the Midlatitude Continental Convective Clouds Experiment (MC3E; Jensen et al. 2015). In these campaigns, both ground-based mobile equipment and aircraft observations from the NOAA P-3 were used to document the kinematic, dynamic, and microphysical processes of MCSs. Aircraft observations from these studies were able to sample the stratiform region well, documenting particle size distributions (PSDs) and physical characteristics of individual particles (or "habits") from particle imagery.

MCSs typically contain both convective and stratiform precipitation and develop mesoscale circulations as their lifecycle progresses. The convective region consists of numerous intense updrafts producing moderate to heavy precipitation and sometimes sporadic hail near the surface. The convective updrafts loft liquid water above the environmental freezing altitude, where the liquid becomes supercooled. If the supercooled water than collides with and collects upon ice particles (i.e. riming/accretion), ice particles grow and may become graupel particles if additional collision and collection of supercooled liquid occurs. Heavy riming of graupel leads to the formation of hail which is seen in strong convective updrafts. If the updrafts are weak, hail will not be able to grow to appreciable sizes and will subsequently melt before reaching the surface. Stronger updrafts can allow for growth of hail to larger sizes, but if the updrafts are too strong, the hailstones can be detrained from the convective region prior to large growth.

The stratiform precipitation originates from the decaying, but still buoyant, convective cells and also from the broader-sloping front-to-rear ascent. Denser and more rapidly falling hydrometeors fall closer to the convective core whereas the less dense ice crystals within the convective region aloft are detrained and advected downstream to "seed" the stratiform region (Rutledge and Houze, 1987; Houze, 1989). This seeding is very important to the stratiform precipitation process as discussed by Rutledge and Houze (1987) and Yuter and Houze (1995). Since the ice particle terminal velocity is greater than the mean vertical motion, which is on the order of 10's of cm s^{-1} (Houze, 1989), the particles will descend through the stratiform cloud and grow via vapor deposition. As the particles approach the environmental freezing temperature, they begin to aggregate to become large snowflakes (Houze and Churchill, 1987). The particles can also grow via riming slightly above the melting level, however this growth mechanism is far less prevalent compared to the convective region (Leary and Houze, 1979; Houze, 1997). As the larger snowflakes descend through the melting level within the stratiform cloud, they melt and reach the ground as light to moderate liquid precipitation.

Microphysical processes directly impact bouyancy and convective fluxes through condensate loading and latent heating/cooling (Bryan and Morrison, 2012). These impacts are felt and can change the dynamical characteristics of organized convection. The biggest and most notable impact is through the development of the low-level cold pool. The low-level cold pool is driven by diabatic cooling, primarily associated with the evaporation of raindrops and the melting of snow aggregates. The balance between the low-level cold pool and environmental shear is argued to be important in MCS sustainability and evolution (e.g. Rotunno et al., 1988).

1.2.3 Microphysics studies using polarimetric radar observations

There have been recent studies using polarimetric radar observations to understand the bulk microphysics of MCSs, particularly focusing on tropical convection associated with the Madden Julian Oscillation (MJO) and convection in West Africa (e.g. Bouniol et al., 2010; Evaristo et al., 2010; Rowe and Houze, 2014; Barnes and Houze, 2014). However, to our knowledge, there have not been any studies examining bulk microphysics of a large number of MCS events over the middle latitudes.

Rowe and Houze (2014) were able to show that the frequency of different hydrometeor types varied with storm size and MJO acitivity, however the mean hydrometeor vertical profiles did not vary a considerable amount unless the radar echo was partitioned into convective and stratiform components. Barnes and Houze (2014) (hereafter BH14) took the study one step further and analyzed the microphysical characteristics of mature MJO convection by compositing polarimetric radar data and identifying hydrometeor distributions in relation to the important mesoscale airflow patterns within MCSs. The authors used the NCAR Particle Identification (PID; Vivekanandan et al. 1999) algorithm to identify the most likely hydrometeor species within a given radar sampling volume. Figure 2 shows the results of BH14 synthesized into a schematic for both the convective and stratiform regions of mature MCSs associated with the MJO. Features to note within the convective region include the absence of hailstones, the lack of enhanced graupel concentrations, and the presence of wet aggregates. While its been documented that MCSs are kinematically similar throughout the world, the hydrometeor structure of tropical MCSs most likely differs from continental MCSs because of the differences in aerosol content, thermodynamic profile, and convective intensity between marine and continental air masses (Zipser, 1977; LeMone and Zipser, 1980; Zipser and LeMone, 1980; Keenan and Carbone, 1992; LeMone et al., 1998).

An important caveat of the BH14 study was that they were unable to comment on the how the hydrometeor frequency distributions varied during the storms' lifecycle. The composites were created from fixed azimuth range-height indicator (RHI) scans. Specifically, the authors only allowed 1 RHI scan to be indicative of the entire storm. As a result of this cross-section composite approach, they were not able to examine the systems in their entirety. With the NEXRAD WSR-88D network, we will be able to show how the hydrometeor frequencies vary during the lifecycle of a given MCS over the CONUS, accounting for the complete volume of each storm.

As a follow up to their observational study, Barnes and Houze (2016) performed a comparison of observed and simulated ice microphysical processes in tropical oceanic mesoscale convective systems. They found that within the stratiform region, the general layering of microphysical processes was similar between the observations and simulations. However, differences appeared in terms of the microphysical processes themselves, specifically the locations of riming and aggregation. It is to our knowledge that this was the first paper to compare simulated spatial patterns of microphysical processes to polarimetric radar observations within MCSs. This warrants motivation to examine how the observed hydrometeor distributions from continental midlatitude MCSs compare to idealized MCS simulations.

Evaristo et al. (2010) examined polarimetric signatures of West African squall lines. The authors also used the NCAR Particlr Identification (PID; Vivekanandan et al. 1999 algorithm for hydrometeor classification system to determine microphysical characteristics. The authors found strong Z_{DR} and K_{DP} columns co-located with high Z_H values within the convective region of the MCS suggesting the presence of a high concentration of large rain drops. They found heavy to moderate rain and sometimes sporadic hail dominates below the melting level in the convective region, whereas above the melting level the most dominate hydrometeor type was graupel owing to riming by strong updrafts. This differs from the study of BH14 who found that dry aggregates are the most dominant hydrometeor type above the melting level. The difference could have been a result of the type of hydrometeor classification used, or it could stem from the fact that one system occurred over land while the other occurred over water. Differences would arise in terms of instability and wind shear (e.g. deep-layer and low-level).

1.3 Microphysics in models

The representation of microphysical processes in numerical models is typically accomplished through the use of a bulk or bin parameterization scheme. Bulk schemes are computationally inexpensive and assume the shape of a particle-size distribution (PSD). The most common PSD employed in bulk schemes is the gamma distribution (Milbrandt and Yau, 2005a,b) or a modified version of it by varying certain shape parameters. Bulk parameterizations predict one or more moments of the PSD (e.g., mass mixing ratio, number concentration). A single moment (SM) scheme typically predicts mass mixing ratio (q), where as a double moment (DM) scheme typically predicts q and also the number concentrations (N_T) of the hydrometeor species. Generally, the more moments predicted, the more realistic microphysics representation by a bulk microphysics scheme. This is particularly true for simulating MCSs as Morrison et al. (2012) have shown that a DM scheme is needed to accurately portray the trailing stratiform region. Alternatively, bin schemes explicitly predict the evolution of the size distributions by discretization of the distribution into multiple size bins, allowing for shapes that conform to a wide variety of functional forms and may contain more than one mode (e.g. Khain et al., 2004). However, these schemes are computationally expensive (often more than 50 times as computationally expensive as a bulk scheme) and are thus generally only used for research applications.

The physical characteristics of MCSs have been reproduced in previous modeling studies. Several studies have shown that ice-phase microphysics along with a DM microphysics scheme must be included in order to obtain representative storms, especially for capturing the stratiform precipitation region (e.g. Fovell and Ogura, 1988; McCumber et al., 1991; Morrison et al., 2009). However, even with the inclusion of ice-microphysics, simulating the characteristics of these systems has not been reliable since their structure is sensitive to the precise representation of ice processes (Chen and Cotton, 1988). Seeing as how there are a plethora of bulk schemes that have been developed and used in MCS studies, the differences in hydrometeor distributions amongst the schemes can be large (Weverberg et al., 2013).

1.4 Motivation

It is to the authors knowledge that there are limited studies utilizing a large dataset of polarimetric radar observations and linking those observations to microphysical processes within continental MCSs over the CONUS. Admittedly, this may be due to the WSR-88D radar upgrades to dual-polarization having been completed only recently in 2013. Previous studies have used single cases to arrive at their conclusions, largely from the field campaigns listed previously. While this approach can allow for an in-depth analysis of a single event, conclusions drawn from a single case are often not representative of a large number of storms. There are inherent variabilities when trying to infer hydrometeor distributions within storms due to differing environmental characteristics, synoptic forcing, and organization. However, analyzing multiple cases and creating composites allows for more general conclusions to be drawn.

Aircraft observations also have drawbacks, including generally not being able to sample the convective region, and limited temporal and areal coverage since the observations are dependent on the aircraft's flight pattern. Using polarimetric radar observations would alleviate these issues, with some potential loss of information at the smallest spatial scales due to limitations of radar sampling (i.e., remote sensing). There are also limitations due to the particles combined scattering characteristics. In particular, scattering characteristics are dominated by larger sized particles, such that radar observations may not always represent the "dominant" hydrometeor type within a volume (e.g., in terms of number and/or mass).

In this study, we leverage polarimetric NEXRAD WSR-88D observations to better understand the bulk distributions of hydrometeors within continental mesoscale convective systems over the CONUS. We employ techniques to merge individual radar observations into large-area, three-dimensonal composites for analysis (Homeyer, 2014; Homeyer and Kumjian, 2015), a fuzzy logic hydrometeor classification algorithm (HCA; Park et al. 2009), and a novel radar echo classification algorithm (Starzec et al., 2017) to enable a detailed physical understanding. Bulk distributions of hydrometeors within MCSs are examined in terms of the thermodynamic environment in which they form, their lifecycle, seasonality, and geographic location.

This study also seeks to examine how bulk hydrometeor distributions are represented in an idealized model, and how they compare to WSR-88D observations. At times, microphysics parameterizations fail to reproduce observed microphysical processes. These processes influence the dynamics of the MCS, which in turn affects the evolution and longevity of the system. It is therefore paramount to make sure hydrometeor distributions and the associated microphysical processes represented by a model are similar to the observations. The Weather Research and Forecasting model (WRF; Skamarock et al. 2008) and a polarimetric radar data simulator (PRDS; Jung et al. 2008b,a, 2010) is used to facilitate more direct comparisons between the model output and the radar observations.

The conclusions drawn from this study, and future studies of this kind would potentially enable improvements in the representation of microphysics in our models, thus yielding more realistic simulations of precipitation and, hopefully, severe and/or hazardous weather associated with MCSs.

We begin by discussing the methods of both the model and observational analysis in chapter 2. The modeling is discussed first in chapter 3 in order to show hydrometeor distributions from the model using different microphysical parameterizations and to demonstrate how model output and simulated polarimetric variables can be used to make modifications to the P09 HCA to improve its performance with observations. The observational analysis is then presented in chapter 4. Lastly, this study concludes with a discussion in chapter 5.

Chapter 2: Data and methods

This chapter highlights the data and methods employed in this study for both the idealized model and observational analyses.

2.1 Idealized model simulation setup

The Weather Research and Forecasting model (WRF; Skamarock et al. 2008) was used in this study to simulate a 2D idealized squall line subject to four different microphysics parameterizations: Thompson (THOMPS; Thompson et al. 2008), Milbrandt and Yau (MBY; Milbrandt and Yau 2005a,b), Morrison (MORR; Morrison et al. 2005, 2009), and lastly the National Severe Storm Laboratory (NSSL; Mansell et al. 2010; Mansell 2010) with cloud condensation nuclei (CCN) (NSSL$_{CCN}$) and without CCN (NSSL$_{DM}$). These parameterizations were used simply because they were the only parameterizations compatible with the PRDS. THOMPS is partially a DM scheme as it predicts N_T and q for rain. However, all other species are SM as only q is predicted. MBY is a DM scheme that predicts bulk quantities for cloud water, cloud ice, rain, snow, graupel, and hail species. MORR follows the MBY scheme however there is a ”switch” for the rimed ice category which can either represent graupel or hail. For this study's purpose, rimed ice within the MORR scheme represents graupel. Lastly, the NSSL scheme is DM and predicts all similar species as MBY.

The main advantage in using a 2D simulation (as is done here) is that a large number of simulations can be run at minimal computation cost while not losing any of the essential characteristic dynamics and structure of the system (Weverberg et al., 2012). However, there are some limitations of 2D simulations. In particular, 2D simulations omit the Coriolis force and thermal stratification in the initial environment (Mahoney et al., 2009), which is not strictly representative of observed midlatitude environments. The 2D idealized simulations do not take into account day/night given the stable environment and boundary conditions which have an influence on the vertical wind shear.

All simulations were run for 12 hours. Simulations were run on a 1000 km grid with 250 m horizontal resolution and 100 vertical levels with a time step of three seconds. The system was initiated by a 3 K thermal bubble 4 km in width and 1.5 km in altitude. The Weisman and Klemp (1982a) sounding was used as the input sounding. Lower stratospheric moisture in the sounding was unrealistically high, and was therefore reduced to a constant value of 5 ppm. There was no cumulus parameterization scheme used. The long-wave and short-wave radiation parameterization chosen was the rapid radiative transfer model for general circulation (RRTMG; Iacono et al.,2008). Gravity wave damping in the upper 5 km of the vertical domain was included to prevent reflection of waves off the model top.

The microphysical variables, along with the state variables from the model output, can be used to simulate polarimetric radar variables using a polarimetric radar data simulator (PRDS; Jung et al. 2008b,a, 2010). The T-matrix method (Vivekanandan et al., 1991) is used to calculate complex scattering amplitudes for both rain and ice species via numerical integration over the PSDs. Currently, the PRDS only performs scattering calculations for rain, snow, graupel, and hail categories. Cloud ice and cloud water are not currently implemented in the simulator, however implementation in the future is expected as both species are important in the precipitation process (Zhang, 2017 personal communication). Lack of scattering calculations for cloud ice species limits our analysis to non-ice species as a result. This limitation becomes more important for hydrometeor classification as discussed later in the text. There are also other uncertainties and limitations with the polarimetric radar data simulator including the representations of canting and aspect ratios in certain species. The formulations for these may need refinement in the future as they can affect microphysical evolution. For more details on the methods employed for the PRDS, readers are referred to (Jung et al., 2008b,a).

2.2 Polarimetric radar observations and composites

This study utilizes level II dual-polarization radar observations from the NEXRAD WSR-88Ds to quantify bulk hydrometeor distributions of 34 continental midlatitude MCSs. The high resolution radar composites were created by merging all individual radar observations onto a common large-area grid following the methods outlined in Homeyer (2014) and Homeyer and Kumjian (2015). To summarize briefly, observations within 300 km in range from each individual radar contributing to the domain of an MCS throughout its lifecyle were binned in space and time at five minute intervals on a 0.02° × 0.02° ($\sim$2 km) longitude-latitude grid with 1 km vertical resolution. The radar observations were weighted spatially in range using a Gaussian weighting scheme. Only observations within 300 km of a radar were used.

The composites retained all observations including false echoes and biological scatter. Non-meteorological echo is removed prior to analysis using an approach based on that outlined in Zhang et al. (2004). First, contaminated observations were identified by ρ_{HV} values less than 0.80 for Z_H values of 40 dBZ or greater and for ρ_{HV} values less than 0.95 for Z_H values less than 25 dBZ. A second pass then identified regions where Z_H was less than 10 dBZ for any altitude up to 4 km. The locations were then flagged and removed. Systematic biases in Z_{DR} were also corrected in the binning process using a natural scatterer approach similar to that in Ryzhkov et al. (2005). For more detail on this bias correction, the reader is referred to the discussion in Homeyer and Kumjian (2015).

The compositing technique employed in this study was ideal for trying to understand the bulk characteristics of these systems. However, given the 1 km vertical resolution, microphysical processes on scales smaller than the composite are missed altogether. In order to resolve fine scale microphysical processes, such as melting in stratiform regions, the vertical resolution needs to be increased. This was accomplished by examining single-radar dual-polarization observations for each MCS at multiple range intervals from the radar: 30, 60 120, and 200 km. Polarimetric observations are typically only reliable to ranges of 120 km due to beam broadening (Loney et al., 2002; Ryzhkov, 2007). Therefore, the near range intervals (30 and 60 km) provide the highest resolution of the lower troposphere reaching to altitudes of ~ 10 km, while the far range interval of 200 km served as a comparable range to the composite field. The same methods and analysis techniques outlined hereafter were applied, but with the enhanced vertical resolution of 250 m versus 1 km in altitude from the composites. A comparison between the two approaches will be discussed in chapter 4.

2.3 Radar echo classification

There have been studies which have sought to accurately classify radar echo as either convective or stratiform (e.g. Steiner et al., 1995; Starzec et al., 2017). For this study, the Storm Labeling in 3 Dimensions (SL3D; Starzec et al. 2017) algorithm was used to classify radar echo as either convective updraft, convection, precipitating stratiform, non-precipitating stratiform, or ice-only anvil. SL3D utilizes polarimetric radar variables and the altitude of the environmental freezing level to classify the radar echo. The algorithm determines convective updrafts by searching for three distinct radar signatures; weak echo regions which can bounded or unbounded, Z_{DR} columns, or K_{DP} columns. Convective and stratiform echo are separated based on the depth of a vertical Z_H column, the echo top altitude, and the intensity relative to surrounding echo. Lastly, ice-only anvil classification are given if $Z_H > 0$ dBZ was only present above an altitude of 5 km.

SL3D was initially developed using 3D radar observations. In order to perform echo classification with the model simulations, we use a different approach. For simplicity, simulated radar echo was only classified as either convective or stratiform by examining vertical velocity (w) threshold values. For locations where $w > 2.0$ ms^{-1}, the echo was classified as convective, whereas other locations were classified as stratiform. Single convective classification grid points were removed via neighborhood averaging and reclassified appropriately to avoid spurious discontinuities.

For the observational component of this study, the radar echo source regions analyzed were labeled as updraft, convective, stratiform, and anvil. The updraft source region simply resembles the SL3D convective updraft classification. The convective source region was comprised of both the convective updraft and convection classification from the SL3D algorithm. The stratiform source region consisted of only the precipitating stratiform classification from the SL3D algorithm. Lastly, the anvil source region was defined to consist of any echo that was classified as non-precipitating (i.e. the ice-only anvil classification and the non-precipitating mixed-phase stratiform classification).

2.4 Evolutionary stage classification

Since the idealized model took time to spin up and the simulated storm did not dissipate before propagating off the grid, only the mature stage of the simulated MCS was analyzed. A 6 hour time block corresponding to when both convective and stratiform precipitation were present was used for the analysis. Therefore, the results from the modeling component of this study are only representative of MCSs in their *mature* stage. Subsequently, only comparisons with the observations for the mature stage will be discussed.

For the observational analysis, an objective method for classifying the lifecycle of each MCS was achieved by computing time series of the mean and median 15 and 30 dBZ convective echo top altitude in conjunction with examining radar reflectivity. The time series were computed only for the convective source region.

The lifecycle stages for the observational component of the study were labeled as developing, mature, and dissipating. The developing stage was defined as the presence of a convective line at least 100 km in any continuous direction, determined by Z_H, along with an increasing trend (i.e. positive slope) in the convective echo top altitude time series. Once the increase in the echo top time series began to plateau, the lifecycle of the system was then classified as mature. In view of Z_H, the mature stage consisted of a well defined stratiform region whereas in the developing stage the stratiform region was beginning to form. Lastly, the dissipating stage was defined as a decreasing trend (i.e. negative slope) in the echo top altitude time series, along with a noticeable decrease in the prominence of the convective line. An example illustrating this method is shown in figure 3. Once the boundary time locations were determined for each stage, all times in between those bounds are used in computing statistical metrics for each life cycle stage.

2.5 Environment considerations

Environmental sensitivity tests were pursued for both the modeling and observational components of this study. For the idealized model simulations, potential temperature and mixing ratio profiles from the initial Weisman and Klemp (1982a) sounding were perturbed to create three distinct MUCAPE regimes as shown in figure 4: low (MUCAPE < 1000 J kg^{-1}), medium or average (MUCAPE ~ 2000 J kg^{-1}), and high (MUCAPE ~ 3000 J kg^{-1}). These ranges were determined by examining histograms of MUCAPE environments from the 34 observed MCS events. The 25th, 50th, and 75th percentile values correspond to the above MUCAPE regimes respectively.

Environmental considerations were taken into account for the observational component of this study by using the North American Regional Reanalysis (NARR; Mesinger et al. 2006). The NARR output is available every three hours with horizontal resolution of 32 km and 29 vertical levels. The NARR output was chosen because of its high spatial resolution compared to other reanalysis datasets, and it was believed to capture the state of the atmosphere better than operational numerical model output such as that from the RAP or NAM. Assimilated atmospheric variables including pressure, temperature, and specific humidity from the NARR output were used to compute most unstable CAPE (MUCAPE). In this study, MUCAPE reflects the state of the thermodynamic environment. The environmental freezing level altitude (0°C isotherm) was also retained which serves as a critical variable for classifying radar echo via the SL3D algorithm and for hydrometeor classification (see chapter 2.6).

MUCAPE was chosen over other forms of CAPE because of the nocturnal and often elevated nature of MCSs. Sometimes, environments where MCSs develop can have near zero surface-based CAPE (SBCAPE), but large MUCAPE. The differences arise due to these convective systems occurring after the time of maximum surface temperature (i.e., nighttime) and can thus be rooted above the stable planetary boundary layer where the nocturnal low-level jet can aid in initiating and sustaining convection (Maddox, 1983; Stensrud, 1996). There can be instances when the MUCAPE and SBCAPE are equivalent, but the goal was to maintain consistency with representation of the thermodynamic environment.

The varying degree of wind shear plays a significant role in evolution and longevity of MCSs (e.g. Weisman and Klemp, 1982b; Weisman et al., 1988; Rotunno et al., 1988). Daytime MCSs are more sensitive to low-level shear whereas nocturnal MCSs are more sensitive to deep-layer shear. This study does not examine the relationship between wind shear and microphysical evolution, if one exists. Rather, we hypothesize the primary driver in microphysical evolution is the amount of instability in the environment (i.e. MUCAPE).

Proximity soundings from multiple cases were examined in different thermodynamic environments and different regions around the CONUS in order to test the robustness of the NARR output. Differences between the environmental freezing level altitude from NARR output and the observations were typically less than 250 m which was well within the vertical sampling resolution of the composites. Comparisons of MUCAPE revealed minimal differences (not shown).

One caveat with using the NARR dataset was the difference in spatial and temporal scales compared to those of the polarimetric radar observations. Though improvements in the resolution of NARR are impossible, these differences were overcome for analysis purposes using linear interpolation in both space and time.

2.6 Hydrometeor classification algorithm (HCA) description

In order to construct hydrometeor frequency distributions, a method for classifying precipitation particles from polarimetric radar observations was needed. Traditionally, this has been accomplished by using "fuzzy logic" algorithms (e.g. Vivekanandan et al., 1999; Park et al., 2009). Since there is a general understanding as to how polarimetric radar values correspond to specific hydrometeor types, classification algorithms can be developed using fuzzy logic (discussed further below). The HCA will typically aim to indicate the most dominant particle contributing to a set of polarimetric radar data. The most dominant particle type identified by the HCA is a good indicator of the microphysical processes at work within a storm.

The HCA used in this study is that implemented operationally for the WSR-88Ds and developed by Park et al. (2009), hereafter P09. The P09 HCA was selected due to the fact that it is the basis for the current operational HCA applied to WSR-88D data. The HCA uses six radar measurements: Z_H, Z_{DR}, K_{DP}, ρ_{HV}, the standard deviation (SD) of Z_{DR} (SD(Z_{DR})), and SD(ϕ_{DP}) to identify 10 different *species*. The hydrometeor *species* are dry aggregated snow (DS), wet snow (WS), ice crystals of random orientation (CRY), graupel (GRA), big drops (BD), light-moderate rain

(RA), heavy rain (HR), and rain-hail mixture (RH). Two non-meteorological species are ground clutter/anomalous propogation (GC/AP), and biological scatters (BS). The fuzzy logic approach for this classification has three steps: 1.) fuzzification, 2.) aggregation, 3.) defuzzification (Zhang, 2016). The fuzzification step involved establishing trapezoidal membership functions for each hydrometeor specie. Each hydrometeor specie has a specific range of characteristic values of each radar variable. Sometimes, these radar variable ranges overlap between multiple hydrometeor species (i.e. RA and GRA regarding Z_H). However, examining the covariability between polarimetric observations helps determine which hydrometeor specie was most likely contributing to the set of polarimetric radar observations. The aggregation step involves summing membership functions for a set of polarimetric radar observations for each specie. The sum represents the total contribution of all the membership functions and represents how likely the input parameters will result for a given specie. The hydrometeor specie with the highest aggregation value is then assigned to the set of radar data and is identified as the most dominant hydrometeor specie (i.e. defuzzification). For more information on the specifics of this HCA, the reader is referred to P09.

In order to assess the microphysical characteristics in a bulk sense, we combine like hydrometeor classification *species* identified by the HCA to more general *classes*. The motivation for grouping like species becomes apparent when performing comparisons with model output where hydrometeor species are simple classes: rain, ice, snow, graupel, and sometimes hail. For updraft and convective radar echo classification, the *classes* are defined as rain, non-rimed ice, and rimed ice. The BD, RA, and HR HCA species are combined to form a hydrometer rain class. GRA and RH are combined to create a rimed ice class, but at times will be left as their own class. The non-rimed ice class is comprised of the DS, WS, and CRY species. For stratiform and anvil echo classification, GA and RH were omitted following P09.

The stratiform and anvil *classes* are defined as rain, dry snow, crystals, and wet snow. Therefore, unlike with convective source precipitation, there is not an "non-rimed ice" class for stratiform precipitation as the individual species are analyzed separately.

Regarding the idealized simulations, the simulated polarimetric radar variables derived from the PRDS are a function of the microphysical variables. A measure to test the accuracy and physicality of the bulk hydrometeor distribution as determined from applying the P09 HCA to the simulated polarimetric radar variables was desired. This was achieved by using the microphysical variables themselves, specifically q. We identify the hydrometeor class with the largest q at each grid point. This method gives the most dominant hydrometeor type, in terms of mass, as predicted by the model. We call this the maximum q approach.

In addition to the differences in what the HCA and maximum q classification measure, there are differences in the types of classifications produced by each method, specifically with hydrometeor species above the freezing level. We therefore try to use a more general class such as "non-rimed ice" in order to avoid these differences. As mentioned previously, the "non-rimed ice" class can be a combination of both CRY, DS, and WS hydrometeor species. For the maximum q classification, the "non-rimed ice" class for convective source regions is comprised of snow *and* ice species. The P09 HCA omits DS in convective source regions which makes the "non-rimed ice" class represent CRY *only* (see P09 for details).

It is important to note that the most dominant hydrometeor type identified by the maximum q approach and the P09 HCA are not expected to be equivalent. Polarimetric variables provide a measurement of the scattering characteristics of a collection of particles within a volume, which may be at various stages of growth and thus, contribute to the radar observation in non-uniform ways (given the dependence of Z and Z_{DR} on particle size). On the other hand, changes in mass of a hydrometeor specie are determined by specific microphysical processes (e.g. growth mechanisms, breakup) and particles may be evaluated separately to determine the most "dominant". Despite these important differences, we expect the results from both methods to be qualitatively similar. If classification differences are exhibited, the P09 HCA membership functions will be modified using the maximum q classification and simulated radar variables to reduce the differences as much as possible. After this, the modified P09 HCA would be applied to the NEXRAD WSR-88D observations.

Initial modifications to the P09 methods were made and applied to fit the observational datasets used in this study and are discussed as follows. 1.) The SL3D algorithm was used for radar echo classification. 2.) The standard deviation of Z_{DR} and ϕ_{DP} membership functions were omitted. 3.) The confidence vector $\mathbf{Q}$ was assumed to equal one in the aggregation process because quality control techniques were addressed through our algorithms developed for the radar composites. 4.) Liquid classifications were not allowed to extend beyond 4 km above the environmental freezing altitude in convective precipitation, and liquid classes were not allowed at altitudes above the environmental freezing level for radar echo classified as stratiform. 5.) The Z_H upper-level membership function value for graupel was modified to 50 dBZ compared to 45 dBZ. 6.) In P09, a melting level algorithm developed by the Nation Severe Storms Laboratory (NSSL) was used in hydrometeor classification. However in this study, the altitude of the environmental freezing temperature provided from the NARR dataset served as a proxy for the melting level altitude. 7.) As a result of modification 6, and the vertical sampling of the composites, the WS hydrometeor class was only allowed to occur within 1 km below the melting level in stratiform precipitation.

Chapter 3: Idealized model simulation analysis

We begin by examining the representation of bulk hydrometeor distributions from a modeling perspective. To motivate the use of modeling in conjunction with the observations, we present two main goals in applying the PRDS in this study.

1. Identify the bulk hydrometeor distributions of an idealized simulated MCS using two forms of hydrometeor classification.

2. Use microphysical variables from the model (i.e. q, N_t) to possibly modify the P09 HCA algorithm that will be implemented for the observational analysis.

3.1 Contour frequency by altitude diagrams (CFADs)

A classic approach to examine radar variables corresponding to convective and stratiform precipitation is the contoured frequency by altitude diagram (CFAD; Yuter and Houze 1995). A CFAD reveals characteristics of the distribution of a given radar variable and its variability as a function of altitude.

Figure 5 shows convective source region CFADs of the simulated polarimetric variables for each microphysics scheme subject to the medium MUCAPE regime. Z_H convective CFADs generally feature a concave distribution with higher Z_H values near the ground decreasing towards cloud top. Frequencies are between 10-20% for high Z_H near the ground extending vertically towards the environmental freezing level, while aloft mid-range Z_H frequencies in the mid troposphere range between 20-40 dBZ before reaching cloud top near 0 dBZ. The THOMPS Z_H CFAD is the weakest of all schemes. THOMPS is a single-moment scheme that does not have a hail specie, implying all rimed ice is graupel. Since graupel has a slower fall velocity compared to hail, Z_H may be reduced closer to the ground (Bryan and Morrison, 2012). Z_{DR} and K_{DP} CFADs below the freezing level contain lower end frequencies for values greater than 1 dB and 0.5 deg km^{-1} respectively. Above the freezing level, both Z_{DR} and K_{DP} achieve their highest frequencies in excess of 50% for values of essentially 0 dB and 0 deg km^{-1}. The ρ_{HV} CFADs reveal high frequencies for values centered at ∼0.98. A broad reduction in ρ_{HV} to ∼0.95 is seen below the freezing level and corresponds to the presence of mixed phase particles (i.e. rimed ice and liquid). This reduction is generally maximized at the -2 km relative altitude bin for all schemes with frequencies in the 30-40% range.

Stratiform source region CFADs were also created from the simulated polarimetric variables and are shown in figure 6. Stratiform precipitation is characterized by a more diagonalized Z_H CFAD above the freezing level compared to convective precipitation, agreeing with previous results by Yuter and Houze (1995). All microphysics schemes contain low-end frequency values for any given Z_H below the freezing level. Above the freezing level, higher frequencies up to ∼30% are exhibited up to 5 km above the freezing level where after Z_H approaches 0 dBZ, similar to the convective region.

The Z_{DR} CFADs for all schemes reveal high frequency values above the freezing level centered on ∼0 dB similar to the convective region Z_{DR} CFADs. Below the freezing level, the NSSL$_{DM}$, NSSL$_{CCN}$, and THOMPS scheme have increased frequencies between the 0-1 dB range compared to the MBY and MORR schemes which feature lower frequencies in the same range, but larger values of Z_{DR}. This implies that more oblate raindrops (i.e. too many large drops in rain PSDs) may be present in the stratiform region for MORR and MBY schemes compared to the other three schemes, a result similar to Putnam et al. (2016). This interpretation is also supported by observational analyses below (e.g., see Fig. 23 and associated discussion). The K_{DP} CFAD contains high frequencies of ∼0 deg km^{-1} throughout the depth of echo.

The most striking feature seen within the stratiform region CFADs are associated with the ρ_{HV} reduction. As mentioned previously, the ρ_{HV} reduction is indicative of the radar bright band signature which typically occurs just below the freezing level. From the CFAD analysis presented here, there is a substantial displacement of the ρ_{HV} reduction from the environmental freezing level altitude, ~1.5-2 km below the freezing level for all schemes except for THOMPS which does not feature a substantial ρ_{HV} reduction. Also interesting, all microphysics schemes contain a region of enhanced Z_{DR} frequencies ~1 km below the freeing level for values between 1-2 dB. We believe the increase in frequencies marks the Z_{DR} identification of the radar bright band. While it is possible for melting to be delayed up to 0.5 km, the 1.5-2.0 km displacement of the ρ_{HV} reduction (and melting layer) is unrealistic. The microphysical process of melting may in fact be too slow in some, if not all of the microphysics schemes examined here. This feature has been noticed in previous literature (Jung et al., 2010), but to our knowledge has not been addressed further.

As alluded to in section 1.3, near zero Z_{DR} and K_{DP} and high ρ_{HV} above the freezing level are expected because the PRDS does not compute scattering calculations for cloud ice and cloud water. Subsequently, no true shape information from the simulated polarimetric variables above the freezing level exists. Once the P09 HCA is applied to the simulated radar data, we expect to see an over classification of dry-snow aggregates in the stratiform region owing to their spherical nature (i.e. Z_{DR} ~0 dB). Since there is limited shape information above the freezing level, there is little confidence in modifying the unrimed ice species membership values of the P09 HCA. Until cloud ice and cloud water are added to the PRDS package, we can only modify and test the robustness of the implemented P09 HCA for species below the freezing level.

3.2 Hydrometeor frequency distribution analysis

In this section, the P09 HCA is applied to the set of simulated polarimetric radar data for each microphysics scheme and for each source of precipitation. The maximum q approach derived from the microphysical variables is also shown.

3.2.1 Convective source region

Convective source region bulk hydrometeor distribution profiles for both the maximum q method and the simulated polarimetric variables subject to the P09 HCA for all microphysics schemes and the medium MUCAPE regime are shown in figure 7 and figure 8, respectively. While there are differences among each microphysics scheme, both HCA approaches produce similar profiles of all the three major hydrometeor species considered. Below the freezing level, liquid frequencies are the largest indicating that liquid hydrometeors are the dominant hydrometeor class, agreeing with previous studies (e.g. Straka and Zrnic, 2000; Evaristo et al., 2010; Barnes and Houze, 2014). Both approaches contain a “rimed ice nose” which reaches maximum frequencies between 0-3 km above the freezing level for all microphysics schemes. In fact, when partitioning the rimed ice class into its components, the rimed ice nose is actually a “graupel nose” as shown from figure 9 and figure 10. The frequency magnitude and vertical extent of the graupel nose are greatest for the MORR and MBY schemes in the maximum q approach (fig. 9). Similar graupel noses are seen among all microphysic schemes when applying the P09 HCA to the simulated polarimetric variables (fig. 10). Above the graupel nose feature, the non-rimed ice class becomes the most dominant hydrometeor class.

There are differences in the mean values when comparing the two different HCA approaches, specifically for both NSSL simulations and the THOMPS simulation. The P09 HCA overestimates the vertical extent and frequency magnitudes of the graupel nose feature compared to the maximum q approach for these schemes. However, the MORR, THOMPS, and MBY schemes compare quite well between the two HCA approaches. Even with the mean difference between both HCA approaches, the model expects graupel to be the most likely hydrometeor type $\sim$0-3 km above the freezing level similar to West African convection (Evaristo et al., 2010), but different than tropical convection (Barnes and Houze, 2014).

The biggest differences between the two HCA methods arises near the surface where excessive rimed ice is being classified for the P09 HCA approach. Examination of GRA and RH species separately revealed RH was overly classified and highly variable for all schemes using the simulated polarimetric data compared to the maximum q approach (Fig. 10). We attribute this difference to the fact that the RH classification represents a rain-hail mixture, whereas in a model, q_h represents specifically hail. Therefore, the membership functions for the RH class need to be modified to represent specifically hail if future comparisons are to be made. Even within the classification of "rain-hail mixture", hail typically is viewed as the most *dominant* hydrometeor specie owing to its societal impacts.

Along with the issue of over classification of rimed ice near the surface, the MBY scheme contains larger frequencies of hail being identified as the most dominant hydrometeor type amongst all schemes which predict a hail specie (fig. 9). Owing to the larger fractions of hail, more mass would need to be melted which could make the cold pool stronger, thus increasing the system propagation speed (Weverberg et al., 2012). The NSSL simulations in comparison have less hail, stemming from the fact that this parameterization treats the conversion from graupel to hail differently than MBY (i.e. see Eqs. A48-49 and discussion of Mansell et al. 2010).

Scatter plots of the simulated polarimetric variables, Z_H and Z_{DR}, for the locations where q_h was classified as the most dominant hydrometeor type were analyzed to address possible modifications for a pure hail classification category. An example of a convective source region scatter plot from the MBY scheme is shown in figure 11). It is evident from the scatter plot that the hail specie in the model is largely characterized by simulated Z_{DR} less than 1 dB for Z_H greater than 45 dBZ below the freezing level. Rain (liquid) species are characterized by higher simulated Z_{DR} values much greater than 1 dB for increasing Z_H.

Originally in P09, the membership function range of Z_{DR} for RH were a function of Z_H and could be as high as 4 dB for large values of Z_H. Based on the scatterplot analysis, changes to the RH mixture to represent hail alone resulted in restricting the Z_{DR} membership function values to be between 0-1 dB. Subsequently, the Z_{DR} membership function was no longer a function of Z_H as was in P09. From this point on, the hail specie will be referred to as HA.

Recreating the bulk hydrometeor profiles with the new HA specie similar to figures 9 and 10, vast improvements are seen below the freezing level altitude as the excessive rimed ice classifications near the surface is removed (Fig.12). The resulting rimed ice profile is now comparable between both the maximum q approach and modified P09 HCA below the freezing level. Separating the rimed ice class into graupel and hail species reveal that reducing the Z_{DR} membership function values yields a more representative and realistic vertical distribution of hail for MCSs (Fig.13). Since hail is not observed as frequently near the surface for MCSs as it is with other forms of convection (e.g. supercells), the excessive hail classifications near the surface were removed while the general shape of the hail profile began to resemble a Gaussian distribution. For any given altitude, hail frequencies were never above 22%. We therefore are confident with implementing these changes into the HCA for the observational analysis to follow in chapter 4.5.1.

3.2.2 Stratiform source region

A similar analysis to that of the convective source region was performed for the stratiform source region for all microphysics schemes as shown in figure 14 and figure 15 . Below the freezing level, liquid species are generally the dominant hydrometeor class. For the maximum q approach, snow was classified as the most dominant hydrometeor class from ~0-5 km above the freezing level, thereafter the most dominant hydrometeor class becomes ice for MORR and both NSSL schemes with little variability. However, THOMPS is different. The snow specie is dominant until ∼7 km above the freezing level, where after ice crystals and snow are classified almost equally along with high variability near cloud top. The reason for this may be due to the fact that THOMPS is a SM scheme. Morrison et al. (2009) discussed that DM schemes have faster growth rates of ice compared to SM schemes during the mature stage of the MCS owing to an increased mesoscale updraft in the updraft region. Therefore, we see an abundance of the ice class near cloud top for all schemes except for THOMPS.

Snow fractions were also classified to altitudes of ∼-2 km below the environmental freezing level for all microphysics schemes which agrees with the stratiform CFAD profiles shown in figure 6. We stress that these results are most likely not physical, but they again reinforce the need to re-evaluate the melting processes in microphysics schemes in future studies. The maximum q approach also classifies low-end fractions of graupel, with a maximum of $\sim 10\%$ occurring within close proximity to the freezing level.

Examining hydrometeor classification from the P09 HCA (Fig. 15), dry snow is classified as the most dominant hydrometeor class throughout the entire storm above the freezing level for all schemes, whereas the crystal class frequencies were virtually non-existent, specifically just above the freezing level. This differs tremendously from the maximum q profile, which classified ice species as the dominant hydrometeor class above the 5 km relative altitude bin for most schemes. Again, we attribute these differences to the fact that the PRDS does not compute scattering characteristics for cloud ice and cloud water, thus yielding little to no shape information that is necessary for the P09 HCA to successfully distinguish between pristine ice and aggregates.

Since we simply do not have enough information regarding the shape of the ice and snow particles aloft, we unfortunately are unable to test whether or not the membership functions are correct or incorrect using the PRDS. Only size information (i.e. Z_H) is present, in which overlap between the Z_H membership functions does exist for dry-snow aggregate and ice crystal species. The highest aggregation value will be for the dry snow class as a result.

The P09 HCA also does not allow for graupel to be classified within the stratiform region which is why graupel classifications are absent within the stratiform region in figure 15. This condition was relaxed in order to test the membership functions of the GRA HCA classification. Figure 17 shows the new stratiform region with the inclusion of graupel. As a first pass, graupel fractions are comparable to the maximum q approach. The maxima were generally just above the freezing level, which was in the same location as the maximum q HCA approach. This agrees with past observational studies along with the results found by Barnes and Houze (2014) for tropical MCSs. Given the similarities between both approaches and the vertical distribution being similar to previous observations, we feel confident in allowing the stratiform region to contain graupel classifications for the observational analysis up to 2 km above the freezing level.

3.2.3 Environment Sensitivities

Figures 18 and 19 show the difference of the mean hydrometeor frequency distribution profiles between high and low MUCAPE regimes for all microphysics schemes for the convective source region. A positive difference indicates that the frequencies of a given class was larger for more unstable environments, while a negative difference resembles the opposite relationship. All schemes except the THOMPS scheme reveal a positive difference value for graupel throughout the depth of the MCS for both the maximum q approach (fig. 18) and the modified P09 HCA method (fig.19). This indicates that higher frequencies of graupel were being classified for environments with greater instability. As a result of increased graupel frequencies, non-rimed ice frequencies begin to decrease aloft and liquid frequencies decrease below the freezing level. Liquid frequencies increase slightly above the freezing level for the more unstable environments whereas below the freezing level, liquid frequencies decrease owing to increased fractions of graupel and hail. The more unstable the environment (i.e. larger MUCAPE), the greater the potential for stronger updrafts to loft liquid hydrometeors higher, and possibly more numerous amounts of drops, above the freezing level.

Chapter 4: Observational results

In this chapter, we take the updated P09 HCA and apply it to the 34 MCS cases identified in Table 1. Similar analysis techniques are performed as discussed in chapter 3. The goals here are to:

1. Identify the bulk characteristics of midlatitude continental MCSs in the CONUS based on radar echo classification, lifecycle evolution, geographic region, and time of year (i.e. seasonality).
2. Compare the observational results to those of the model simulation where appropriate.

4.1 Contour frequency by altitude diagrams (CFADs)

4.1.1 Radar composites

CFADs were computed for each of the four polarimetric radar variables for every case and for each radar echo source region. The frequency distributions for each case were then composited together via weighted averaging to create overall CFAD composites for each radar echo source region as a function of evolutionary stage.

Figure 20 shows the composited CFADs for the convective source region. Within the convective region, the Z_H CFAD is generally characterized as a vertically oriented feature sloping to lower Z_H values with altitude. Frequencies range from ∼5-30% in the reflectivity range of 15-50 dBZ, with maximum frequencies near 40 dBZ at the lowest altitudes. During the lifecycle of the MCS, the width of the CFAD contracts slightly as higher values of Z_H above the freezing level become less frequent. The maximum frequencies from 0-6 km above the freezing level increase as the lifecycle of the system progresses.

Z_{DR} values in excess of 2 dB are seen below the freezing level, indicative of convective precipitation. Given the slightly elevated frequencies of Z_{DR} greater than

1 dB above the freezing level, some of the frequencies exhibited may be associated with Z_{DR} columns. Approximately within the 0-6 km relative altitude range, the Z_{DR} CFAD is characterized by high frequencies in excess of 35% between 0.0-0.5 dB. The widening of the Z_{DR} CFAD aloft near cloud top in conjunction with decreasing Z_H are indicative of pristine ice hydrometeors (e.g. Straka and Zrnic, 2000). As the lifecycle of the system progresses, Z_{DR} values of $\sim$1 dB become more frequent below the freezing level.

The K_{DP} CFAD profile generally is centered on 0 deg km^{-1} with lower end frequency values for positive K_{DP} values below the freezing level indicating heavier precipitation (e.g. Straka and Zrnic, 2000). Over the life cycle of the system, large K_{DP} values greater than 1 deg km^{-1} below the freezing level begin to diminish. This indicates that the concentration of rain drops or the oblateness of the drops are decreasing as the lifecycle of the MCS progresses. Lastly, ρ_{HV} CFADs were generally characterized by a near-homogeneous vertical CFAD profile. A broad reduction in ρ_{HV} is seen near the melting level and is skewed to altitudes above. The reduction is indicative of mixed phase precipitation, in particular liquid and rimed ice. The broad reduction decreases in vertical extent as the system's lifecycle progresses, indicating that the altitude at which supercooled liquid may be lofted to is decreasing. Higher-end frequencies are centered on $\sim$0.96-0.97 near the surface and aloft which are considered typical values for moderate-heavy rain and pristine ice aloft, respectively.

Stratiform CFADs were also generated in a similar manner to the convective CFADs (Fig. 21). Stratiform CFADS are different from convective CFADs in that the Z_H CFAD is more diagonalized (Yuter and Houze, 1995). The Z_H CFAD contains higher-end frequencies >25% above the freezing level between 5-25 dBZ. The higher frequenices aloft associated with low Z_H values are indicative of the ice crystals advected downstream from the convective region. As these particles descend, they grow via vapor deposition and then aggregation, which increases the size of the particles, as they descend to the environmental freezing level thus yielding larger values of Z_H. Slightly above the freezing level upwards to the 2 km relative altitude bin, the slope of the frequencies becomes smaller indicating the greatest aggregation zone as Z_H increases more rapidly. Just below the freezing level, a sharp increase in Z_H is seen attributed to the increase in refractive index due to the melting of snow aggregates to wet-snow and subsequently liquid precipitation. Peak frequencies below the freezing level are $\sim$30% between 10-35 dBZ. The range of Z_H values also increases as indicated by the width of the CFAD, and expresses the natural variability of liquid particle size.

Z_{DR} CFADs were characterized by a similar profile as the convective source region, although the maximum values of Z_{DR} are not as large below the freezing level. Maximum Z_{DR} values below the freezing level are generally less than 1.5 dB. Aloft, Z_{DR} is closer to 0 dB near the freezing level, which is more representative of snow aggregates, and increases to 1 dB near near the 8 km relative bin which is indicative of horizontally-oriented pristine ice that has been advected downstream from the convective region (e.g. Straka and Zrnic, 2000). As the lifecycle of the MCSs progress, the stratiform Z_{DR} CFAD grows wider (i.e. higher frequencies for higher values of Z_{DR}) above the freezing level indicating that more pristine ice may be present than compared to earlier stages thus representing less aggregation.

CFADs of K_{DP} are generally centered on 0 deg km^{-1} throughout the entire depth of the storm. Below the freezing level, frequencies are centered on zero and appear to become slightly negative above the freezing level. This may be slightly more indicative of vertically oriented particles, although, above the freezing level, K_{DP} is generally a noisy product in the presence of snow. The ρ_{HV} CFAD clearly reveals the location of the radar bright band signature. The reduction in ρ_{HV} occurs just above and below the freezing level to approximately 0.90 during the mature and dissipation stages. Reduction of ρ_{HV} is due to the presence of mixed phase particles in the radar sampling volume (i.e. liquid and ice), whereas the reduction below the freezing level is attributed to melting snow aggregates and mixed phase precipitation of various sizes (e.g. Zrnic et al., 1993; Straka and Zrnic, 2000). The signatures were not as pronounced in the developing stage, but recall the methods employed as the stratiform region should only be well established in the mature and dissipating stages.

4.1.2 Single radar analysis

CFADs were also constructed for times when the MCSs traversed over a single radar in order to evaluate storm characteristics at finer vertical resolutions. The SL3D algorithm classified from the composite was interpolated in space and time to the radar echo at each range gate. The single radars and times for each case were chosen so that the radar captured both convective and stratiform precipitation regions.

The resulting CFADs for the convective and stratiform source regions for observations within 60 km range to the radar are shown in figures 22 and 23 . The overall structure of the CFADs from this perspective resembles the composite approach, as expected. Differences do arise, however, from increased vertical resolution. The convective CFAD generally has reduced frequencies overall compared to the composite perspective. The ρ_{HV} reduction is not as pronounced in the vertical as it does not extend to higher altitudes compared to the composite perspective. There is also more noticable spread in Z_{DR} both above and below the freezing level. The values of Z_{DR} below the freezing level are similar to those in the composite approach. However above the freezing level, frequencies of negative Z_{DR} are seen more frequently than in the composites.

The Z_H CFAD for stratiform precipitation may be slightly more diagonalized (i.e.

more horizontal) compared to the composite version. Frequencies of Z_H around 20-25 dBZ are also larger for the single radar perspective compared to the composite version 0-4 km above the freezing level. The ρ_{HV} CFAD is also centered on higher values of ρ_{HV}, specifically ~0.98 compared to 0.96-0.97 as in figure 21. Higher frequencies of lower ρ_{HV} aloft also increase as lifecycle progresses, indicating more crystals of various orientations are present aloft.

The increased vertical resolution makes the bright band signature more pronounced, especially in the Z_H, Z_{DR}, and ρ_{HV} fields. The ρ_{HV} reduction is contained to within 1 km of the freezing level as opposed to the composites which shows more of a broad reduction over the span of 1.5-2 km. This most likely arises due to the vertical resolution of the composites. Also, K_{DP} resonance is exhibited just below the freezing level and is most likely attributed to wet snow flakes and partially by nonuniform beam filling (Zrnic et al., 1993; Ryzhkov, 2007).

4.2 Bulk hydrometeor frequency distributions

The CFADs provide raw information on the behavior of the radar variables which can also provide verification of our methods employed thus far. The NARR dataset was able to capture the altitude of the environmental freezing level reliably as evident by the location of the bright band signature. Our CFAD profiles also resemble others in previous literature indicating the robustness of the SL3D algorithm in echo classification. Further analyses of the radar variable CFADs in terms of seasonality and geographic region do not change considerably. However, by looking at all of the radar variables in conjunction with each other, we can better assess the bulk microphysical characteristics within the system. Performing this manually would be time-consuming, so we therefore employed the HCA as discussed in section 2.6 with the new modifications described in the modeling chapter 3.

4.2.1 Radar composites

Hydrometeor frequency distributions of all cases merged together via weighted averaging for each radar echo source region are shown in figure 24. Below the freezing level, liquid is the most dominant hydrometeor class for all echo source regions. Liquid hydrometeors are also classified as the dominant hydrometeor class ∼20% of the time above the freezing level in the updraft region. The prescence of liquid hydrometeors above the melting level has been typically observed in updraft regions indicating the primary growth mechanism is accreation. Between 0-6 km above the freezing level (AFL), rimed ice is the most likely hydrometeor class as it is classified over 70% of the time during the developing stage. The "rimed ice nose" can be seen extending over a 6 km layer AFL during the developing stage. As the MCS lifecycle progresses, the magnitude and vertical extent of this feature decreases, and thus the changeover between dominant classes of non-rimed ice and rimed ice is found at lower altitudes. Similar to the model hydrometeor frequency distributions, the rimed ice nose is actually a "graupel nose" as seen in figure 25. From figure 25, we also see that if hail is present, the classification frequencies reach a maximum of ∼5% AFL in the updraft region. The general distribution of hail in the vertical is similar to the model although with lower frequencies.

At altitudes greater than 5km AFL during the mature and dissipating stages, graupel frequencies begin to decrease approaching cloud top as non-rimed ice becomes the most dominant hydrometor class. As the lifecycle of the system progresses, the frequencies of graupel near cloud top begin to decrease. During the developing stage, the graupel classification frequency was ∼30% decreasing to ∼10% by the dissipation stage near cloud top. We cannot comment on the nature of the graupel aloft with certainty (i.e. spherical or conical shape), but the prescence of conical graupel near cloud top has been inferred in previous studies (Homeyer and

Kumjian, 2015).

Plus and minus 1σ values for the frequencies of each class are used to assess the variability in the classification frequencies. Variability is more pronounced within the updraft region compared to any other region as well as near cloud top in any region primarily caused by fewer observations and beam broadening. Variability is also generally larger during the dissipating stage.

The convective region features a similar profile to the updraft region, however the magnitudes and variability of some of the features are reduced. Frequencies for the graupel class are not as high compared to the updraft region above the freezing level. There are also fewer occurrences of liquid classified above the freezing level, $\sim$5-10% depending on the lifecycle stage.

Within the stratiform region, the liquid class is the most dominant hydrometeor class with a classification frequency of 100% within the lowest few kilometers below the freezing level. A small fraction of wet snow of $\sim$10% is observed to occur within 1 km below the freezing level. Graupel was also allowed to be classified in the stratiform up to 2.0 km above the freezing level after the model simulation analysis and previous observational studies. Frequency maxima were close to 10% just above the 0 km relative altitude bin. Above the freezing level, dry aggregated snow is the most dominant hydrometeor class between 0-7 km relative altitude bin reaching maximum classification frequencies of 75-85% after which ice crystals of various orientations become the most dominant class near cloud top. The high fraction of dry snow aggregates near the freezing level is consistent with the favored growth mechanism of aggregation whereas aloft, crystals detrained from decaying convection seed the stratiform region so we expect to see larger fractions of ice crystals aloft. As the MCS lifecycle progresses, the dry-snow aggregate and ice crystal separation between 0-5km above the freezing level decreases as the ice class began to be classified more as the dominant hydrometeor type. As a result, the changeover altitude of the more dominant hydrometeor class decreases.

The anvil region featured a mix of the dry snow and ice classes above the freezing level. In the developing stage, higher frequencies of dry snow were classified between 0-5 km above the frequency level. At cloud top, the ice class had higher frequencies. As the evolution of the system progresses, the two classes become almost equal in occurrence, especially in the dissipation stage. Near the freezing level, liquid classifications were present, however no liquid reached the surface per the definition of anvil in this study.

4.2.2 Single radar analysis

A similar analysis to the composite based hydrometeor distributions was also performed from the perspective of single radars contributing to each event.

Figure 26 shows the overall weighted averaged hydrometeor distributions as would be observed from an individual radar for the convective source region out to ranges of 120 km and 60 km from radar. Below the freezing level, higher frequencies of graupel are classified at the expense of liquid hydrometeors which differs slightly from the results of the composites. Hail frequencies are also slightly higher from the single radar perspective as compared to the composite based perspective. However, the general shapes of the mean profiles are similar between the two perspectives. Decreasing the range to 60 km from radar, thus capturing vertical gradients at finer resolution, the composite and single radar profiles are similar again, except for an increased spread in single radar observations. Above the freezing level, the "graupel nose" is still evident and the shapes of both the non-rimed ice and graupel profiles are similar between both perspectives. There is more variability in the single radar profiles compared to the composite based approach which may be caused by fewer observations.

Examining the stratiform source region further, the mean shape of the profile is consistent with the composite based perspective described previously. The altitudes at which ice and snow dominance begins to changeover is seen at higher relative altitudes for the individual radar perspective compared to the composite approach. Again, more variability is seen with the individual radar approach compared to the composites, especially as range from radar decreases.

4.3 Geographic region distributions

MCS events were grouped into four different geographic regions based on where the system developed in: Central/Southern Plains, Midwest & Ohio River, Northeast, and the Southeast. In the event where an MCS was long lived and able to propagate through one or more geographic regions, the region where the MCS initiated from was considered the geographic region the MCS belonged to.

Figures 27 and 28 show the vertical hydrometeor frequency distribution profiles for the all geographic regions for convective and stratiform regions, respectively. The overall shape of the hydrometeor profiles, including the major features noted previously are similar amongst all geographic regions. Again, this result was similar to that found by Rowe and Houze (2014). Within the convective source region, MCS events in the Central/Southern Plains and Upper Plains generally contain higher frequencies of graupel and hail between 0-5 km above the freezing level and a graupel nose reaching a greater vertical extent compared to southeast and northeast MCSs. Supercooled liquid frequencies are similar amongst the regions, with greater frequencies of the non-rimed ice class classified in northeast and southeast regions at the expense of graupel. Hail frequencies are much larger for both Plains regions compared to the southeast and northeast. Surprisingly however, northeast MCSs contain slightly more hail than the southeast cases. These conclusions may simply be explained by the environment in which these systems form in (i.e. large/small

MUCAPE). Climatologically speaking, MUCAPE tends to be greater in the Central US compared to the southeast which would lead to stronger updrafts and possibly larger accretion rates.

Stratiform source region profiles to do not exhibit many differences when compared among each other and to the overall composites shown earlier. The most noticable difference is seen for northeast MCSs where higher frequencies of ice crystals are classified slightly above the freezing level and near cloud top.

4.4 Seasonality distributions

Each MCS was labeled as either a warm season (JJA) or transition season (MAM and SON) case. MCS vertical hydrometeor frequency distribution profiles were created similar to previous figures.

Figure 29 shows the convective and stratiform region distribution plots for both seasons. As noted with the geographic region distribution profiles, the seasonality distributions look similar to the overall composites in terms of the mean vertical profiles. The graupel nose signatures between both regions appear to reach similar magnitudes and vertical extents for all stages. Lastly, the stratiform region exhibits very few if any differences.

4.5 Environment Sensitivities

A different approach was used to assess the role in which the environment impacts the observed hydrometeor distributions within MCSs. Instead of viewing the system as a whole, only the individual storms within the leading convective line were examined. Individual storm locations within the convective line were identified using 30 dBZ Z_H echo top altitude maxima. Once the storms were identified, all polarimetric radar and hydrometeor classification data within a 24 km radius of the storm were extracted. This method was reproduced for each time step (i.e. every 5 minutes).

4.5.1 Thermodynamic fill profiles

Figure 30 below shows the sensitivity of the hydrometeor frequency distribution for each hydrometeor class to changes in the MUCAPE environment. Only locations where the total number of counts were greater than 50% of the mean number of counts were used in the plot. It is evident that as MUCAPE becomes larger, higher frequencies of graupel are classified at the expense of non-rimed ice above the freezing level. Vice-a-versa, when MUCAPE is relatively low, non-rimed ice frequencies are larger at the expense of graupel above the freezing level. Intuitively, the vertical extent of graupel and hail classes are also higher for more unstable environments.

Below the freezing level, there are some non-intuitive relationships exhibited. Specifically hail and graupel frequencies are relatively higher for low MUCAPE environments. Intuition would lead one to expect that the higher fractions of graupel or hail would be associated with a more unstable environment (i.e. larger MUCAPE). In order to address this interesting feature, the polarimetric radar variables associated with each storm were examined further. Figure 31 reveals that below the freezing level within the region where hail fractions were being classified in low MUCAPE regimes, $Z_H > 50$ dBZ, $\rho_{HV} \sim < 0.95$, Z_{DR} ~1.0 dB, and K_{DP} >1.5 deg km^{-1}. These combination of radar variables would most likely indicate the presence of a large concentration of melting hailstones and graupel particles. The higher values of K_{DP} indicate the presence of liquid water, which may be indicative of the shedding of drops from melting hail often argues to be responsible for the development of K_{DP} columns (Rasmussen and Heymsfield, 1987; Hubbert et al., 1998). We believe this signature is not indicative of large hail as the ρ_{HV}, Z_{DR}, and K_{DP} values are typically much lower in such cases.

In order to further test this hypothesis, storms were classified as either “melting” or “non-melting”. In particular, storms were identified as melting if the HCA did not classify echo as HA within the lowest 2 km of a storm. Storms were considered non-melting if the HA class did reach to the lowest 1 km of a storm.

Figure 32 show the sensitivity of the hydrometeor frequency distribution for each hydrometeor class to changes in the MUCAPE environment for both storm types. Since there were more storms labeled as melting as opposed to non-melting, the melting plot resembles figure 30. Examining the non-melting storms, the larger frequencies of hail below the freezing level are in fact associated with higher MUCAPE, supporting the interpretation that the distributions for all cases represent the common occurrence of melting hail rather than large stones capable of reaching the surface. Higher frequencies of hail are also classified in general at any vertical level for higher MUCAPE regimes. As a result of higher frequencies of hail being classified for stronger MUCAPE environments, graupel frequencies must have been reduced to compensate. This is why within the 0-5 km relative altitude interval, relatively higher MUCAPE is associated with lower graupel frequencies, while relatively lower values of MUCAPE are associated with higher graupel frequencies.

Chapter 5: Summary and Conclusions

In this study, the authors leveraged polarimetric radar observations, a novel radar echo classification algorithm, a hydrometeor classification algorithm, a reanalysis dataset, an idealized model, and a polarimetric radar data simulator to determine the bulk microphysics of mesoscale convective systems in light of the environment in which they form, their lifecycle, geographic region, and seasonality.

5.1 Summary

Results have shown that midlatitude continental MCSs contain all forms of precipitations, including hail. Updraft and convective regions were characterized predominantly by liquid hydrometeors below the freezing level, with occasional rimed hydrometeors (graupel or hail) present below the freezing level especially during the developing and mature stages. The most notable feature was the "graupel nose" situated ∼0-6 km above the freezing level. As the lifecycle of the MCS progressed, the graupel signature began to decrease in magnitude and vertical extent owing to the decrease in environmental instability. Therefore, based on the HCA used in this study, graupel would be classified as the most dominant, or most likely, hydrometeor class ∼0-5 km above the freezing level. Since graupel is formed via accretion, the most dominant growth mechanism within the convective and updraft regions of MCSs is accretion.

At cloud top, non-rimed species were classified as the most dominant hydrometeor type in both convective and stratiform precipitation almost 90% of the time. During the development stage for convective regions, graupel particles, had appreciable classification frequencies. As the lifecycle of the MCSs progressed, the fractions aloft decreased.

If hail hydrometeor types were present within the convective regions of these systems, the maximum frequency occurred within the 0-5 km relative altitude range, albeit the frequencies were not as high as compared to graupel. Maximum hail frequencies were witnessed during the development stage of the system, thereafter decreasing as lifecycle progressed. Since graupel and hail are only differentiated based on size, which is proportional to Z_H, and given the small frequencies of hail that were classified, we expect that the hailstones in MCSs are rather small compared to other thunderstorm types like supercells. But, we argue the concentrations of hailstones are more numerous. The hailstones are also of small enough size so that a majority melt before reaching the surface. Figure 32 supports this claim.

Stratiform regions were characterized predominantly by liquid hydrometeors below the freezing level. Within the lowest 1 km of the freezing level, wet snow and graupel particles were also classified, although with relatively low frequencies ($<$ 15%). Above the freezing level, dry snow aggregates were the most dominant hydrometeor type within the 0-5 km relative altitude range. Graupel particles were allowed to be classified in the stratiform region and reached a maximum classification values just above the freezing level. Approaching cloud top altitudes, the dominant hydrometeor type became ice crystals of various orientations. The altitude in which the changeover of the dominant hydrometeor type between dry snow aggregates and ice crystals decreased as the lifecycle of the system progressed. This has implications as to which growth mechanisms are most dominant at specific vertical altitudes, specifically aggregation for dry snow vs. vapor deposition for ice crystals. The increase in various ice crystals in the dissipating stage may also be caused by the decrease in the total number of particles. As a result, less aggregation would occur as particles descend towards the freezing level.

The environment in which the system forms in has the greatest impact on rimed ice production. In more unstable environments, enhanced graupel and hail frequencies indicate that they are more readily classified as the dominant hydrometeor type compared to less unstable environments. Enhanced frequencies below and above the freezing level are seen, whereby reduced classification frequencies of liquid and non-rimed ice classes are exhibited.

5.2 Model vs. Observation Discussion

The model based and observational CFADs discussed are relatively similar to each other and are also similar to those of previous studies (e.g. Yuter and Houze, 1995). The Z_H CFAD for convective precipitation is oriented more in the vertical in the observational profiles compared to the simulated polarimetric Z_H CFADs with less spread most likely due to the increased number of observations from using multiple cases. The vertical offset of 1.5-2.0 km between the ρ_{HV} reduction and the freezing level as seen from the stratiform simulated radar CFADs from the model is also non-existent in the observations. Examining the single radar profiles reveals that the ρ_{HV} reduction is just offset the freezing level. This unphysical offset inevitably affected hydrometeor classification as was discussed in section 3.2. Z_{DR} observational CFADs were also greater than 0 dB above the freezing level unlike the simulated polarimetric Z_{DR} CFADs further highlighting the current limitation in the PRDS of distinguishing non-rimed species above the freezing level, especially for stratiform precipitation.

Vertical frequency distributions of dominant hydrometeor classes between the observations and model had their similarities and differences (Fig. 33). The main similarities within the convective region included the rimed-ice (predominately graupel) nose, liquid precipitation dominance below the freezing level, supercooled liquid hydrometeors present above the freezing level, and high non-rimed ice frequencies aloft. Model profiles for both the maximum q classification and when applying the updated P09 HCA to the simulated observations appeared qualitatively similar to the observational profiles. This indicates that the distribution of hydrometeors as represented in the model is performing quite well. However, it should be noted again that the "non-rimed ice" class is comprised of different species depending on the classification metric (i.e. see chapter 2.6 for details). While the distribution profiles may appear similar qualitatively, it may be so for the wrong reasons. Once shape information for cloud ice and cloud water is included in the PRDS, these (or similar) comparisons should be undertaken to determine the representation of such specie.

Concerning stratiform precipitation, there were some important differences between the model and observations. Namely, snow and related perturbations to the PRDS output were found as low as 1-2 km below the melting level, while there is no indication of significant amounts of snow at altitudes more than 1 km below the melting level in the observations. Because cloud ice and cloud water are not calculated in the PRDS, we also are unable to comment on the similarities and differences between the observed distribution of ice crystal and dry snow aggregates aloft, but this would be an interesting feature to examine further in future work. Thankfully, the observations and maximum q method classifications do compare well above the freezing level in the stratiform source region as snow aggregates were classified as the most dominant hydrometeor class in the 0-5 km relative altitude range, and ice is the most dominant class at higher altitudes. Both graupel profiles reached maxima at similar altitudes, albeit the model simulation vertical profiles of graupel reached higher altitudes compared to the observations, due to out strict < 2 km AFL classification threshold employed in the HCA.

5.3 Dynamical Implications

In this work, we highlighted an issue regarding the melting process in all of the microphysical parameterizations. This slowness would serve to impact the dynamics of the system through an increase in cold pool strength. A stronger cold pool would lead to faster system propagation (e.g. Weverberg et al., 2012). The slowness of the melting is hypothesized to be attributed to one, or both, of the following: 1.) the representation of the size of the hydrometeors as they fall through the environmental freezing level, or 2.) how melting is parameterized itself. Regarding the former, typically the median drop diameter in the grid volume is used to represent all particle sizes at a specific grid point. If hydrometeors are too large, melting rates will decrease, and frozen hydrometeors will extend to lower altitudes. This melting issue could possibly be only associated with bulk schemes. It would be interesting to compare the maximum q classification from a bulk scheme to a bin scheme to see if the melting issue is lessened.

Melting is generally parameterized in each scheme following an equation similar to that in Wisner et al. (1972) or Lin et al. (1983). Ice melts instantaneously to rain upon falling into warm air (i.e. T $>$ 0°C). However, the melting rate for snow, graupel, and hail is based on a heat balance between cooling associated with melting offset by heating from conduction and convection at the particle surface, sensible heating from the collected cloud and rainwater, and latent heat of condensation/evaporation of water to/from the particle surface (e.g. Wisner et al., 1972; Milbrandt and Yau, 2005b). If these processes are not in balance, then the melting rate will be smaller, thus enhancing cooling which will have a feedback on the dynamics of the system. We encourage future work testing the sensitivity of how melting is parameterized in parameterization schemes and how large of an effect this has on MCS development and evolution.

Along with the melting issue, we are able to hypothesize how these sytems may change dynamically from analyzing the dominant hydrometeor frequency profiles. For example, the MBY parameterization contains the largest amount of graupel amongst all schemes in the stratiform region. It also contains the largest vertical offset of the ρ_{HV} reduction from the 0°C altitude. However, observationally we saw similar quantitative values of graupel in the stratiform region yet the ρ_{HV} reduction was just offset from the 0°C altitude both the single radar and composite approaches.

Therefore, graupel alone is not responsible for the slow melting, but the enhanced graupel concentrations in the stratiform region may in fact be exacerbating the melting issue in this scheme. Examining the Z_{DR} CFAD for the MBY scheme, high values of Z_{DR} much greater than 1 dB are present, far larger than the observational CFADs. Therefore, the rain PSDs have too many large drops in the stratiform region (Putnam et al., 2016) which may have arisen from aggregates aloft that were too large.

The issue of melting was also seen in the convective region as the observed ρ_{HV} CFAD revealed more of a broad reduction extending to altitudes both above and below the freezing level. However in all of the convective model CFADs, the ρ_{HV} reduction occurs solely below the freezing level. Thus, it is likley that mixed-phase processes are inadequately represented in convective regions.

5.4 Future Work

The conclusions drawn from this study and future studies utilizing polarimetric radar observations can greatly improve our representation of microphysical processes in numerical models. Granted our knowledge of certain microphysical processes is still incomplete, we do have a general sense as to what processes lead to the formation of certain hydrometeor types and which processes occur in convective and stratiform regions. Since we now have a general understanding of the bulk hydrometeor distribution within continental midlatitude MCSs and its variation throughout the MCS lifecycle, we can better inform microphysics schemes as to where spatially and temporally certain processes should be modified to reproduce the observed characteristics.

The results from this study also show the utility of using a model and PRDS to improve hydrometeor classification, while also revealing some limitations with the model's microphysical processes themselves. We were able to show how the simulated polarimetric variables were able to better distinguish hail from the rain-hail mixture specie in P09. Although we are aware of the new hail classifications implemented into the original P09 HCA (see Ryzhkov et al., 2013; Ortega et al., 2016), the method we have employed is simpler and may in the future be used to justify or possibly change other membership functions of HCAs.

The results found in this study are mostly *qualitative* in nature though specific dominant hydrometeor frequency values were assigned. The *quantitative* information from this study could lay the initial framework for the development of more improved HCAs, like Baysian HCAs for example, or more advanced HCAs developed and trained using machine learning, but a considerable amount of additional work is required.

It's important to note that the conclusions drawn from a study like this are sensitive to the HCA chosen. For example, if this study were to be repeated with the NCAR particle identification (PID) algorithm (Vivekanandan et al., 1999), then the *quantitative* results might differ. As HCAs improve in the future, more quantitative attributes from studies of this kind may be used to improve microphysics schemes.

References

Barnes, H., and R. Houze, 2014: Precipitation hydrometeor type relative to the mesoscale airflow in mature oceanic deep convection of the Madden Julian oscillation. *J Geophys Res Atmospheres*, **119 (24)**, 13,990–14,014, doi: 10.1002/2014JD022241.

Barnes, H. C., and R. A. Houze, 2016: Comparison of observed and simulated spatial patterns of ice microphysical processes in tropical oceanic mesoscale convective systems. *J Geophys Res Atmospheres*, **121 (14)**, 8269–8296, doi: 10.1002/2016JD025074.

Bartels, D. L., and R. A. Maddox, 1991: Midlevel cyclonic vortices generated by mesoseale convective systems. *Mon Weather Rev*, **119 (1)**, 104–118, doi: 10.1175/1520-0493(1991)119<0104:MCVGBM>2.0.CO;2.

Biggerstaff, M., and R. Houze, 1991: Kinematic and precipitation structure of the 10-11 june 1985 squall line. *Monthly weather review*, **119 (12)**, 3034–3065, doi: 10.1175/1520-0493(1991)119<3034:KAPSOT>2.0.CO;2.

Bluestein, H. B., and M. H. Jain, 1985: Formation of mesoscale lines of precipitation: Severe squall lines in oklahoma during the spring. *J Atmos Sci*, **42 (16)**, 1711–1732, doi:10.1175/1520-0469(1985)042<1711:FOMLOP>2.0.CO;2.

Bluestein, H. B., G. T. Marx, and M. H. Jain, 1987: Formation of mesoscale lines of precipitation: Nonsevere squall lines in oklahoma during the spring. 2719–2727, doi:10.1175/1520-0493(1987)115<2719:FOMLOP>2.0.CO;2.

Bouniol, D., J. Delanoë, C. Duroure, A. Protat, V. Giraud, and G. Penide, 2010: Microphysical characterisation of west african MCS anvils. *Q J Roy Meteor Soc*, **136 (S1)**, 323–344, doi:10.1002/qj.557.

Brandes, E., J. Vivekanandan, J. Tuttle, and C. Kessinger, 1995: A study of thunderstorm microphysics with multiparameter radar and aircraft observations. *Mon Weather Rev*, **123 (11)**, 3129–3143, doi:10.1175/1520-0493(1995)123¡3129:ASOTMW¿2.0.CO;2.

Bringi, V. N., and V. Chandraseker, 2001: Polarimetric doppler weather radar: Principles and applications. 636.

Bryan, G. H., and H. Morrison, 2012: Sensitivity of a simulated squall line to horizontal resolution and parameterization of microphysics. **140 (1)**, 202–225, doi:10.1175/MWR-D-11-00046.1.

Caylor, I., and A. Illingworth, 1987: Radar observations and modelling of warm rain initiation. *Q J Roy Meteor Soc*, **113 (478)**, 1171–1191, doi: 10.1002/qj.49711347806.

Chen, S., and W. R. Cotton, 1988: The sensitivity of a simulated extratropical mesoscale convective system to longwave radiation and ice-phase microphysics. **45 (24)**, 3897–3910, doi:10.1175/1520-0469(1988)045¡3897:TSOASE¿2.0.CO;2.

Crum, T. D., and R. L. Alberty, 1993: The WSR-88D and the WSR-88D operational support facility. *B Am Meteorol Soc*, **74 (9)**, 1669–1687, doi:10.1175/1520-0477(1993)074<1669:TWATWO>2.0.CO;2.

Cunning, J. B., 1986: The Oklahoma-Kansas. preliminary regional experiment for STORM-Central. *B Am Meteorol Soc*, **67 (12)**, 1478–1486, doi:10.1175/1520-0477(1986)067¡1478:TOKPRE¿2.0.CO;2.

Davis, C., and Coauthors, 2004: The bow echo and MCV experiment: Observations and opportunities. *B Am Meteorol Soc*, **85 (8)**, 1075–1093, doi:10.1175/BAMS-85-8-1075.

Evaristo, R., G. Scialom, N. Viltard, and Y. Lemaître, 2010: Polarimetric signatures and hydrometeor classification of west african squall lines. *Q J Roy Meteor Soc*, **136 (S1)**, 272–288, doi:10.1002/qj.561.

Fabry, F., and I. Zawadzki, 1995: Long-Term radar observations of the melting layer of precipitation and their interpretation. *J Atmos Sci*, **52 (7)**, 838–851, doi:10.1175/1520-0469(1995)052<0838:LTROOT>2.0.CO;2.

Fovell, R. G., 2002: Upstream influence of numerically simulated squall-line storms. **128 (581)**, 893–912, doi:10.1256/0035900021643737.

Fovell, R. G., and Y. Ogura, 1988: Numerical simulation of a midlatitude squall line in two dimensions. **45 (24)**, 3846–3879, doi:10.1175/1520-0469(1988)045<3846:NSOAMS>2.0.CO;2.

Fritsch, J., R. Kane, and C. Chelius, 1986: The contribution of mesoscale convective weather systems to the Warm-Season precipitation in the united states. *J Clim Appl Meteorol*, **25 (10)**, 1333–1345, doi:10.1175/1520-0450(1986)025<1333:TCOMCW>2.0.CO;2.

Hall, M. P., J. W. Goddard, and S. M. Cherry, 1984: Identification of hydrometeors and other targets by dualpolarization radar. *Radio Sci*, **19 (1)**, 132–140, doi: 10.1029/RS019i001p00132.

Heymsfield, A. J., A. Bansemer, M. R. Poellot, and N. Wood, 2015: Observations of ice microphysics through the melting layer. *J Atmos Sci*, **72 (8)**, 2902–2928, doi:10.1175/JAS-D-14-0363.1.

Homeyer, C., 2014: Formation of the Enhanced-V infrared Cloud-Top feature from High-Resolution Three-Dimensional radar observations. *J Atmos Sci*, **71 (1)**, 332–348, doi:10.1175/JAS-D-13-079.1.

Homeyer, C., and M. Kumjian, 2015: Microphysical characteristics of overshooting convection from polarimetric radar observations. *J Atmos Sci*, **72 (2)**, 870–891, doi:10.1175/JAS-D-13-0388.1.

Houze, R., M. Rutledge, M. Biggerstaff, and B. Smull, 1989: Interpretation of doppler weather radar displays of midlatitude mesoscale convective systems. *Bull. Amer. Meteorol. Soc.*, doi:10.1175/1520-0477(1989)070<0608:IODWRD>2.0.CO;2.

Houze, R., B. Smull, and P. Dodge, 1990: Mesoscale organization of springtime rainstorms in oklahoma. *Mon Weather Rev*, **118 (3)**, 613–654, doi:10.1175/1520-0493(1990)118<0613:MOOSRI>2.0.CO;2.

Houze, R. A., 1989: Observed structure of mesoscale convective systems and implications for large scale heating. *Q J Roy Meteor Soc*, **115 (487)**, 425–461, doi:10.1002/qj.49711548702.

Houze, R. A., 1997: Stratiform precipitation in regions of convection: A meteorological paradox? **78 (10)**, 2179–2196, doi:10.1175/1520-0477(1997)078<2179:SPIROC>2.0.CO;2.

Houze, R. A., 2004: Mesoscale convective systems. *Rev Geophys*, **42 (4)**, doi: 10.1029/2004RG000150.

Houze, R. A., and D. D. Churchill, 1987: Mesoscale organization and cloud microphysics in a bay of bengal depression. **44 (14)**, 1845–1868, doi:10.1175/1520-0469(1987)044<1845:MOACMI>2.0.CO;2.

Hubbert, J., V. Bringi, L. Carey, and S. Bolen, 1998: CSU-CHILL polarimetric radar measurements from a severe hail storm in eastern colorado. *Journal of Applied* , **37 (8)**, 749–775, doi:10.1175/1520-0450(1998)037¡0749:CCPRMF¿2.0.CO;2.

Jameson, A., 1985: Deducing the microphysical character of precipitation from Multiple-Parameter radar polarization measurements. *J Clim Appl Meteorol*, **24 (10)**, 1037–1047.

Jensen, M., and Coauthors, 2015: The midlatitude continental convective clouds experiment (MC3E). *B Am Meteorol Soc*, doi:10.1175/BAMS-D-14-00228.1.

Johns, R. H., 1993: Meteorological conditions associated with bow echo development in convective storms. *Weather Forecast*, **8 (2)**, 294–299, doi:10.1175/1520-0434(1993)008¡0294:MCAWBE¿2.0.CO;2.

Jung, Y., M. Xue, and G. Zhang, 2010: Simulations of polarimetric radar signatures of a supercell storm using a Two-Moment bulk microphysics scheme. **49 (1)**, 146–163, doi:10.1175/2009JAMC2178.1.

Jung, Y., M. Xue, G. Zhang, and J. M. Straka, 2008a: Assimilation of simulated polarimetric radar data for a convective storm using the ensemble kalman filter. part II: impact of polarimetric data on storm analysis. *Mon Weather Rev*, **136 (6)**, 2246–2260, doi:10.1175/2007MWR2288.1.

Jung, Y., G. Zhang, and M. Xue, 2008b: Assimilation of simulated polarimetric radar data for a convective storm using the ensemble kalman filter. part i: Observation operators for reflectivity and polarimetric variables. **136 (6)**, 2228–2245, doi:10.1175/2007MWR2083.1.

Keenan, T., and R. Carbone, 1992: A preliminary morphology of precipitation systems in tropical northern australia. **118 (504)**, 283–326, doi:10.1002/qj.49711850406.

Khain, A., A. Pokrovsky, M. Pinsky, A. Seifert, and V. Phillips, 2004: Simulation of effects of atmospheric aerosols on deep turbulent convective clouds using a spectral microphysics Mixed-Phase cumulus cloud model. part i: Model description and possible applications. *J Atmos Sci*, **61 (24)**, 2963–2982, doi:10.1175/JAS-3350.1.

Kumjian, M., 2013a: Principles and applications of dual-polarization weather radar. part i: Description of the polarimetric radar variables. *J Operational Meteorology*, **1 (19)**, 226–242, doi:10.15191/nwajom.2013.0119.

Kumjian, M., 2013b: Principles and applications of dual-polarization weather radar. part II: warm- and cold-season applications. *J Operational Meteorology*, **1 (20)**, 243–264, doi:10.15191/nwajom.2013.0120.

Kumjian, M., 2013c: Principles and applications of dual-polarization weather radar. part III: artifacts. *J Operational Meteorology*, **1 (21)**, 265–274, doi:10.15191/nwajom.2013.0121.

Kumjian, M. R., and A. V. Ryzhkov, 2008: Polarimetric signatures in supercell thunderstorms. *J Appl Meteorol Clim*, **47 (7)**, 1940–1961, doi:10.1175/2007JAMC1874.1.

Leary, C. A., and R. A. Houze, 1979: Melting and evaporation of hydrometeors in precipitation from the anvil clouds of deep tropical convection. *Journal of the Atmospheric Sciences*, 669–679, doi:10.1175/1520-0469(1979)036<0669:MAEOHI>2.0.CO;2.

LeMone, M., E. Zipser, and S. Trier, 1998: The role of environmental shear and thermodynamic conditions in determining the structure and evolution of mesoscale convective systems during TOGA COARE. *J Atmos Sci*.

LeMone, M. A., and E. J. Zipser, 1980: Cumulonimbus vertical velocity events in GATE. part i: Diameter, intensity and mass flux. *J Atmos Sci*, **37 (11)**, 2444–2457, doi:10.1175/1520-0469(1980)037<2444:CVVEIG>2.0.CO;2.

Lin, Y., R. D. Farley, and H. D. Orville, 1983: Bulk parameterization of the snow field in a cloud model. 1065–1092, doi:10.1175/1520-0450(1983)022¡1065:BPOTSF¿2.0.CO;2.

Loney, M. L., D. S. Zrni, J. M. Straka, and A. V. Ryzhkov, 2002: Enhanced polarimetric radar signatures above the melting level in a supercell storm. *Journal of Applied* , **41 (12)**, 1179–1194, doi:10.1175/1520-0450(2002)041¡1179:EPRSAT¿2.0.CO;2.

Maddox, R. A., 1980: Meoscale convective complexes. **61 (11)**, 1374–1387, doi:10.1175/1520-0477(1980)061¡1374:MCC¿2.0.CO;2.

Maddox, R. A., 1983: Large-Scale meteorological conditions associated with midlatitude, mesoscale convective complexes. *Mon Weather Rev*, **111 (7)**, 1475–1493, doi:10.1175/1520-0493(1983)111¡1475:LSMCAW¿2.0.CO;2.

Mahoney, K. M., G. M. Lackmann, and M. D. Parker, 2009: The role of momentum transport in the motion of a Quasi-Idealized mesoscale convective system. *Mon Weather Rev*, **137 (10)**, 3316–3338, doi:10.1175/2009MWR2895.1.

Mansell, E., 2010: On sedimentation and advection in multimoment bulk microphysics. *Journal of the Atmospheric Sciences*, doi:10.1175/2010JAS3341.1.

Mansell, E. R., C. L. Ziegler, and E. C. Bruning, 2010: Simulated electrification of a small thunderstorm with Two-Moment bulk microphysics. **67 (1)**, 171–194, doi:10.1175/2009JAS2965.1.

McCumber, M., W. Tao, J. Simpson, R. Penc, and S. Soong, 1991: Comparison of Ice-Phase microphysical parameterization schemes using numerical simulations of tropical convection. *J Appl Meteorol*, **30 (7)**, 985–1004, doi:10.1175/1520-0450-30.7.985.

Mesinger, F., and Coauthors, 2006: North american regional reanalysis. **87 (3)**, 343–360, doi:10.1175/BAMS-87-3-343.

Milbrandt, J., and M. Yau, 2005a: A multimoment bulk microphysics parameterization. part i: Analysis of the role of the spectral shape parameter. **62 (9)**, 3051–3064, doi:10.1175/JAS3534.1.

Milbrandt, J., and M. Yau, 2005b: A multimoment bulk microphysics parameterization. part II: a proposed Three-Moment closure and scheme description. *J Atmos Sci*, **62 (9)**, 3065–3081, doi:10.1175/JAS3535.1.

Morrison, H., J. Curry, and M. Shupe, 2005: A new double-moment microphysics parameterization for application in cloud and climate models. part II: single-column modeling of arctic clouds. *Journal of the* .

Morrison, H., S. Tessendorf, and K. Ikeda, 2012: Sensitivity of a simulated midlatitude squall line to parameterization of raindrop breakup. *Monthly Weather* , **140 (8)**, 2437–2460, doi:10.1175/MWR-D-11-00283.1.

Morrison, H., G. Thompson, and V. Tatarskii, 2009: Impact of cloud microphysics on the development of trailing stratiform precipitation in a simulated squall line: Comparison of One- and Two-Moment schemes. **137 (3)**, 991–1007, doi:10.1175/2008MWR2556.1.

Ortega, K. L., J. M. Krause, and A. V. Ryzhkov, 2016: Polarimetric radar characteristics of melting hail. part III: validation of the algorithm for hail size discrimination. *J Appl Meteorol Clim*, **55 (4)**, 829–848, doi:10.1175/JAMC-D-15-0203.1.

Pandya, R. E., and D. R. Durran, 1996: The influence of convectively generated thermal forcing on the mesoscale circulation around squall lines. **53 (20)**, 2924–2951, doi:10.1175/1520-0469(1996)053<2924:TIOCGT>2.0.CO;2.

Park, H., A. Ryzhkov, D. Zrni, and K. Kim, 2009: The hydrometeor classification algorithm for the polarimetric WSR-88D: description and application to an MCS. *Weather Forecast*, **24 (3)**, 730–748, doi:10.1175/2008WAF2222205.1.

Parker, M., and R. Johnson, 2000: Organizational modes of midlatitude mesoscale convective systems. *Mon Weather Rev*, **128 (10)**, 3413–3436, doi:10.1175/1520-0493(2001)129<3413:OMOMMC>2.0.CO;2.

Putnam, B., M. Xue, Y. Jung, G. Zhang, and F. Kong, 2016: Simulation of polarimetric radar variables from 2013 CAPS spring experiment storm scale ensemble forecasts and evaluation of microphysics schemes. *Mon Weather Rev*, doi:10.1175/MWR-D-15-0415.1.

Rasmussen, R. M., and A. J. Heymsfield, 1987: Melting and shedding of graupel and hail. part III: investigation of the role of shed drops as hail embryos in the 1 august CCOPE severe storm. *J Atmos Sci*, **44 (19)**, 2783–2803, doi:10.1175/1520-0469(1987)044¡2783:MASOGA¿2.0.CO;2.

Rotunno, R., J. B. Klemp, and M. L. Weisman, 1988: A theory for strong, Long-Lived squall lines. **45 (3)**, 463–485, doi:10.1175/1520-0469(1988)045<0463:ATFSLL>2.0.CO;2.

Rowe, A., and R. Houze, 2014: Microphysical characteristics of MJO convection over the Indian Ocean during DYNAMO. *J Geophys Res Atmospheres*, **119 (5)**, 2543–2554, doi:10.1002/2013JD020799.

Rutledge, S. A., and R. A. Houze, 1987: A diagnostic modelling study of the trailing stratiform region of a midlatitude squall line. **44 (18)**, 2640–2656, doi:10.1175/1520-0469(1987)044<2640:ADMSOT>2.0.CO;2.

Ryzhkov, A. V., 2007: The impact of beam broadening on the quality of radar polarimetric data. *Journal of Atmospheric and Oceanic Technology*, **24 (5)**, 729–744, doi:10.1175/JTECH2003.1.

Ryzhkov, A. V., S. E. Giangrande, V. M. Melnikov, and T. J. Schuur, 2005: Calibration issues of Dual-Polarization radar measurements. **22 (8)**, 1138–1155, doi:10.1175/JTECH1772.1.

Ryzhkov, A. V., M. R. Kumjian, S. M. Ganson, and P. Zhang, 2013: Polarimetric radar characteristics of melting hail. part II: practical implications. *J Appl Meteorol Clim*, **52 (12)**, 2871–2886, doi:10.1175/JAMC-D-13-074.1.

Schmidt, J. M., and W. R. Cotton, 1990: Interactions between upper and lower tropospheric gravity waves on squall line structure and maintenance. *J Atmos Sci*, **47 (10)**, 1205–1222, doi:10.1175/1520-0469(1990)047<1205:IBUALT>2.0.CO;2.

Seliga, T., and V. Bringi, 1976: Potential use of radar differential reflectivity measurements at orthogonal polarizations for measuring precipitation. *J Appl Meteorol*, **15 (1)**, 69–76, doi:10.1175/1520-0450(1976)015<0069:PUORDR>2.0.CO;2.

Seliga, T., and V. Bringi, 1978: Differential reflectivity and differential phase shift: Applications in radar meteorology. *Radio Sci*, **13 (2)**, 271–275, doi:10.1029/RS013i002p00271.

Skamarock, W., J. Klemp, W. Skamarock, and J. Klemp, 2008: A time-split nonhydrostatic atmospheric model for weather research and forecasting applications. doi:10.1016/j.jcp.2007.01.037.

Smull, B. F., and R. A. Houze, 1985: A midlatitude squall line with a trailing region of stratiform rain: Radar and satellite observations. *Mon Weather Rev*, **113 (1)**, 117–133, doi:10.1175/1520-0493(1985)113<0117:AMSLWA>2.0.CO;2.

Smull, B. F., and R. A. Houze, 1987: Rear inflow in squall lines with trailing stratiform precipitation. *Mon Weather Rev*, **115 (12)**, 2869–2889, doi:10.1175/1520-0493(1987)115<2869:RIISLW>2.0.CO;2.

Starzec, M., C. R. Homeyer, and G. L. Mullendore, 2017: Storm labeling in 3 dimensions (SL3D): a volumetric radar echo and Dual-Polarization updraft classification algorithm. *Mon Weather Rev*, doi:10.1175/MWR-D-16-0089.1.

Steiner, M., R. A. Houze, and S. E. Yuter, 1995: Climatological characterization of Three-Dimensional storm structure from operational radar and rain gauge data. *J Appl Meteorol*, **34 (9)**, 1978–2007, doi:10.1175/1520-0450(1995)034¡1978:CCOTDS¿2.0.CO;2.

Stensrud, D. J., 1996: Importance of Low-Level jets to climate: A review. *J Climate*, **9 (8)**, 1698–1711, doi:10.1175/1520-0442(1996)009¡1698:IOLLJT¿2.0.CO;2.

Straka, J., and D. Zrnic, 2000: Bulk hydrometeor classification and quantification using polarimetric radar data: Synthesis of relations. *Journal of Applied Meteorology*, doi:10.1175/1520-0450(2000)039<1341:BHCAQU>2.0.CO;2.

Thompson, G., P. Field, R. Rasmussen, and W. Hall, 2008: Explicit forecasts of winter precipitation using an improved bulk microphysics scheme. part II: implementation of a new snow parameterization. doi:10.1175/2008MWR2387.1.

Vivekanandan, J., W. Adams, and V. Bringi, 1991: Rigorous approach to polarimetric radar modeling of hydrometeor orientation distributions. **30 (8)**, 1053–1063, doi:10.1175/1520-0450(1991)030¡1053:RATPRM¿2.0.CO;2.

Vivekanandan, J., S. Ellis, R. Oye, D. Zrnic, A. Ryzhkov, and J. Straka, 1999: Cloud microphysics retrieval using s-band Dual-Polarization radar measurements. *B Am Meteorol Soc*, **80 (3)**, 381–388, doi:10.1175/1520-0477(1999)080<0381:CMRUSB>2.0.CO;2.

Weinheimer, A. J., and A. A. Few, 1987: The electric field alignment of ice particles in thunderstorms. *J Geophys Res Atmospheres 1984 2012*, **92 (D12)**, 14 833–14 844, doi:10.1029/JD092iD12p14833.

Weisman, M., and J. Klemp, 1982a: The dependence of numerically simulated convective storms on vertical wind shear and buoyancy. *Monthly Weather Review*, **110 (6)**, 504–520, doi:10.1175/1520-0493(1982)110<0504:TDONSC>2.0.CO;2.

Weisman, M., and J. Klemp, 1982b: The dependence of numerically simulated convective storms on vertical wind shear and buoyancy. *Monthly Weather Review*, **110 (6)**, 504–520, doi:10.1175/1520-0493(1982)110<0504:TDONSC>2.0.CO;2.

Weisman, M. L., 1993: The genesis of severe, Long-Lived bow echoes. *J Atmos Sci*, **50 (4)**, 645–670, doi:10.1175/1520-0469(1993)050¡0645:TGOSLL¿2.0.CO;2.

Weisman, M. L., 2001: Bow echoes: A tribute to t. t. fujita. *B Am Meteorol Soc*, **82 (1)**, 97–116, doi:10.1175/1520-0477(2001)082¡0097:BEATTT¿2.3.CO;2.

Weisman, M. L., J. B. Klemp, and R. Rotunno, 1988: Structure and evolution of numerically simulated squall lines. **45 (14)**, 1990–2013, doi:10.1175/1520-0469(1988)045<1990:SAEONS>2.0.CO;2.

Weverberg, K., A. M. Vogelmann, H. Morrison, and J. A. Milbrandt, 2012: Sensitivity of idealized Squall-Line simulations to the level of complexity used in Two-Moment bulk microphysics schemes. *Mon Weather Rev*, **140 (6)**, 1883–1907, doi:10.1175/MWR-D-11-00120.1.

Weverberg, V. K., and Coauthors, 2013: The role of cloud microphysics parameterization in the simulation of mesoscale convective system clouds and precipitation in the tropical western pacific. *J Atmos Sci*, **70 (4)**, 1104–1128, doi:10.1175/JAS-D-12-0104.1.

Wisner, C., H. Orville, and C. Myers, 1972: A numerical model of a hail-bearing cloud. *Journal of the Atmospheric* .

Yuter, S. E., and R. A. Houze, 1995: Three-Dimensional kinematic and microphysical evolution of florida cumulonimbus. part II: frequency distributions of vertical velocity, reflectivity, and differential reflectivity. 1941–1963, doi:10.1175/1520-0493(1995)123<1941:TDKAME>2.0.CO;2.

Zhang, D., and M. J. Fritsch, 1987: Numerical simulation of the meso-β scale structure and evolution of the 1977 johnstown flood. part II: inertially stable Warm-Core vortex and the mesoscale convective complex. *J Atmos Sci*, **44 (18)**, 2593–2612, doi:10.1175/1520-0469(1987)044<2593:NSOTMS>2.0.CO;2.

Zhang, G., 2016: Weather radar polarimetry. 304.

Zhang, J., S. Wang, and B. Clarke, 2004: Wsr-88d reflectivity quality control using horizontal and vertical reflectivity structure. *11th Conf. on Aviation, Range, and Aerospace Meteorology*, URL `[Available online at https://ams.confex.com/ams/pdfpapers/81858.pdf]`.

Zipser, E., and M. LeMone, 1980: Cumulonimbus vertical velocity events in GATE. part II: synthesis and model core structure. *J Atmos Sci*, **37 (11)**, 2458–2469, doi:10.1175/1520-0469(1980)037<2458:CVVEIG>2.0.CO;2.

Zipser, E. J., 1969: The role of organized unsaturated convective downdrafts in the structure and rapid decay of an equatorial disturbance. **8 (5)**, 799–814, doi:10.1175/1520-0450(1969)008<0799:TROOUC>2.0.CO;2.

Zipser, E. J., 1977: Mesoscale and convective scale downdrafts as distinct components of squall-line structure. **105 (12)**, 1568–1589, doi:10.1175/1520-0493(1977)105<1568:MACDAD>2.0.CO;2.

Zrnic, D., N. Balakrishnan, C. Ziegler, V. Bringi, K. Aydin, and T. Matejka, 1993: Polarimetric signatures in the stratiform region of a mesoscale convective system. *J Appl Meteorol*, **32 (4)**, 678–693, doi:10.1175/1520-0450(1993)032¡0678:PSITSR¿2.0.CO;2.

Appendix: Figures & Tables

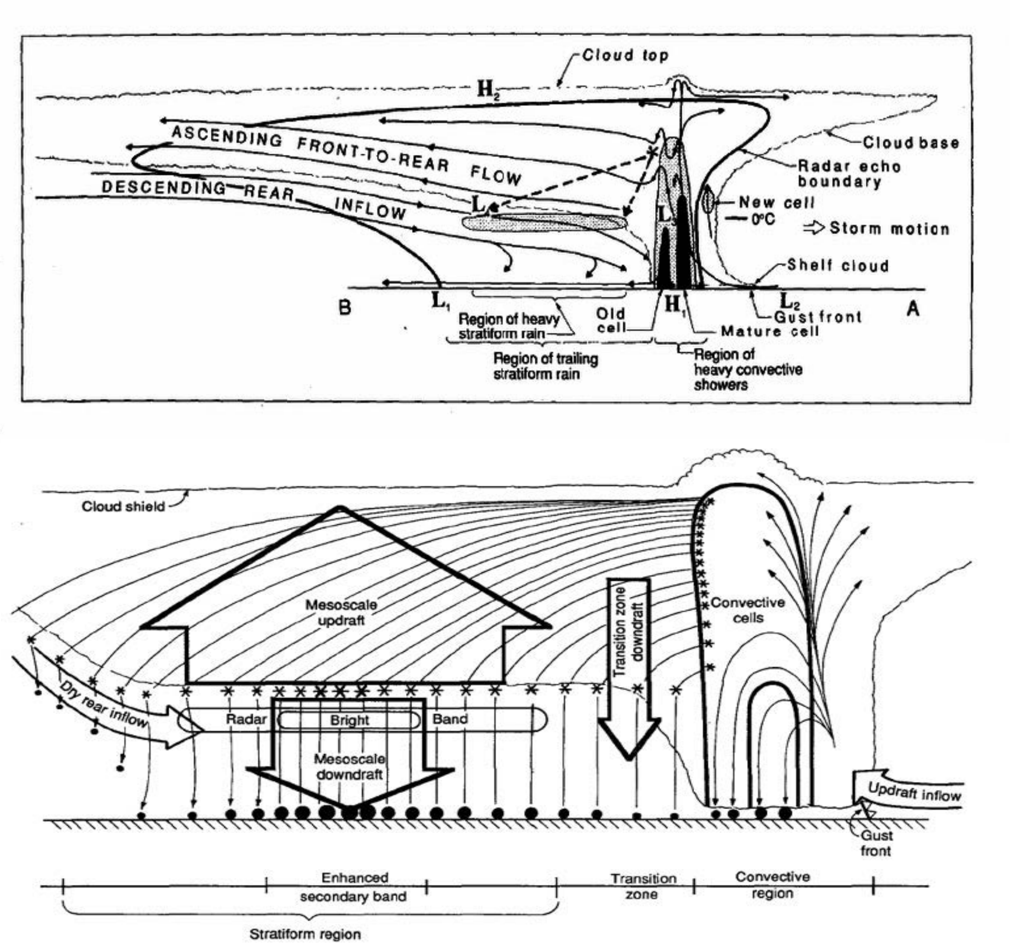

Figure 1: Schematics showing characteristic kinematic wind profiles, different modes of precipitation, and hydrometeor particle trajectories within the traditional LLTS MCS. Top: (Houze et al., 1989); Bottom: (Biggerstaff and Houze, 1991)

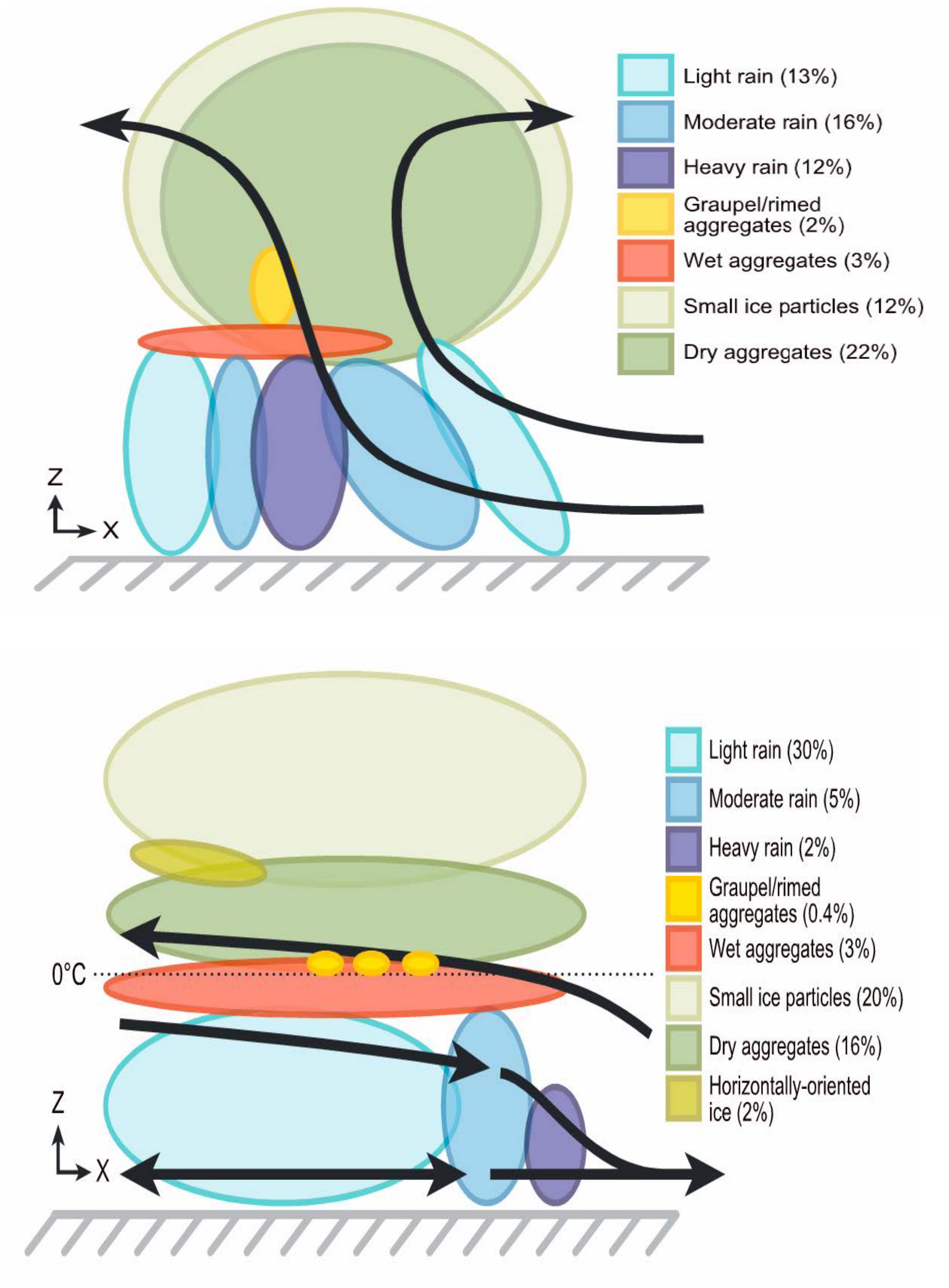

Figure 2: Barnes and Houze (2014) conceptual model for mature tropical MCSs associated with the MJO. Top panel represents the convective region whereas the bottom panel represents the stratiform region. See their figures 8 and 11 for more information.

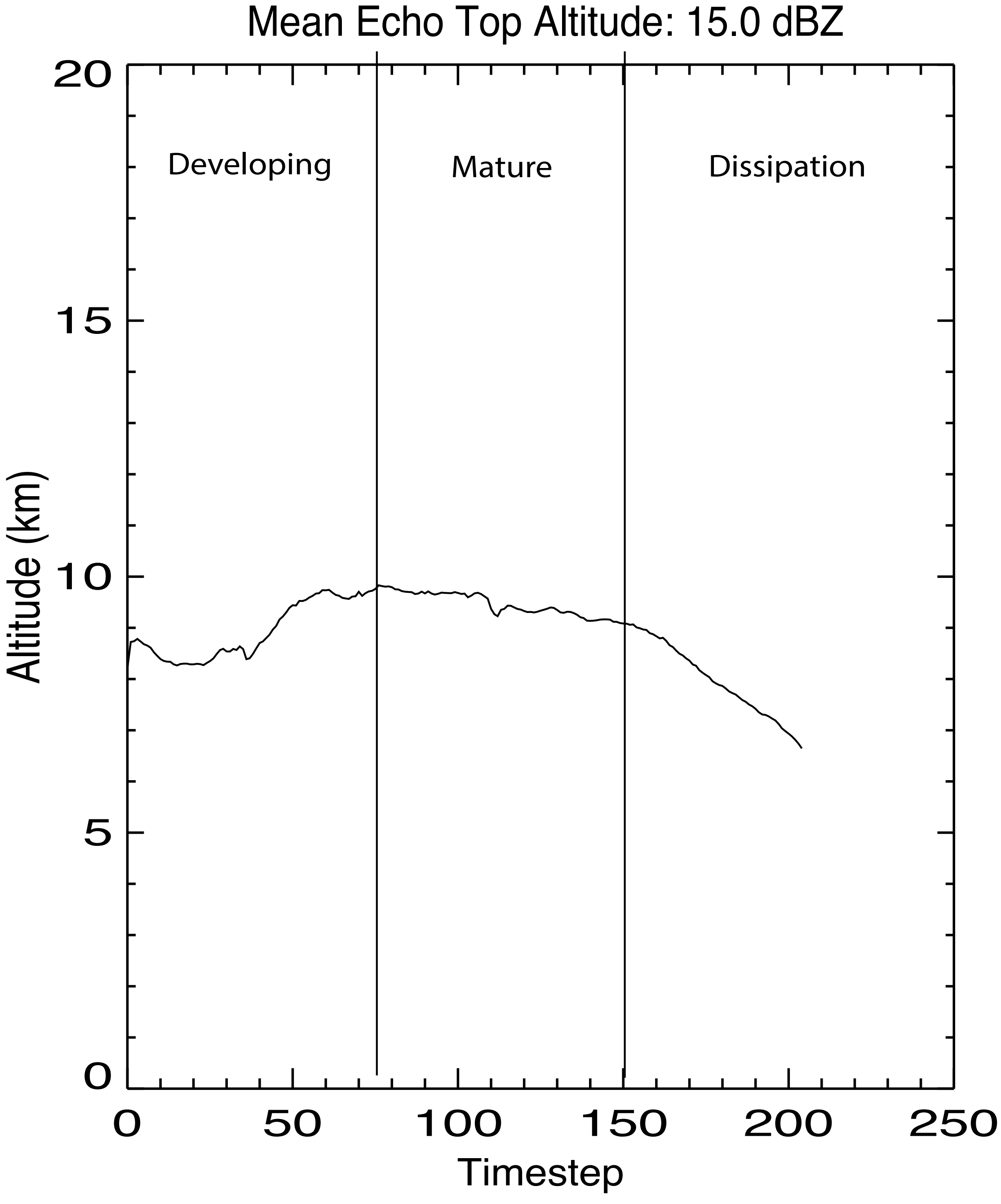

Figure 3: Mean (left) and Median (right) Z_H convective echo top altitude time series for 2014 June 16-17. Vertical lines denote the separation time index for a lifecycle stage.

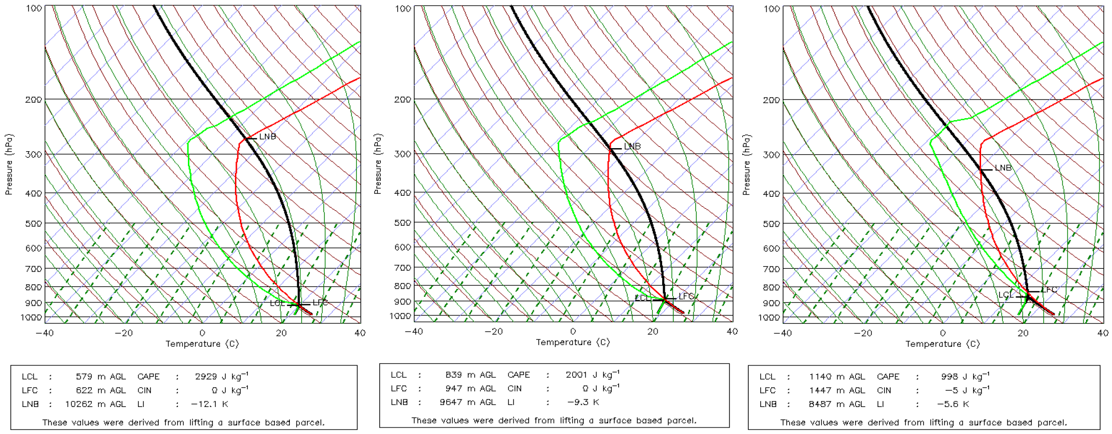

Figure 4: WRF soundings used for deriving environment sensitivities as pertubred from Weisman and Klemp (1982a). Red line indicates temperature profile, green line indicates dewpoint profile, and black line represents the most unstable parcel profile. Sounding intensity (measured by MUCAPE) decreases as viewed from left to right.

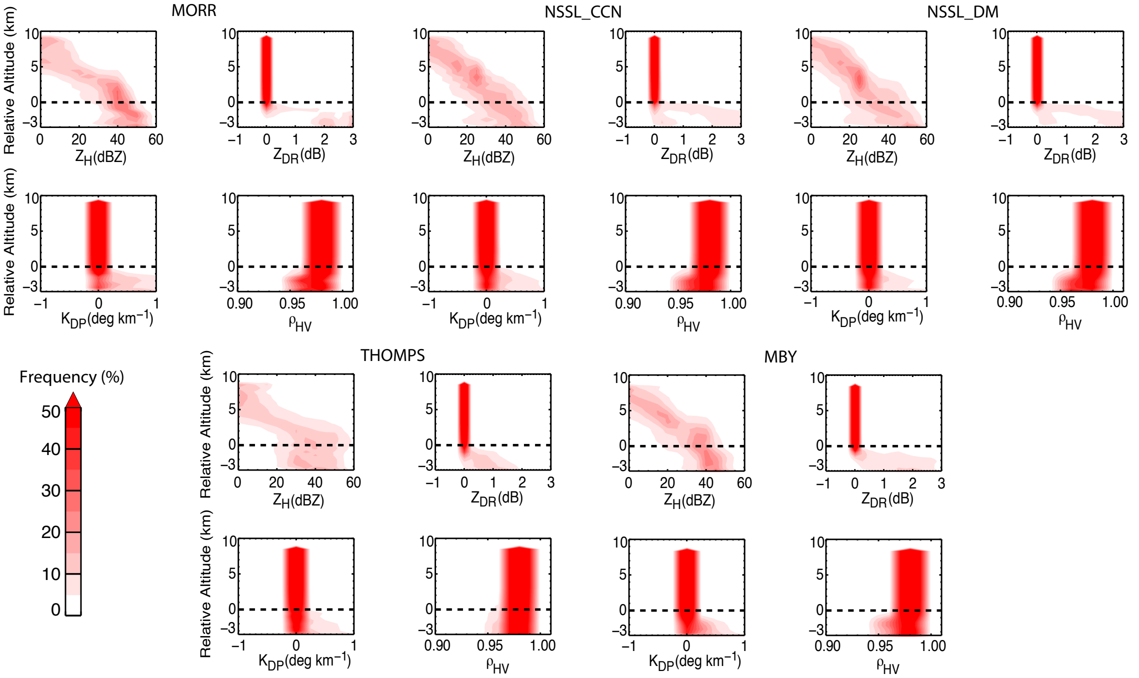

Figure 5: Simulated polarimetric radar variable CFADs for each microphysics scheme for the convective source region of the MCS. Colored contours represent the frequency (%). Dashed black line represents the 0 km relative altitude bin. Profiles are binned relative to the environmental freezing level altitude (i.e. 0°C isotherm altitude). The same ordering of microphysics schemes will be used in subsequent plots.

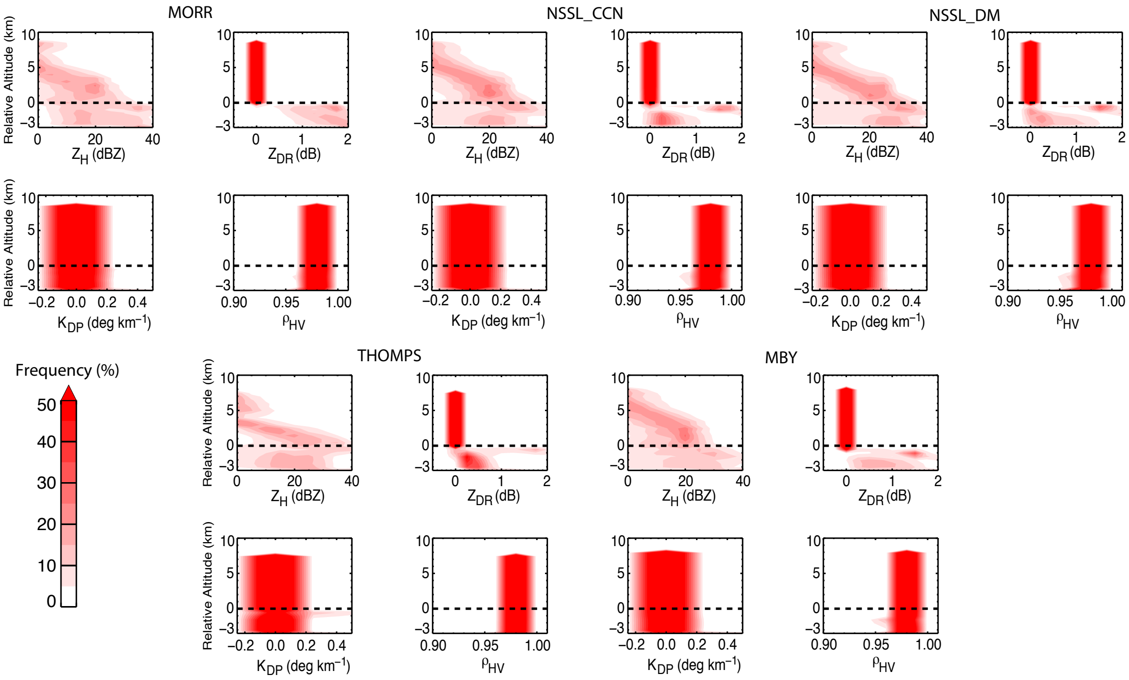

Figure 6: Same as figure 5 except for the stratiform source region of the MCS.

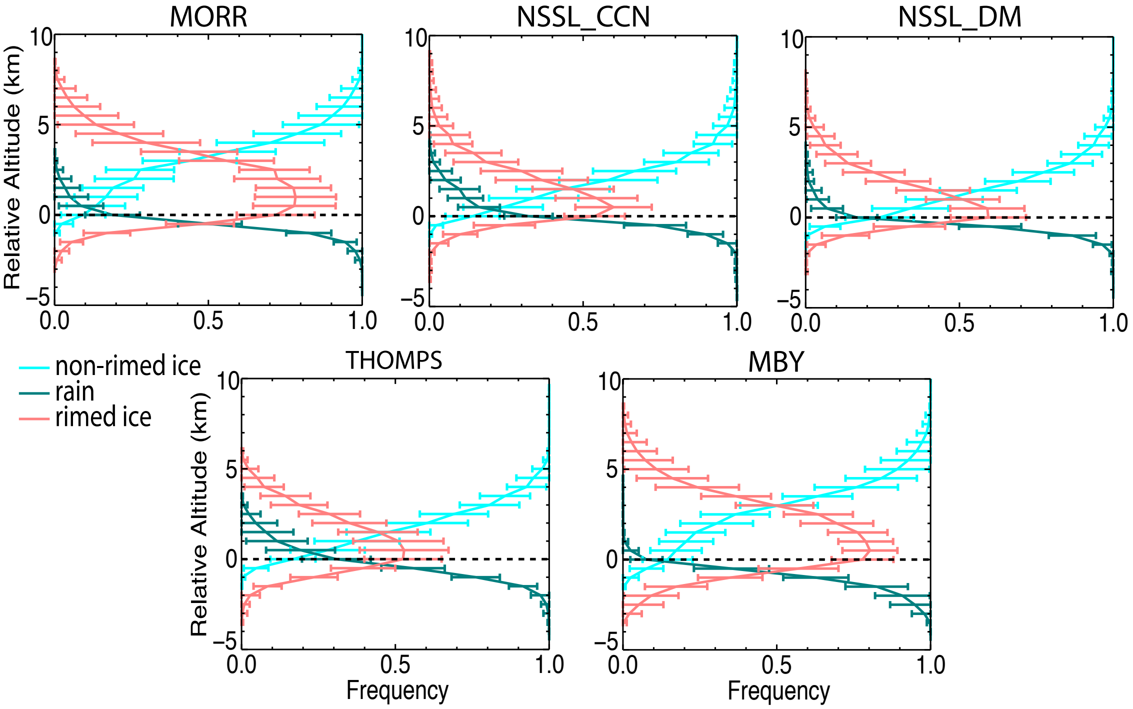

Figure 7: Mean convective source region vertical hydrometeor frequency distribution profiles for all microphysics schemes using the maximum q approach. Profiles are binned relative to the environmental freezing level altitude. Dashed black line indicates the 0 km relative bin. Hashes attached to each vertical profile represent +/- 1σ values. Each color represents a hydrometeor class denoted by the legend on the left. Frequencies can be converted to % by multiplying any value by 100%.

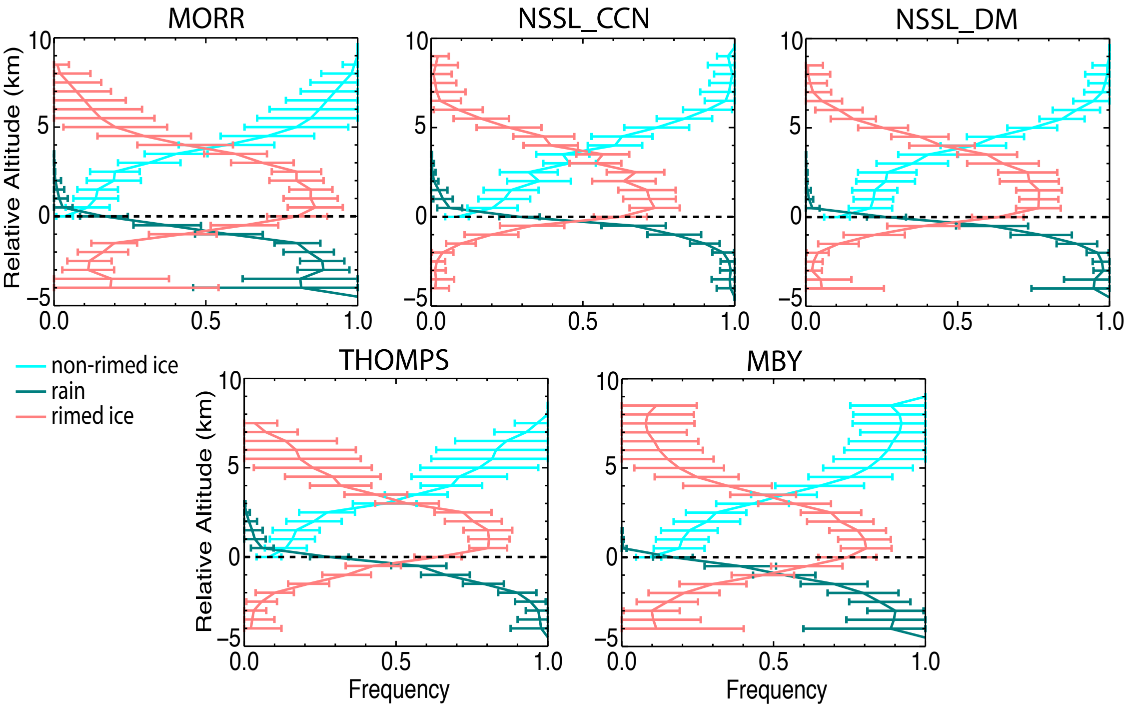

Figure 8: Similar to figure 7 except hydrometeor frequencies are determined by the HCA applied to the simulated polarimetric radar data.

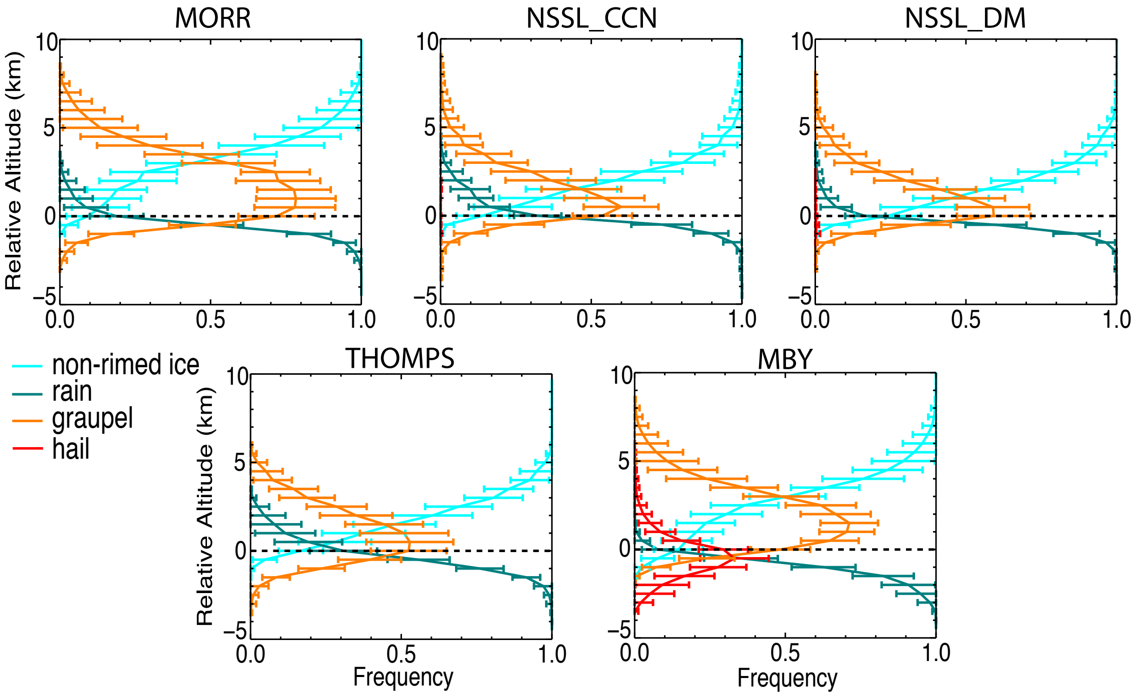

Figure 9: Same as figure 7 except the rimed ice category is separated into graupel and hail classes.

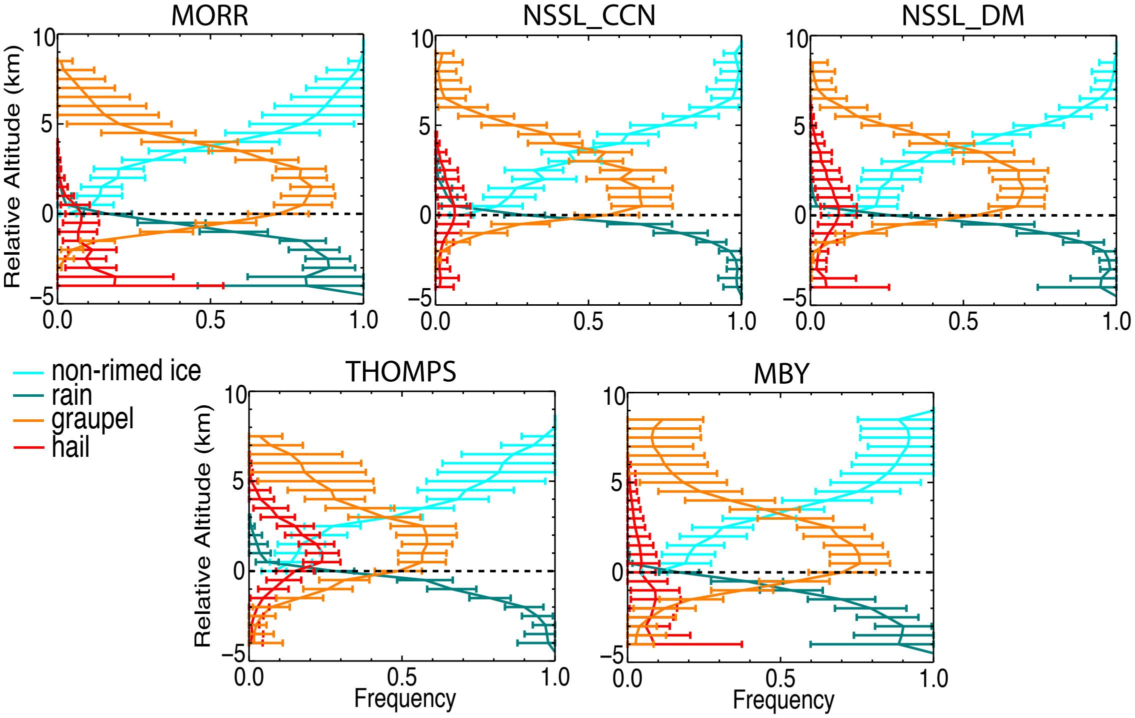

Figure 10: Same as figure 8 except the rimed ice category is separated into graupel and hail classes.

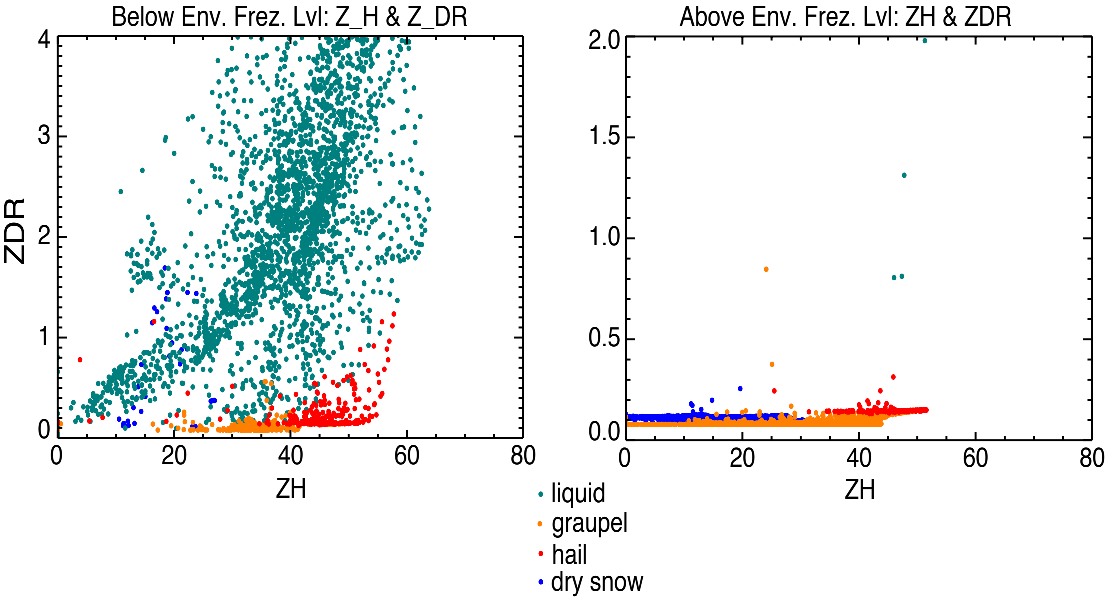

Figure 11: An example Z_H (x-axis) and Z_{DR} (y-axis) scatterplot for the convective source region of the MBY microphysic scheme. Each dot represents the simulated polarimetric radar data values corresponding to the maximum q HCA classification at a given grid point. Left panel features grid points below the environmental freezing level whereas the right figure represents grid points above the environmental freezing level. The legend is given in the bottom center of the figure.

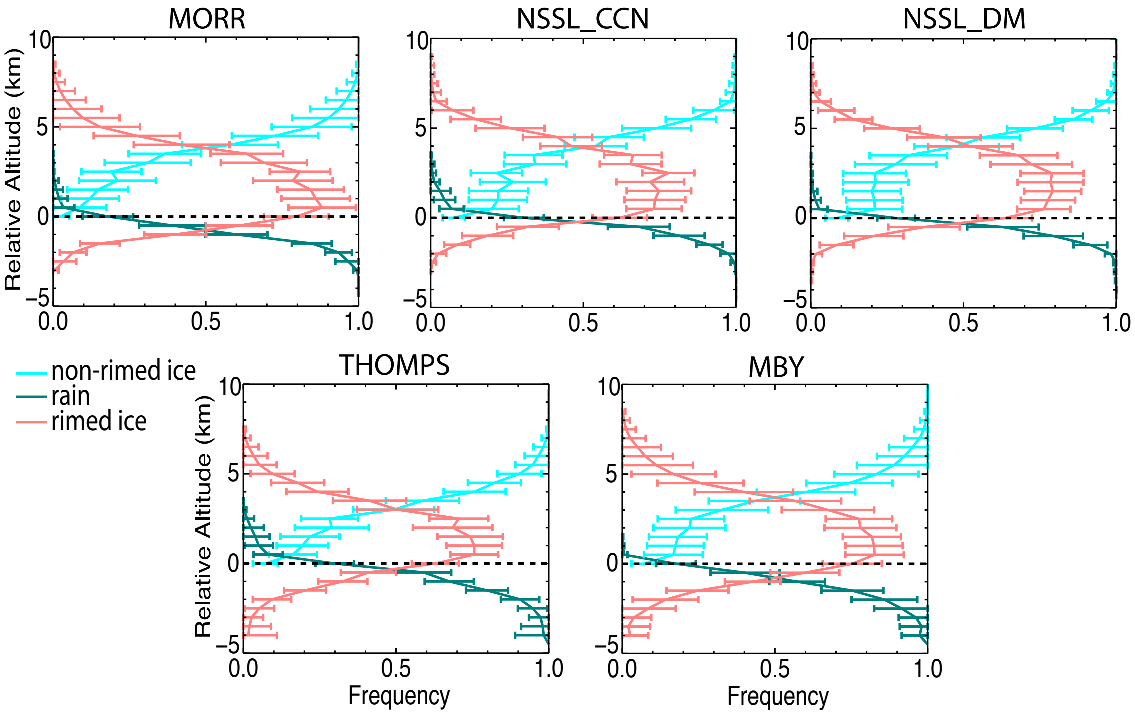

Figure 12: Similar to figure 8 except accounting for new HCA modifications as discussed in the text.

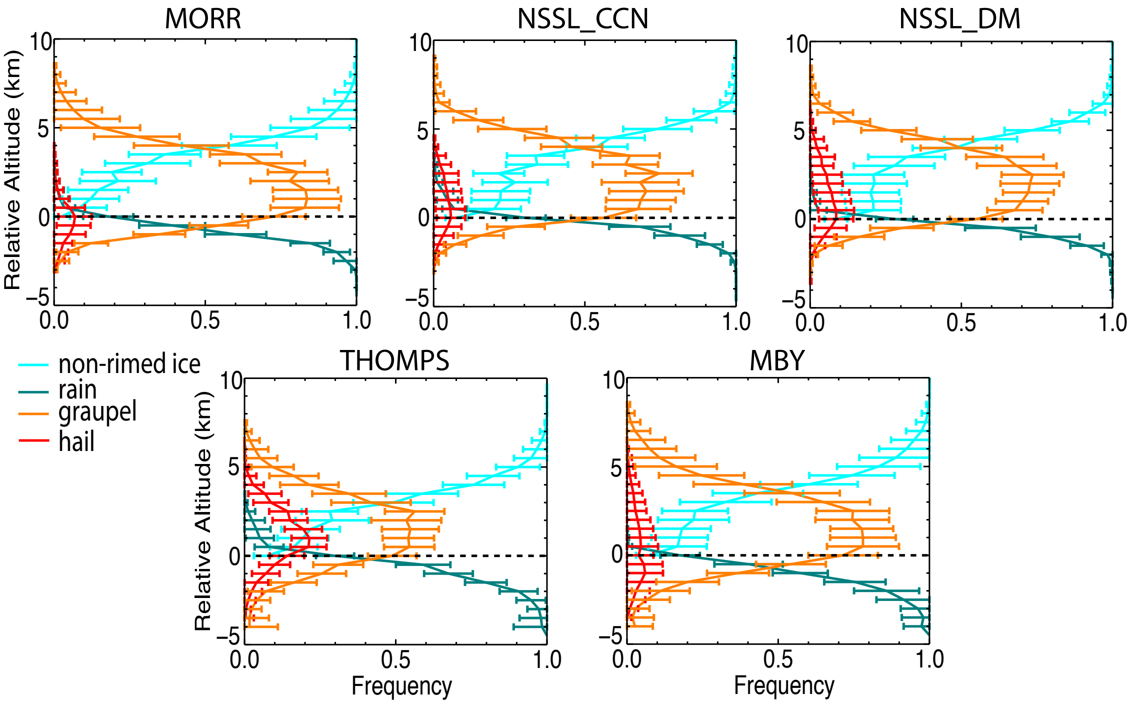

Figure 13: Similar to figure 12 except rimed ice category is separated into graupel and hail classes.

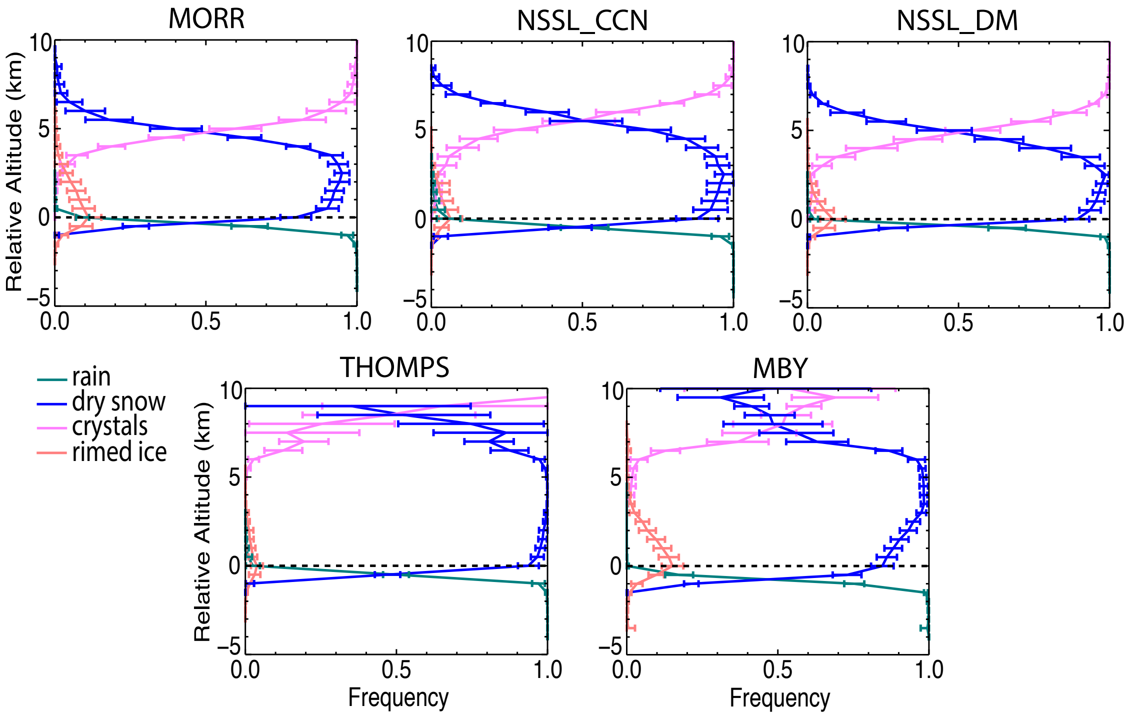

Figure 14: Similar to figure 7 except the stratiform source region is analyzed.

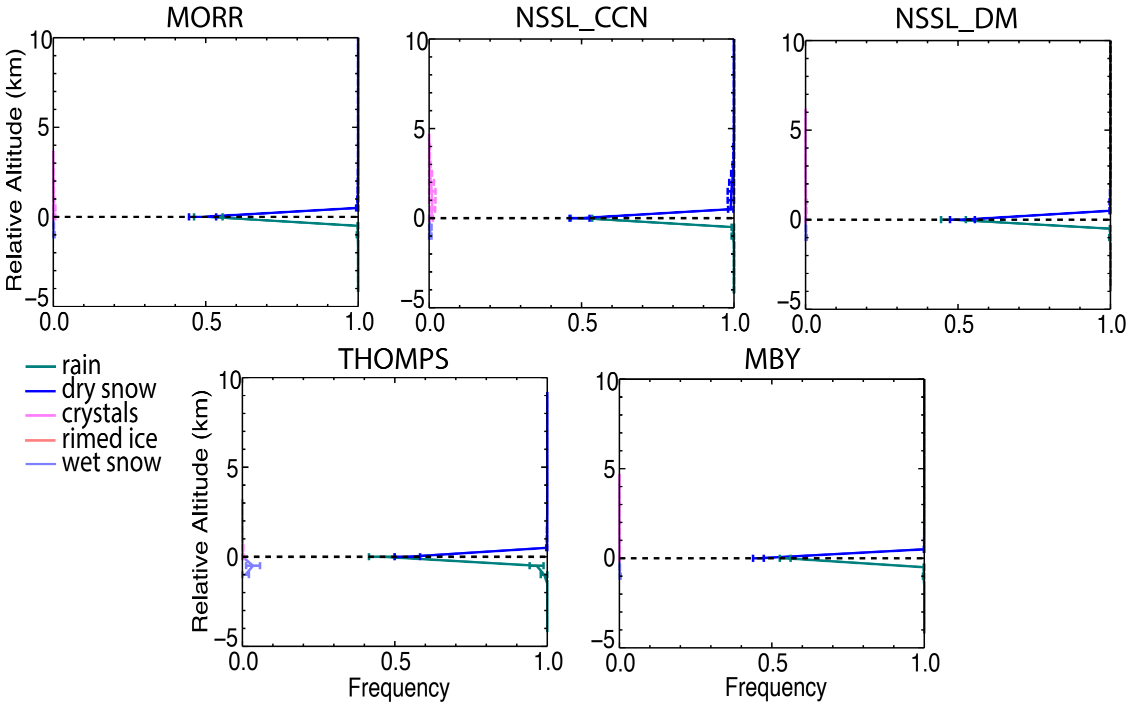

Figure 15: Similar to figure 8 except the stratiform source region is analyzed.

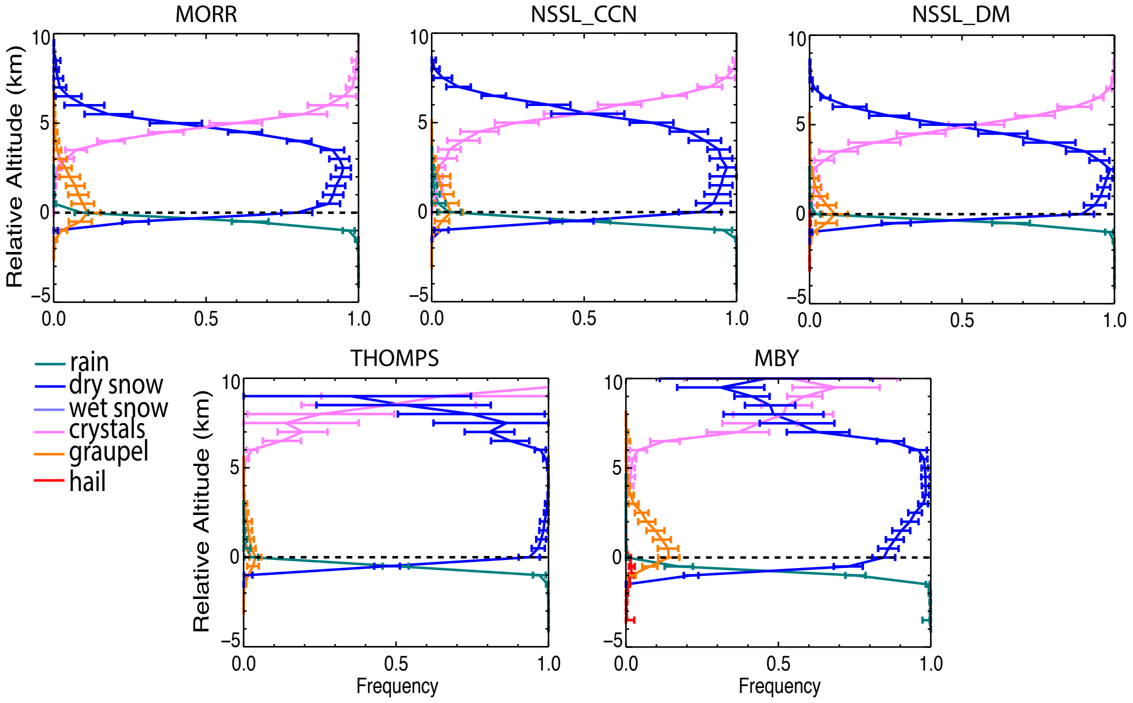

Figure 16: Similar to figure 9 except the stratiform source region is analyzed.

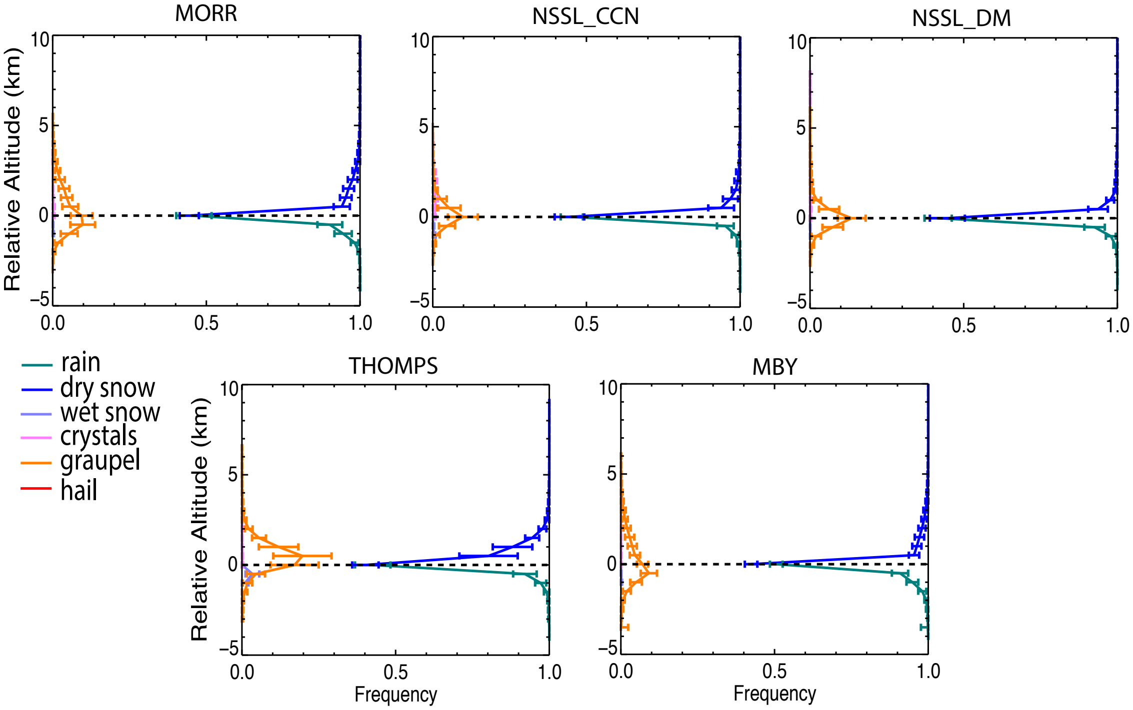

Figure 17: Similar to figure 15 except the stratiform source region is analyzed.

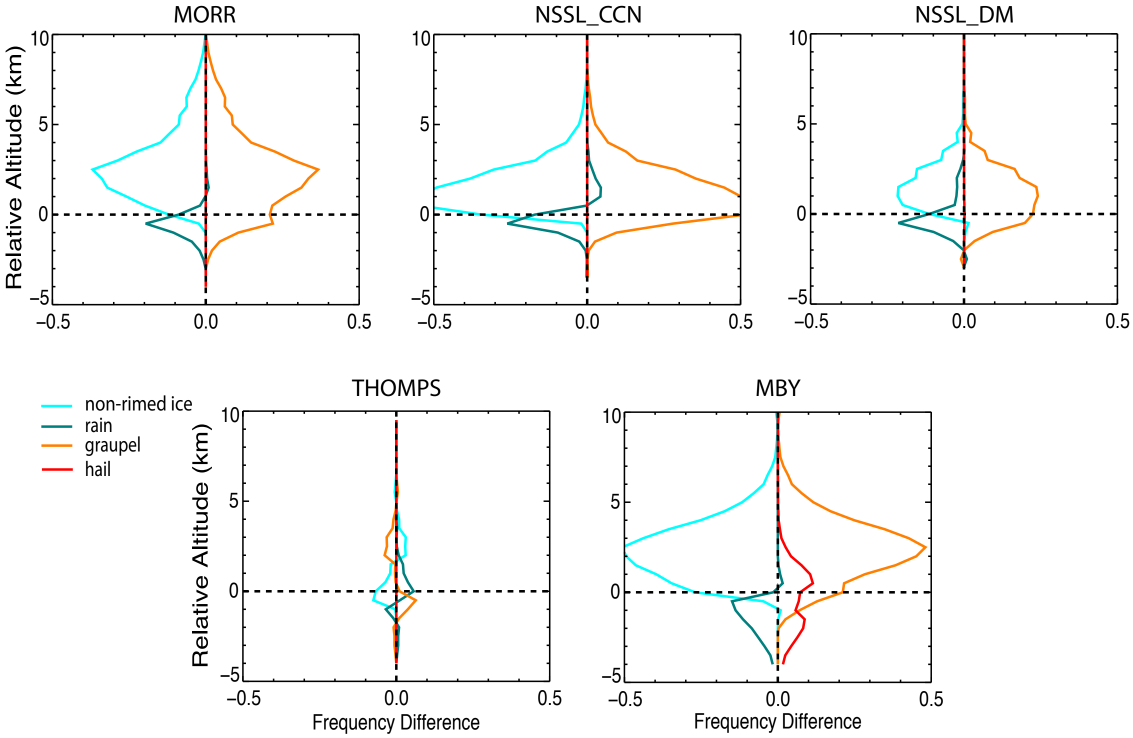

Figure 18: Convective source region hydrometeor distribution high-low MUCAPE regime differences as classified by the maximum q HCA for each microphysics scheme. A positive difference indicates mean hydrometeor frequencies were larger for more unstable environments. Colors are similar to previous figures. Dashed lines indicate 0.0 km relative altitude along with 0.0 difference location.

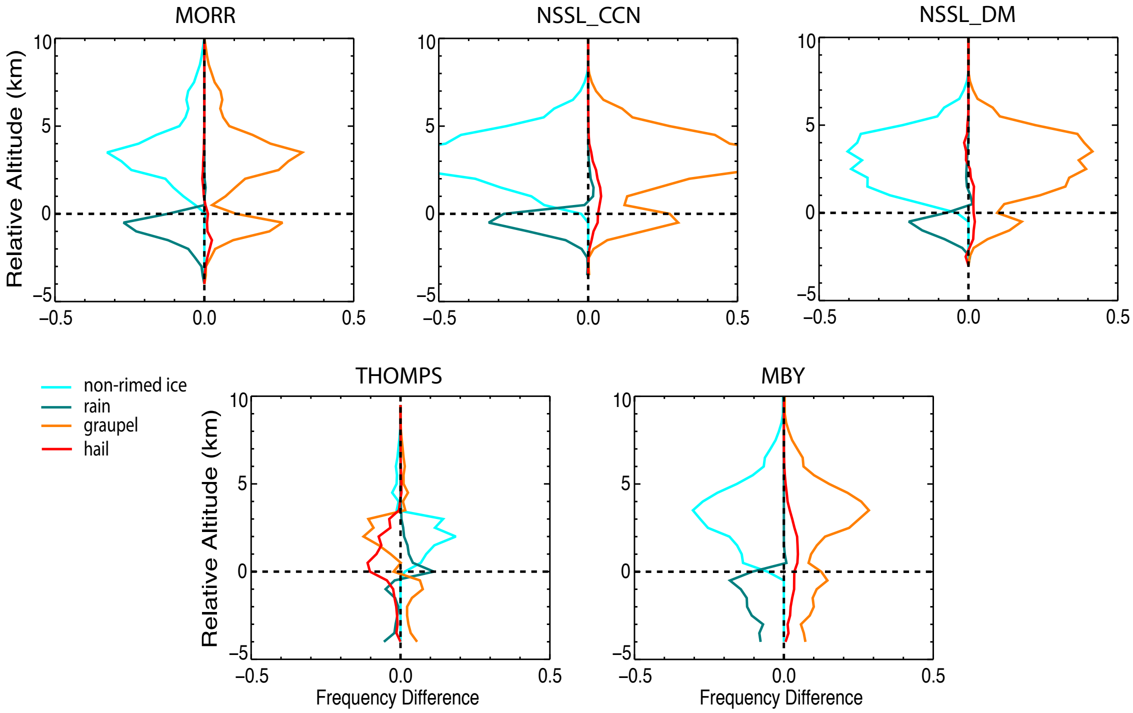

Figure 19: Similar to figure 18 except vertical profiles are classified by the simulated polarimetric radar variables.

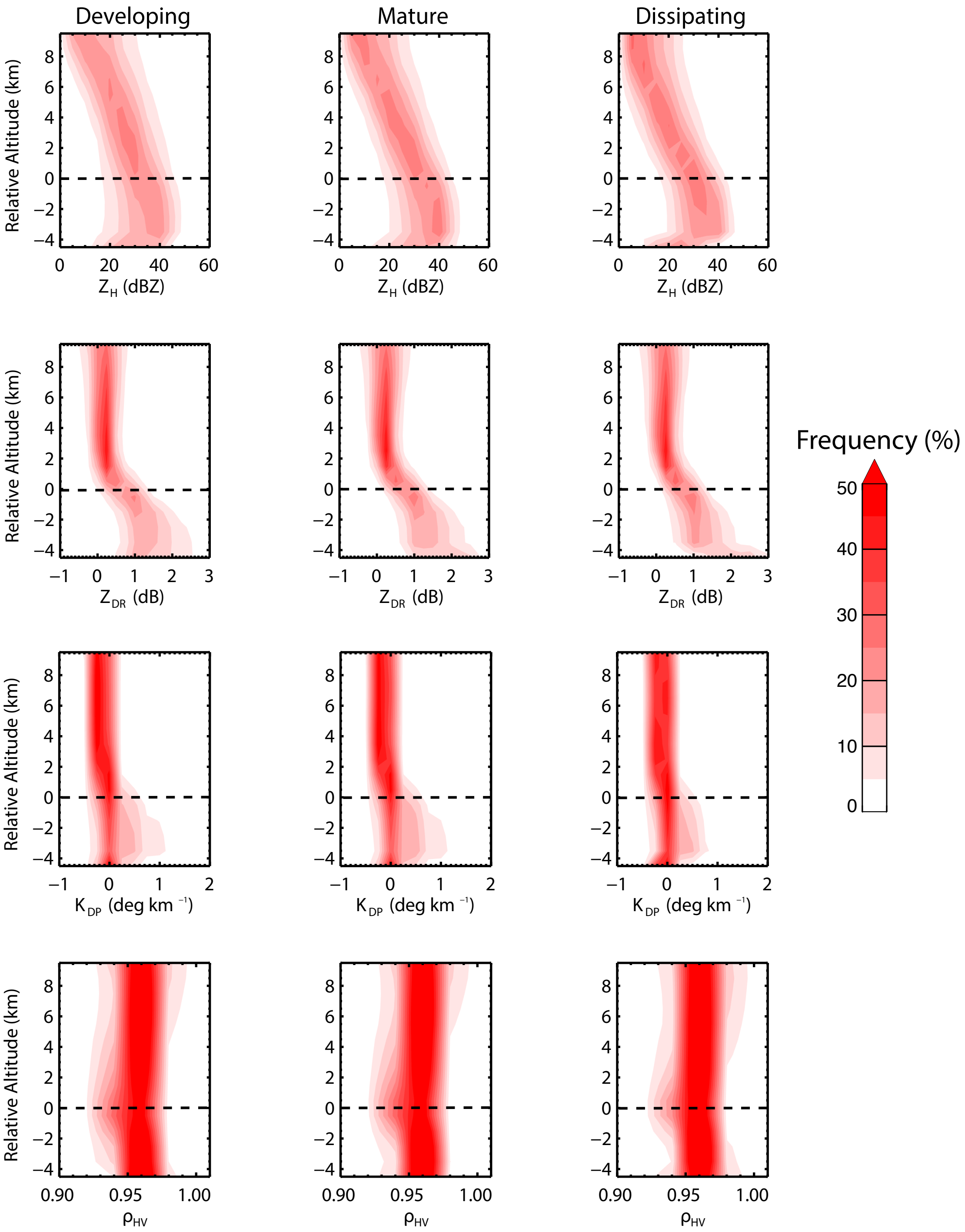

Figure 20: Composite Z_H (top) and Z_{DR} (bottom) convective source region CFADs from all 34 MCS events combined via weighted averaging. Colored contours represent the frequency (%). Dashed black line represents the 0 km relative altitude bin. Each panel represents one of the three evolutionary stages as labeled above each figure. All observations are binned relative to the environmental freezing level altitude.

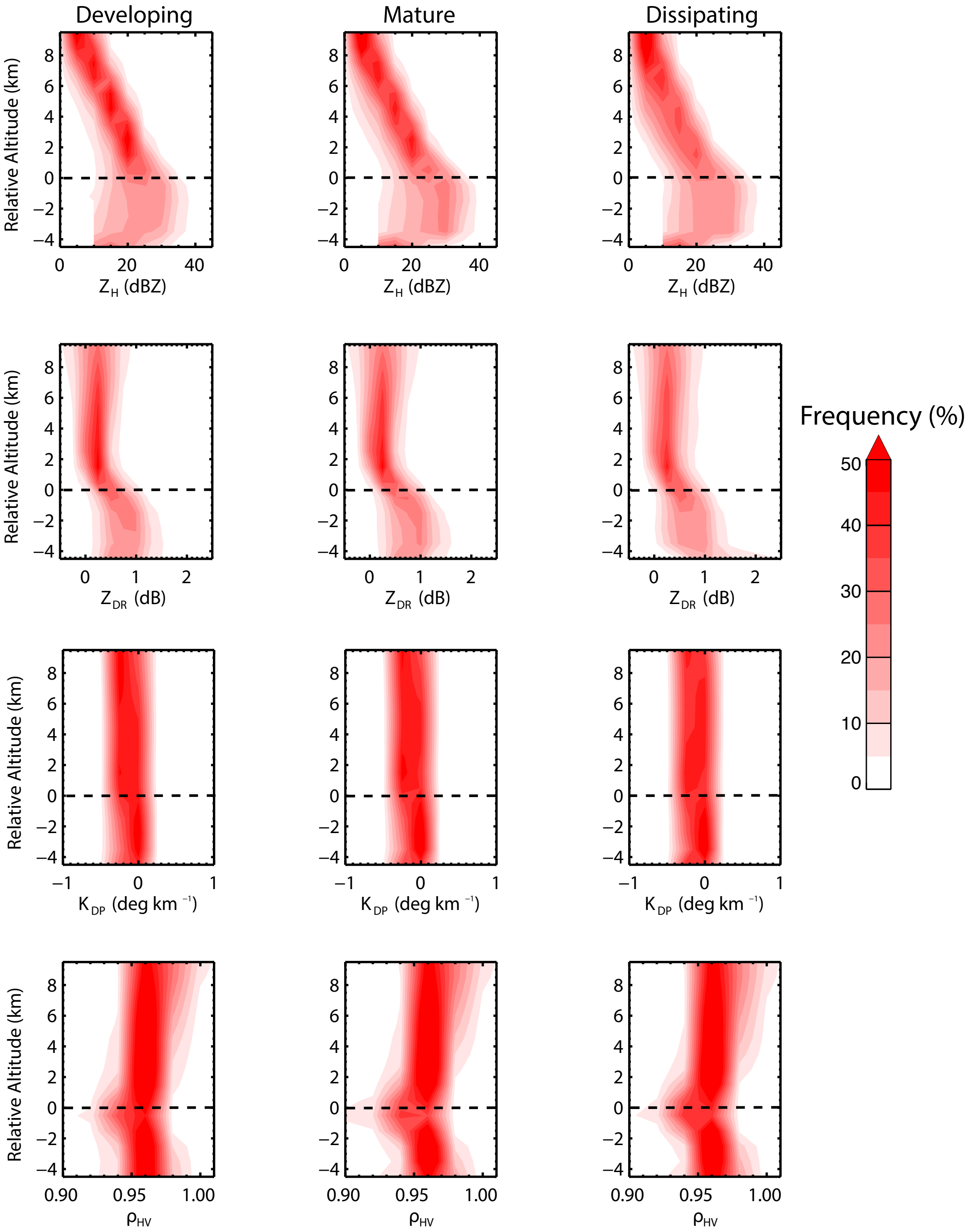

Figure 21: Similar to figure 20 except the stratiform source region is analyzed.

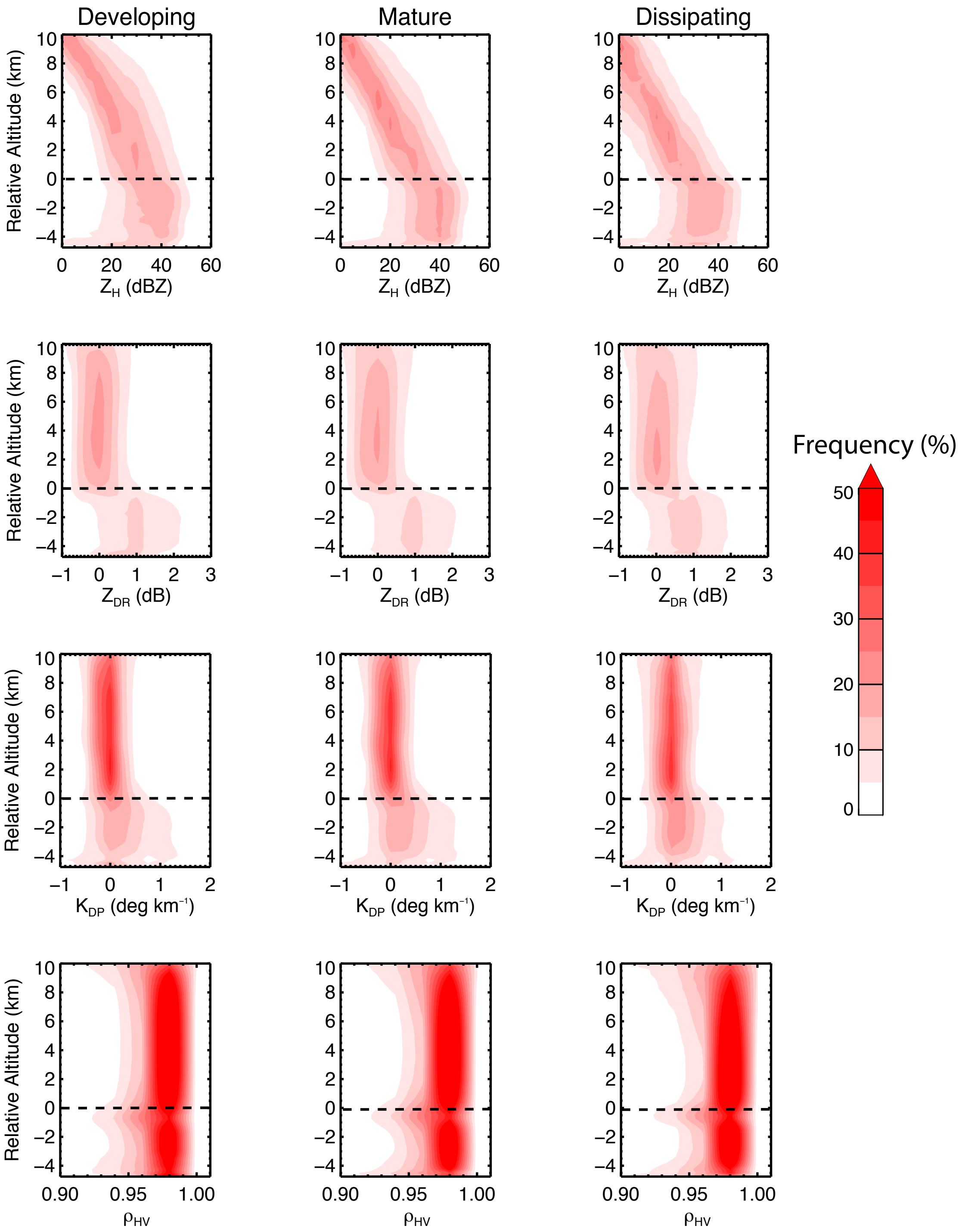

Figure 22: Single radar perspective CFAD similar to figure 21 except for the convective source region and only observations within 60 km from range of the radar were used.

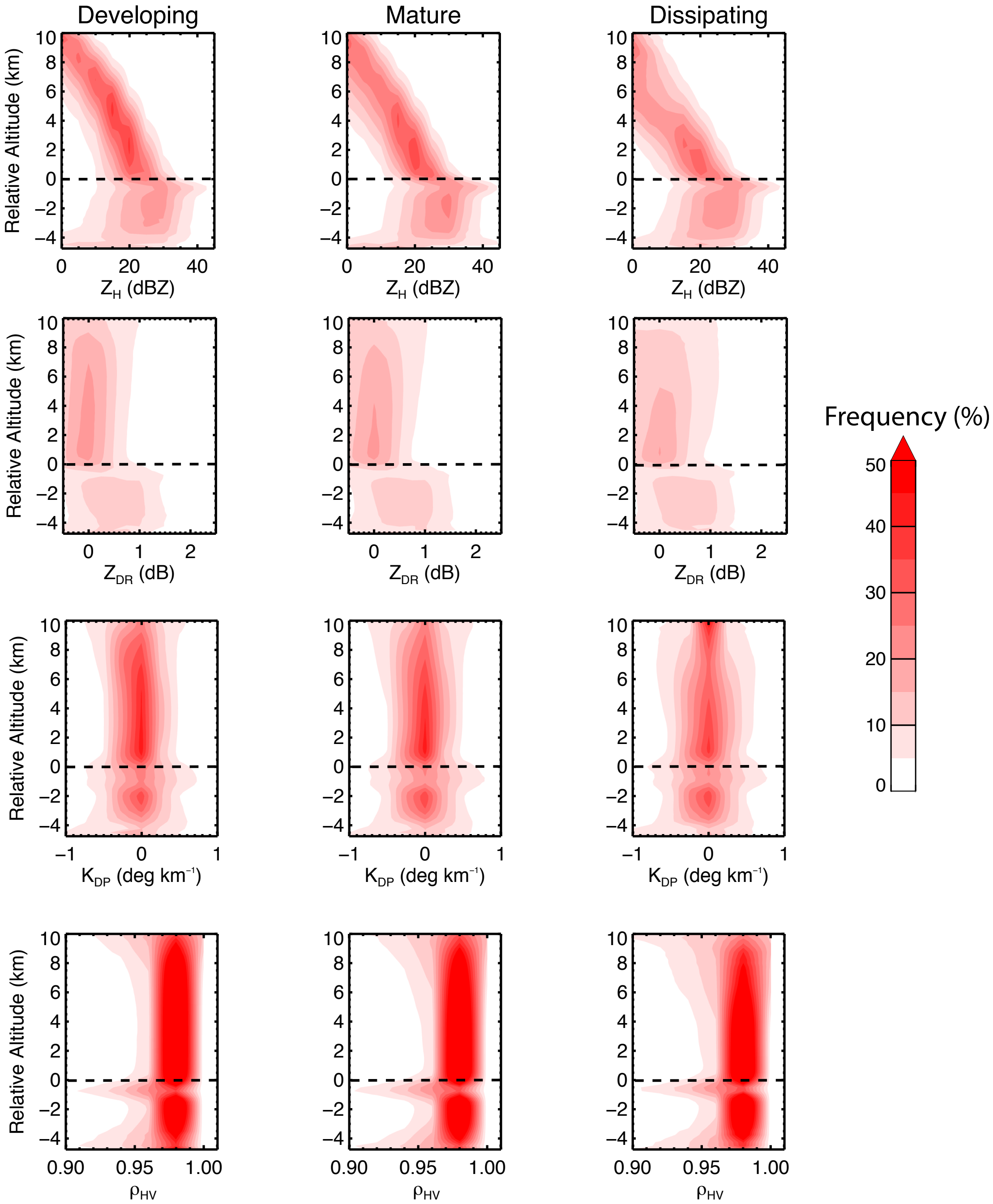

Figure 23: Single radar perspective CFAD similar to figure 21 except only observations within 60 km from range of the radar were used.

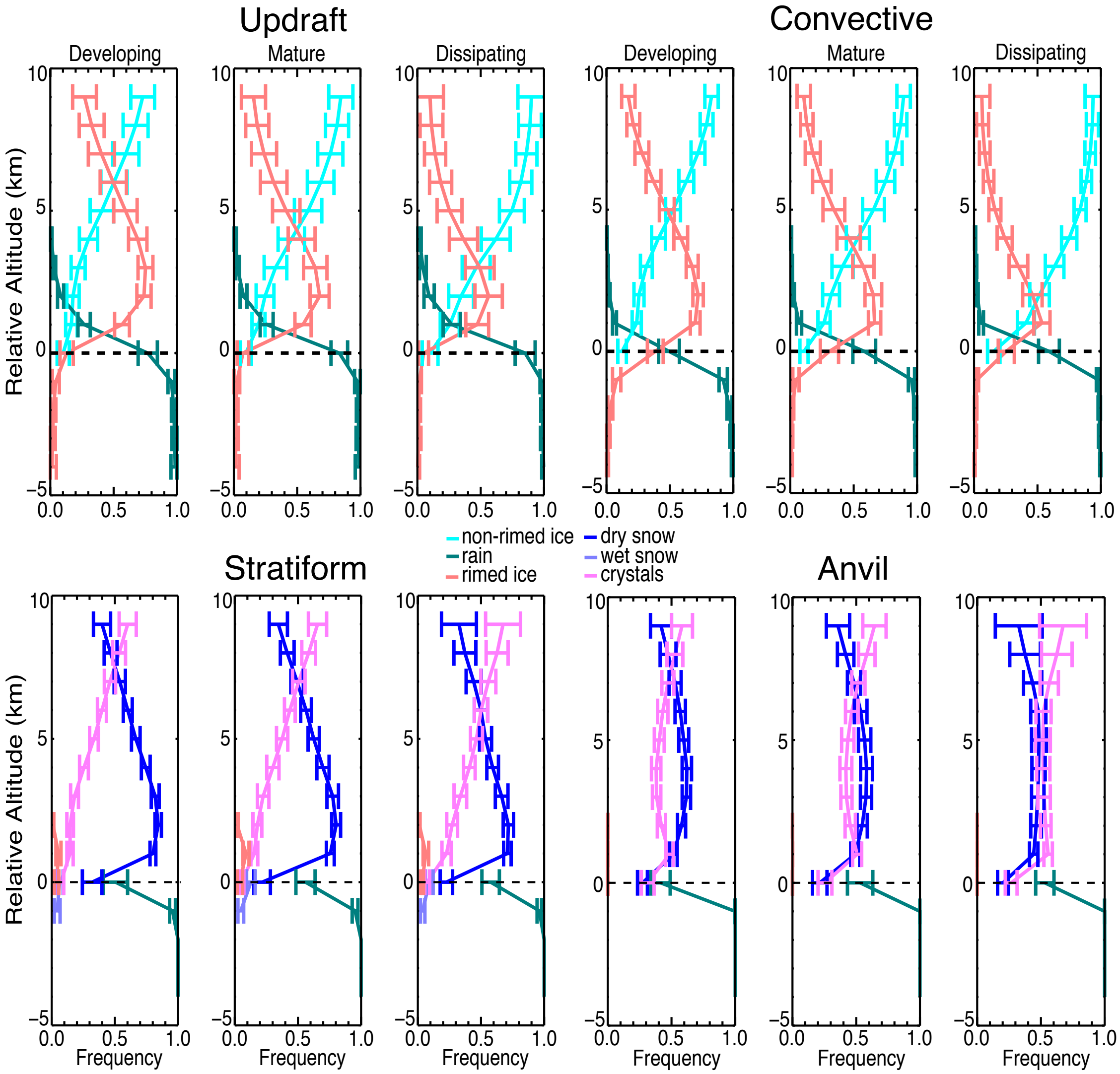

Figure 24: Composite mean vertical hydrometeor frequency profiles for all MCS events merged together via weighted averaging as function of evolutionary stage. Each source of precipitation is shown. All observations are binned relative to the environmental freezing level altitude. Dashed line represents the 0 km relative altitude bin. Hydrometeor classes are indicated by the center legend. Frequencies can be converted to % by multiplying any value by 100%.

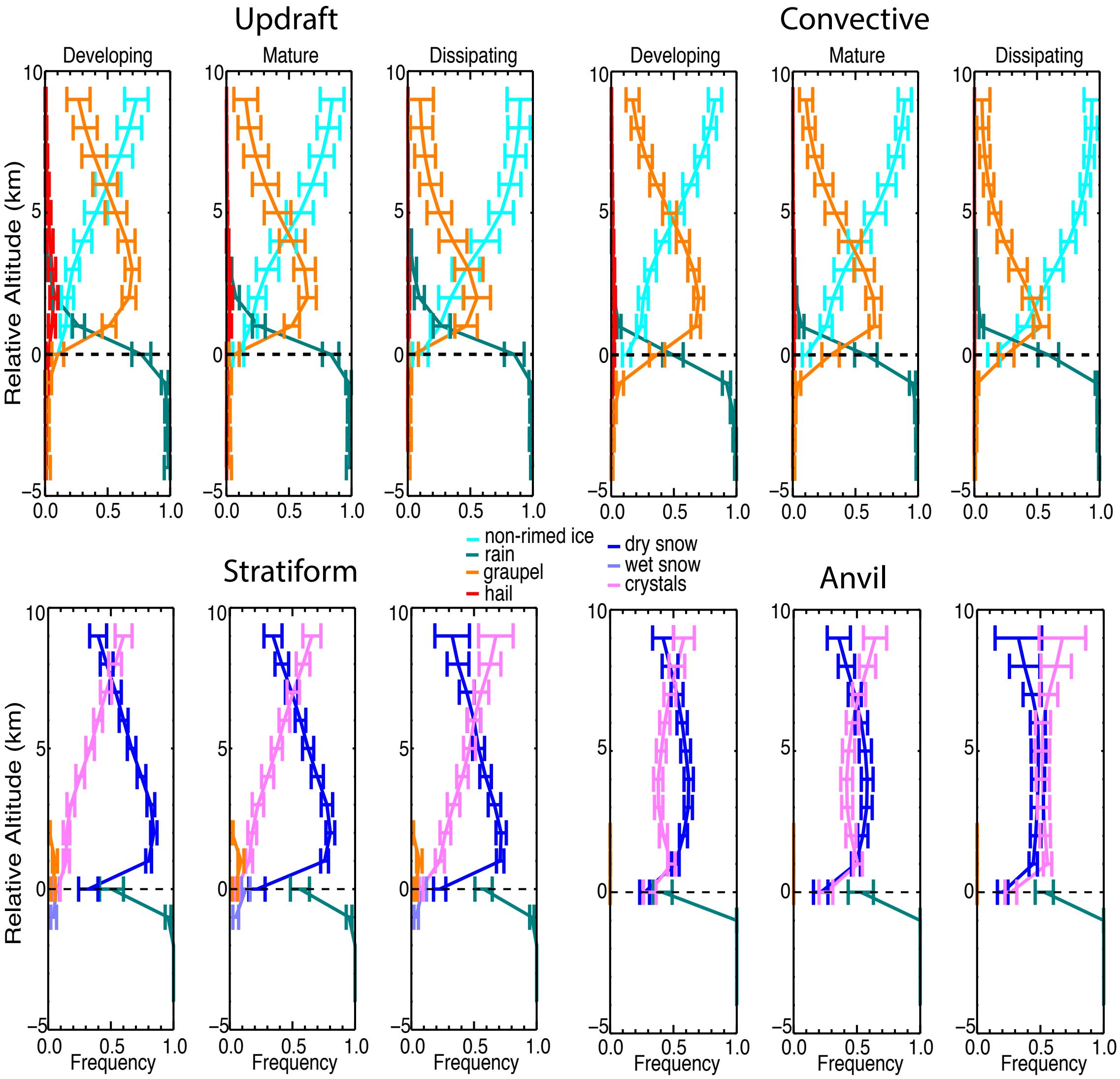

Figure 25: Similar to figure 24 except the rimed ice category is separated into graupel and hail components.

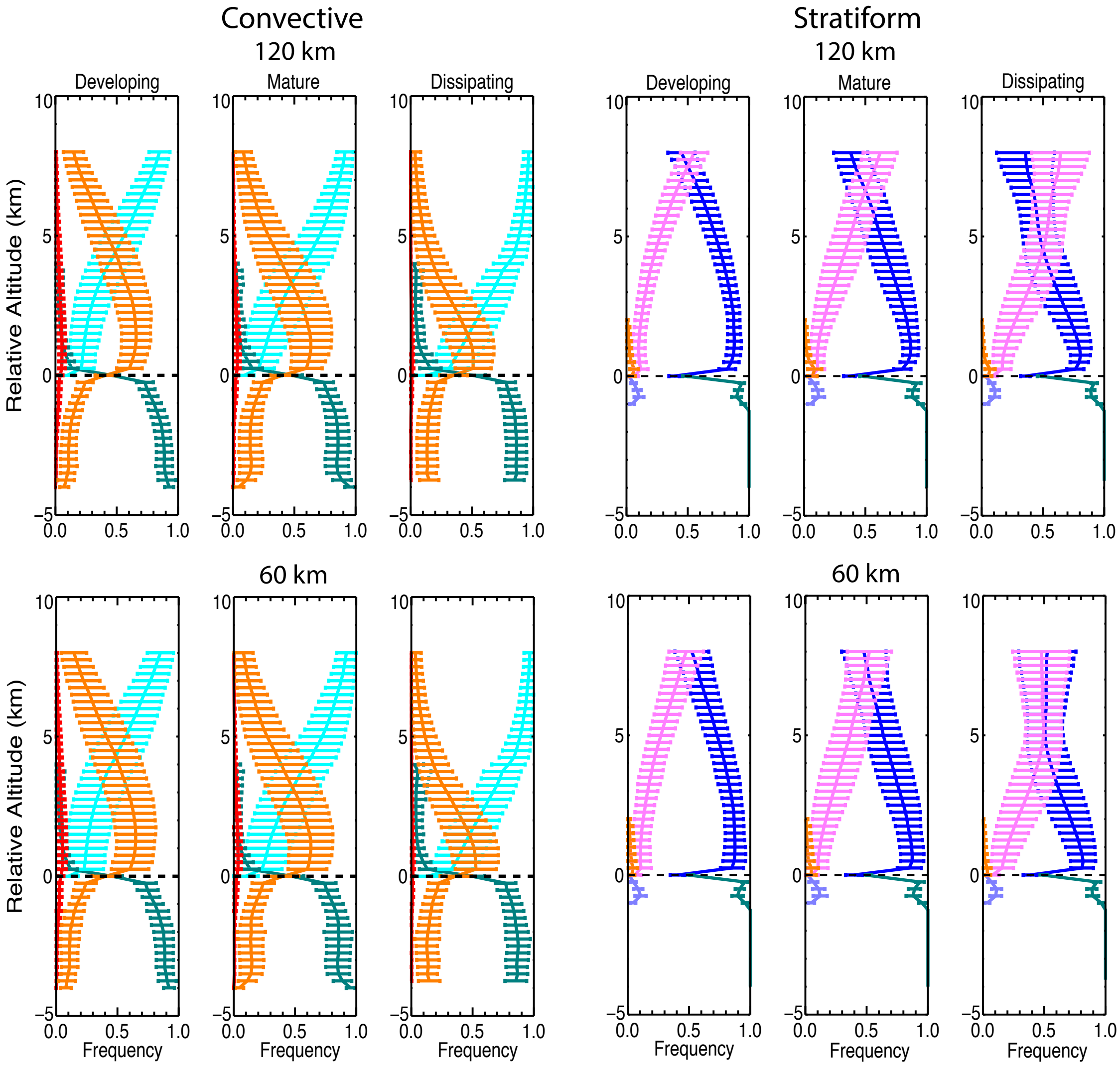

Figure 26: Composite mean vertical hydrometeor frequency profiles from the single radar perspective as a function of evolutionary stage and distance from radar. Note the enhanced vertical resolution and increased variability. Left 2 panels indicate convective source region, right w panels indicate the stratiform source region.

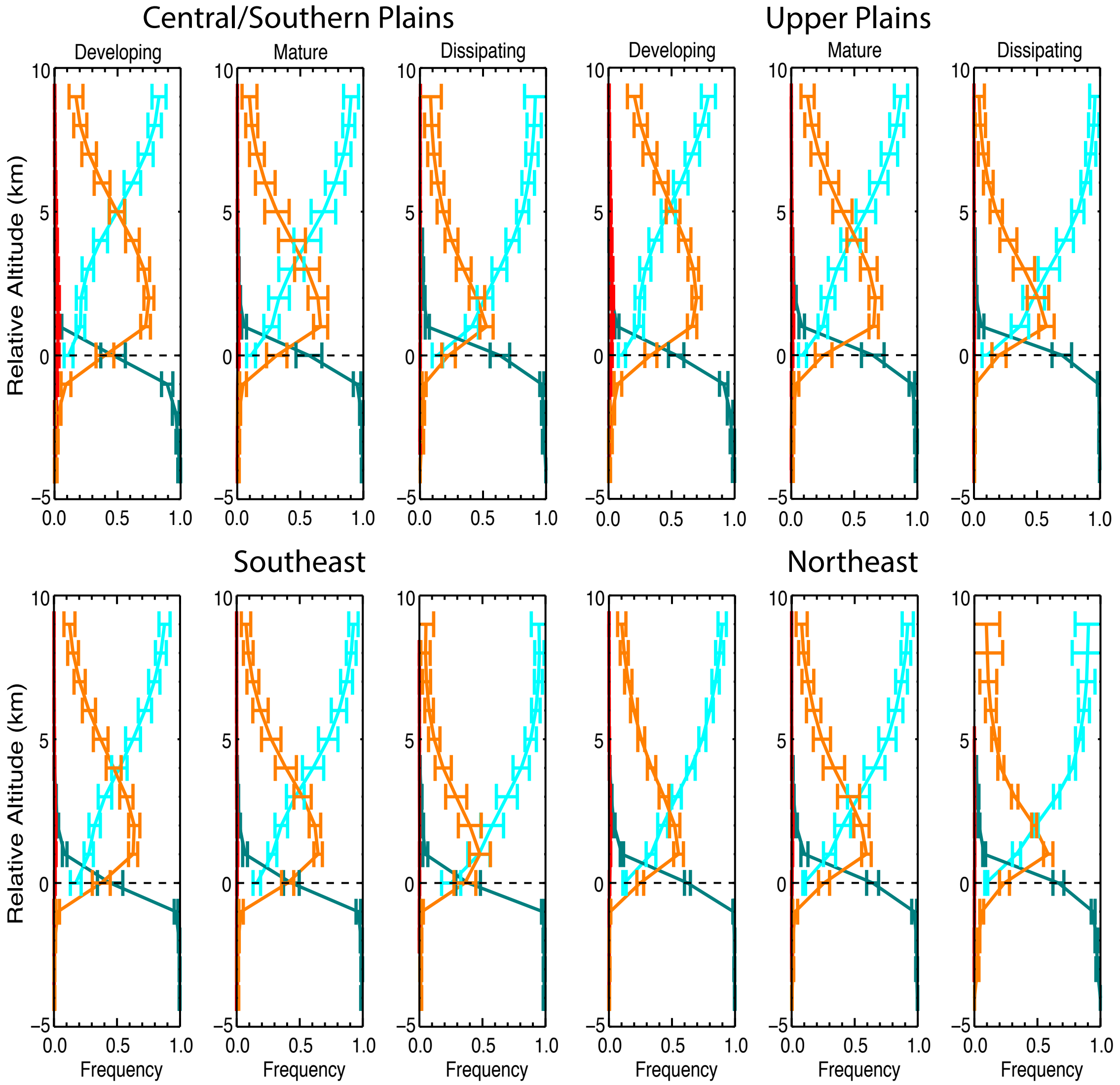

Figure 27: Similar to figure 25 except profiles represent composited hydrometeor frequency distributions of MCSs in different geographic zones for only the convective source region.

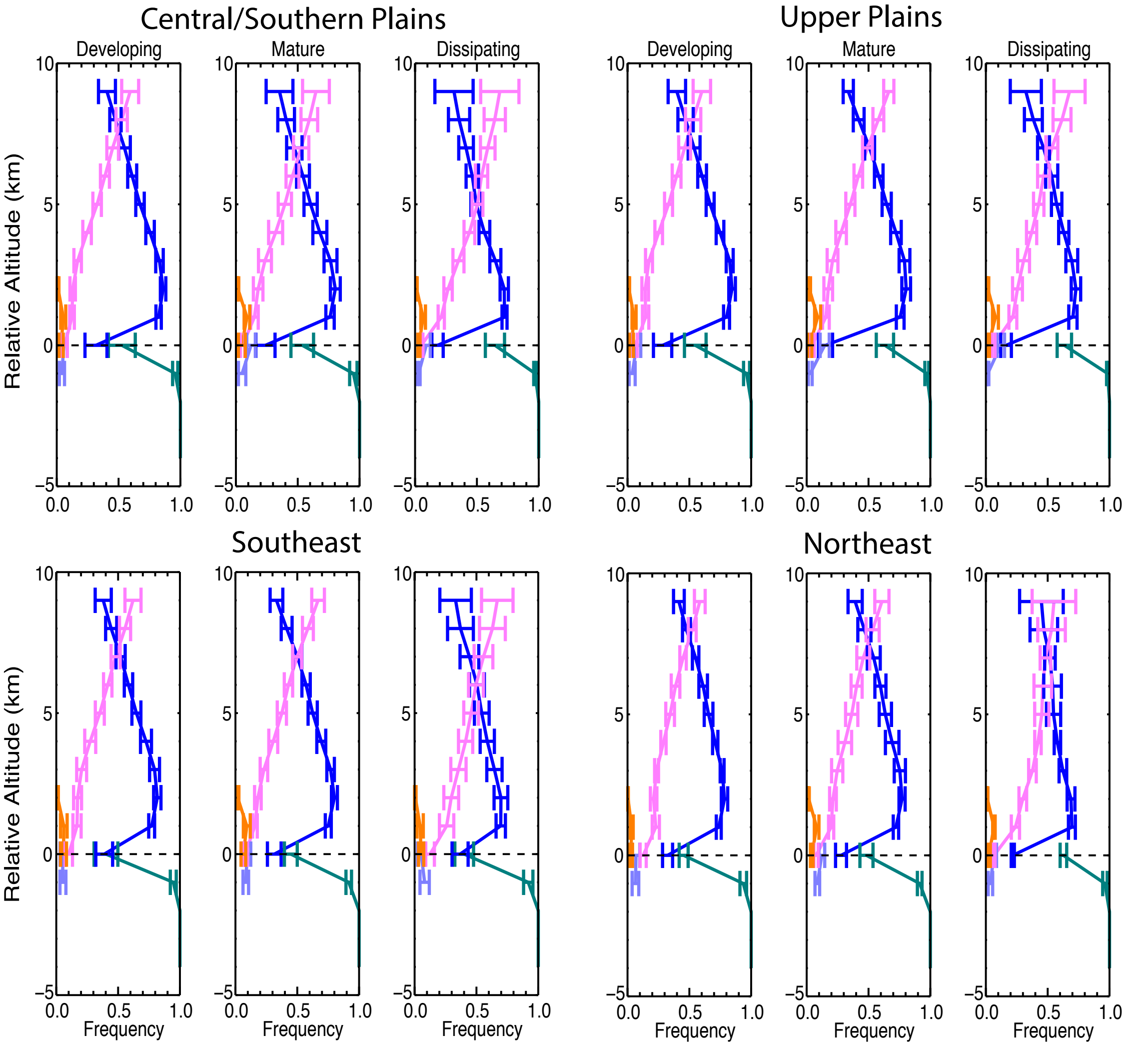

Figure 28: Similar to figure 27 except the stratiform source region is analyzed.

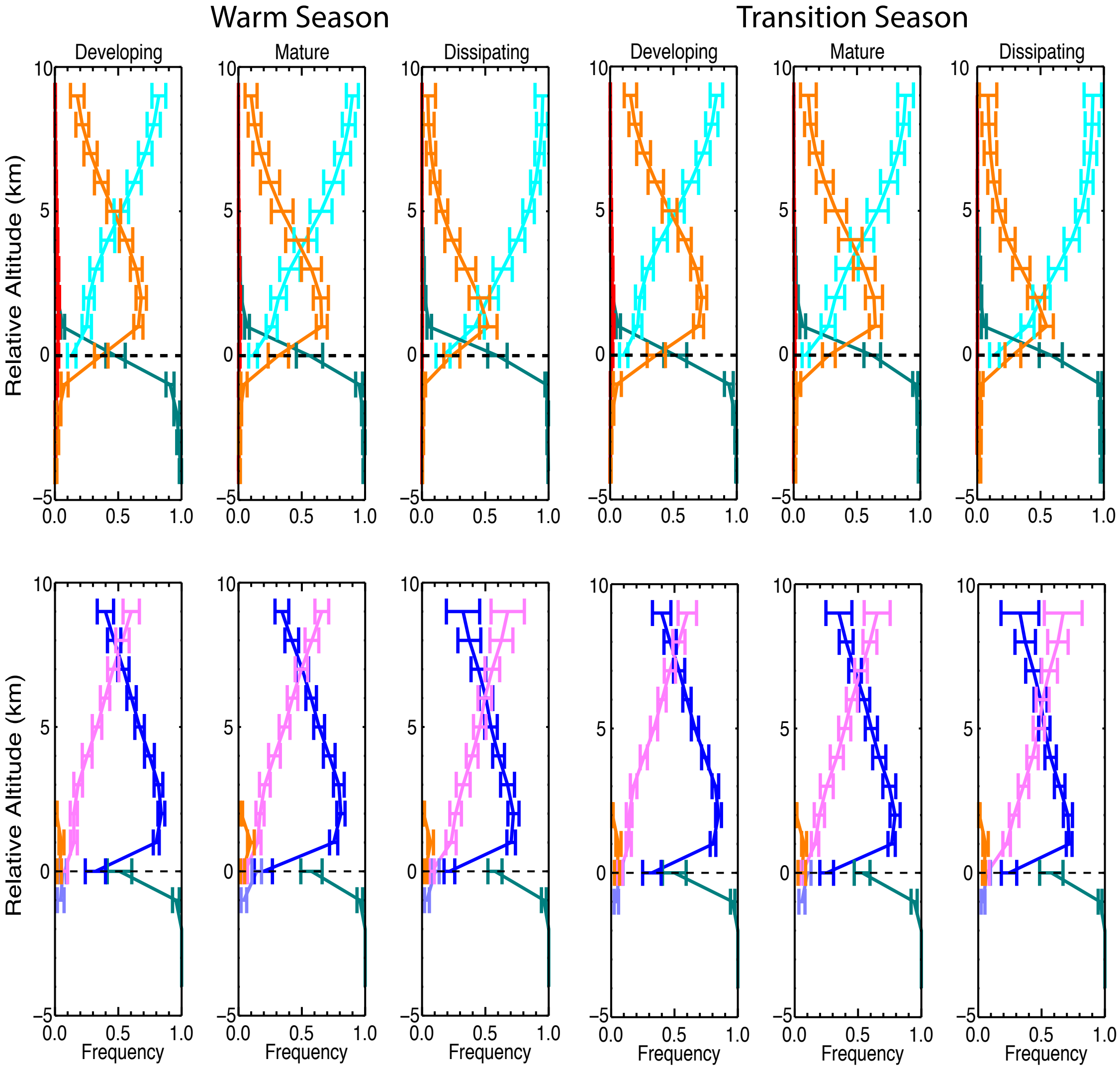

Figure 29: Simialr to figure 27 and figure 28 except frequency distributions represent warm season (JJA) and transition seasons (MAM; SON) events. Convective source region profiles are shown on the top panels, whereas stratiform profiles are shown on the bottom two profiles.

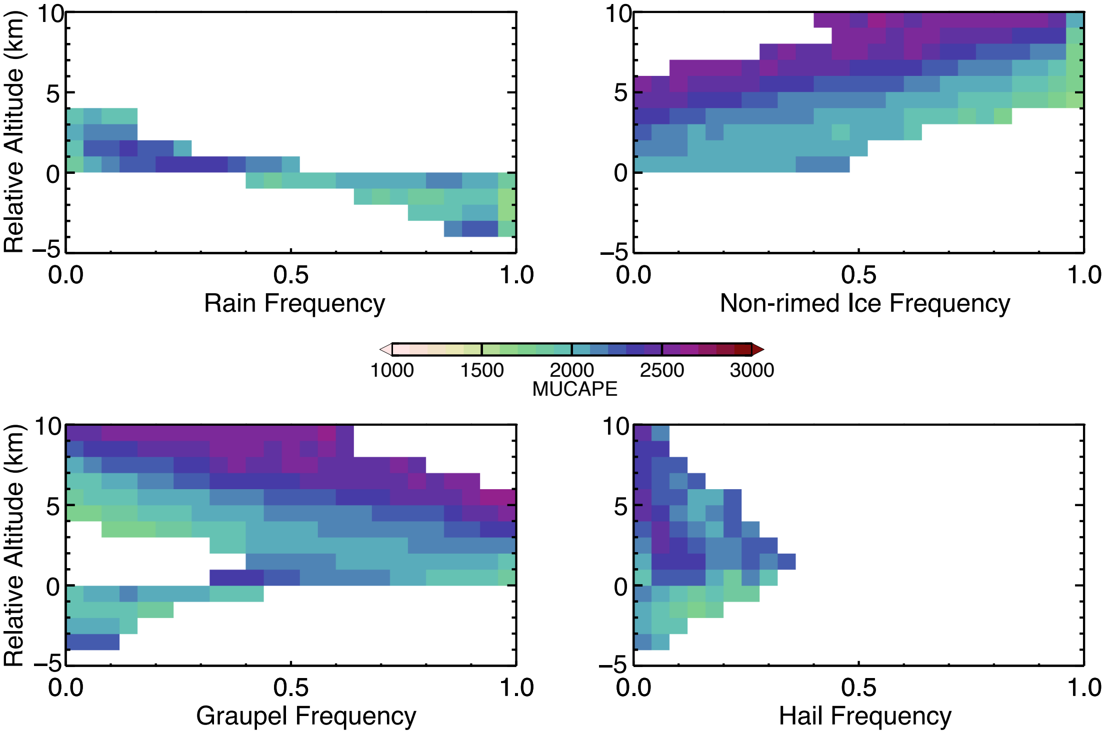

Figure 30: Environmental MUCAPE fill plots for individual storms within the convective region of mature MCSs. Each of the four boxes represents a hydrometeor class denoted along the x-axis. MUCAPE is filled with the colorbar indicating the range of MUCAPE values seen in the center of the plot. Frequencies can be computed as (%) by multiplying by 100%.

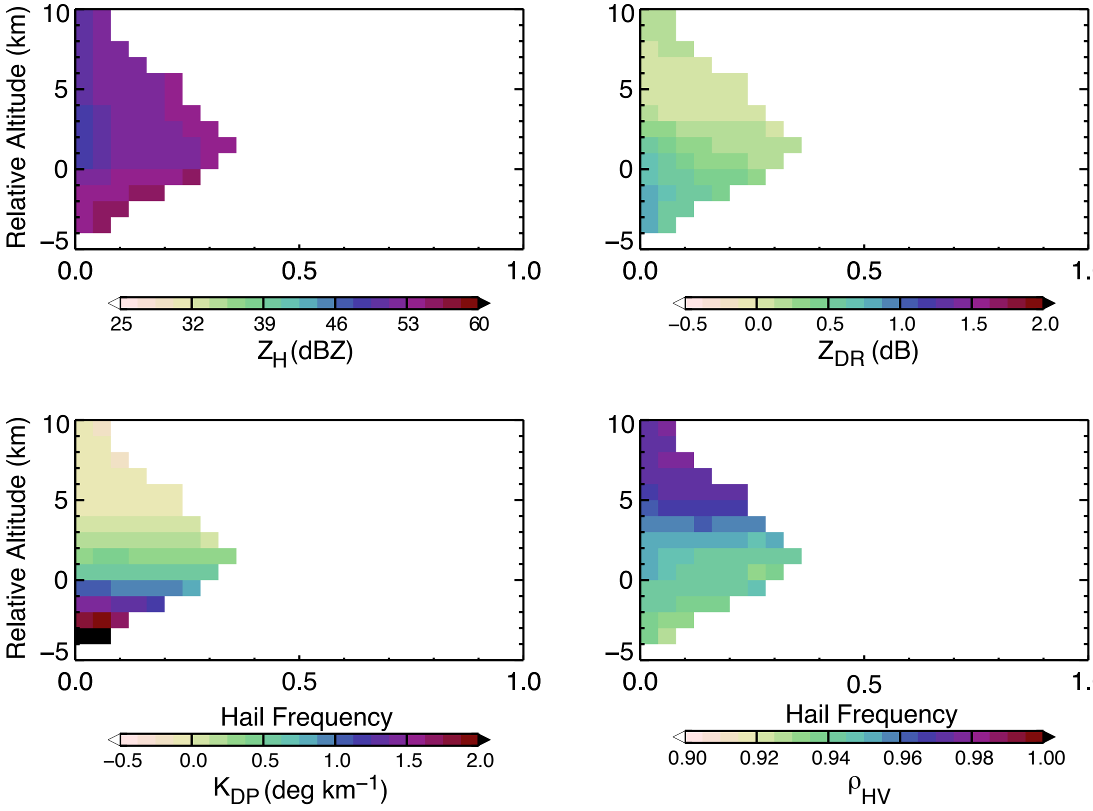

Figure 31: Simialr to figure 30 except polarimetric radar variables are color filled for only the hail hydrometeor class.

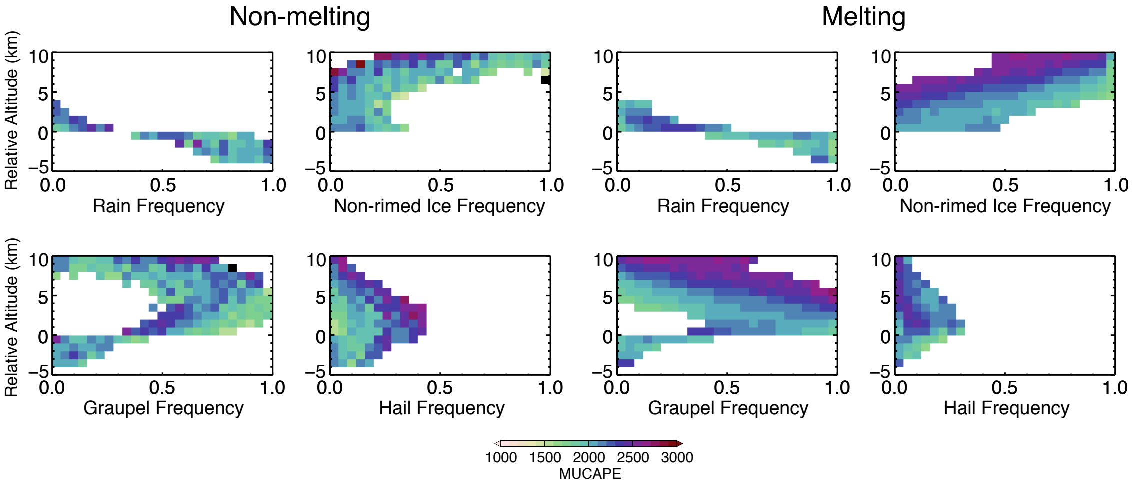

Figure 32: Same as figure 30 except individual storms labeled "non-melting storms" (left) and "melting storms" (right) are analyzed.

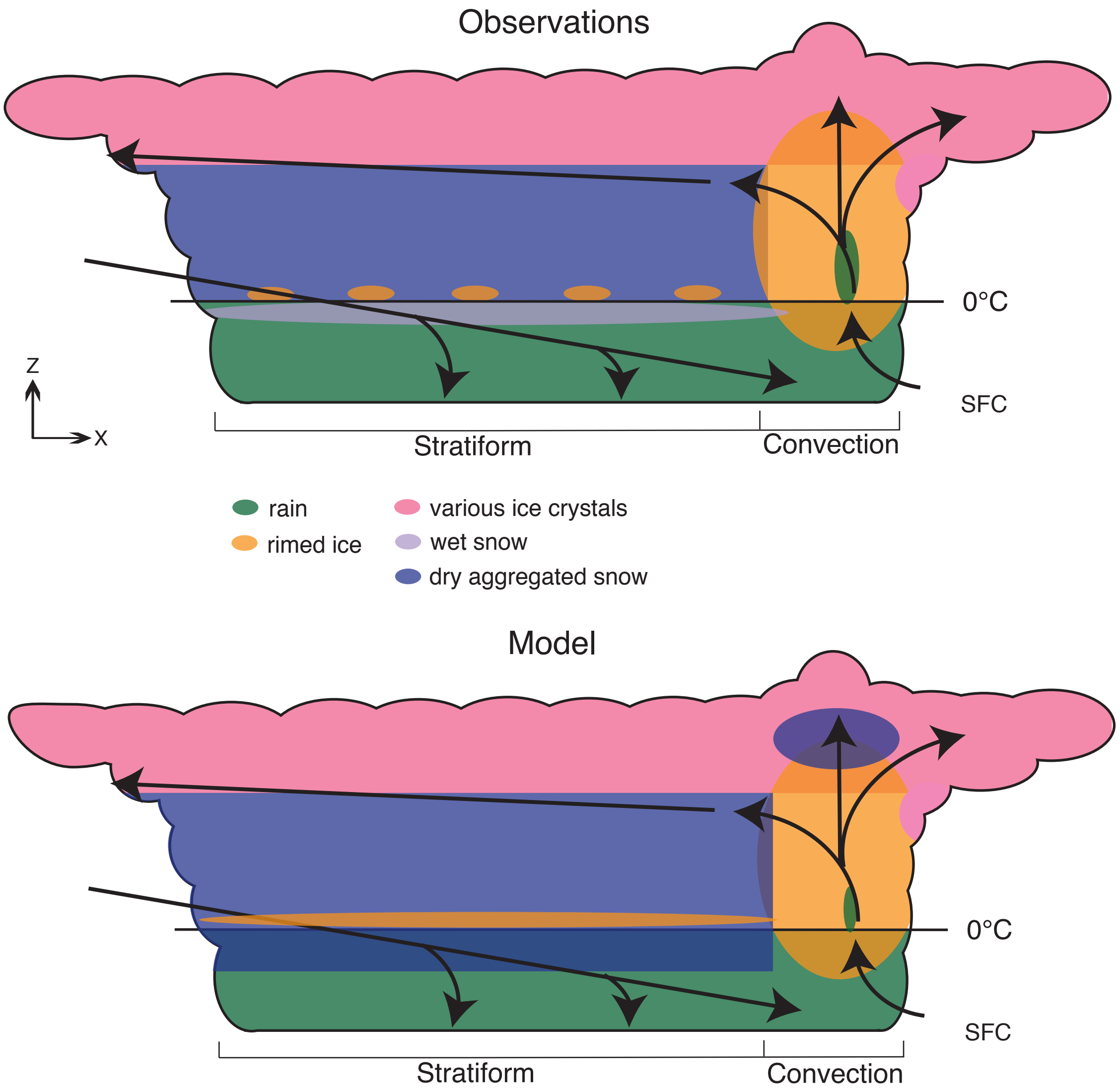

Figure 33: Conceptual schematic from both the observational analysis (top) and model analysis (bottom). Each color is represented by the legend in the middle of the figure. Black arrows denote characteristics airflow patterns. The 0°C altitude is shown.